



Terms and Conditions of Use of Digitised Theses from Trinity College Library Dublin

Copyright statement

All material supplied by Trinity College Library is protected by copyright (under the Copyright and Related Rights Act, 2000 as amended) and other relevant Intellectual Property Rights. By accessing and using a Digitised Thesis from Trinity College Library you acknowledge that all Intellectual Property Rights in any Works supplied are the sole and exclusive property of the copyright and/or other IPR holder. Specific copyright holders may not be explicitly identified. Use of materials from other sources within a thesis should not be construed as a claim over them.

A non-exclusive, non-transferable licence is hereby granted to those using or reproducing, in whole or in part, the material for valid purposes, providing the copyright owners are acknowledged using the normal conventions. Where specific permission to use material is required, this is identified and such permission must be sought from the copyright holder or agency cited.

Liability statement

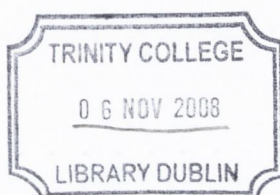
By using a Digitised Thesis, I accept that Trinity College Dublin bears no legal responsibility for the accuracy, legality or comprehensiveness of materials contained within the thesis, and that Trinity College Dublin accepts no liability for indirect, consequential, or incidental, damages or losses arising from use of the thesis for whatever reason. Information located in a thesis may be subject to specific use constraints, details of which may not be explicitly described. It is the responsibility of potential and actual users to be aware of such constraints and to abide by them. By making use of material from a digitised thesis, you accept these copyright and disclaimer provisions. Where it is brought to the attention of Trinity College Library that there may be a breach of copyright or other restraint, it is the policy to withdraw or take down access to a thesis while the issue is being resolved.

Access Agreement

By using a Digitised Thesis from Trinity College Library you are bound by the following Terms & Conditions. Please read them carefully.

I have read and I understand the following statement: All material supplied via a Digitised Thesis from Trinity College Library is protected by copyright and other intellectual property rights, and duplication or sale of all or part of any of a thesis is not permitted, except that material may be duplicated by you for your research use or for educational purposes in electronic or print form providing the copyright owners are acknowledged using the normal conventions. You must obtain permission for any other use. Electronic or print copies may not be offered, whether for sale or otherwise to anyone. This copy has been supplied on the understanding that it is copyright material and that no quotation from the thesis may be published without proper acknowledgement.

Near-infrared Luminescent Polymer Amplifiers and Microlasers



By

Martin Nkrumah Djiango

A thesis submitted for the degree of

Doctor of Philosophy

in the

University of Dublin



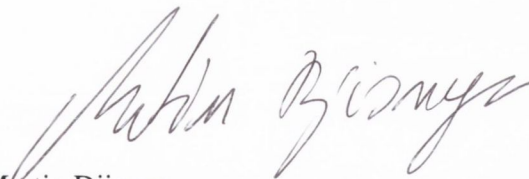
School of Physics
Trinity College Dublin

May 2008

THOSIS
8607

Declaration

I declare that the work in this thesis has not been previously submitted as an exercise for a degree to this or any other university. The work described herein is entirely my own, except for the assistance mentioned in the acknowledgements and the collaborative work mentioned in the list of publications. I agree that Trinity College Library may lend or copy this thesis on request.



Martin Djiango

May 2008

To my parents Michel and Margit Djiango,
and my sisters Mamkoué, Amina, and Mélanie.

“Beard and hair, everywhere”

Acknowledgements

First of all, I would like to thank my supervisor Professor Werner Blau. Thank you not only for giving me the opportunity to do this PhD but also to become a full-time TCD student after my Socrates' year and arranging my fourth year project to be done at the ENS Cachan in France.

I would like to thank my co-supervisor Dr. Kobayashi for working closely with me on the different projects and being available on a daily basis. Thank you for the help, support, and guidance over the years. You always saw light where I could only see darkness.

The year is 2008 A. D. The scientific world is entirely occupied by the nanoscientists. Well, not entirely... One small group of indomitable optical scientists still holds out against the invaders. Over the years the "Gauls" have been: Paula, Grace, Michael, Nino, and Estelle. The Romans, a full legion of them, are: Marguerite, Evelyn, Phil, Mustafa, Darren, Denise, Karen, David, Umar, Yenny, Niall, Chris, Anna, Trevor, Eddie, Shane, Fiona, Helen, Zhenyu, Sukanta, Javier, Ronan, and Jun. I am grateful for all your help.

I would like to thank Mrs. Cummins for all her help in dealing with the administrative matter. I would like to thank Mr. Concannon for all his help in dealing with computer and software related issues.

Thanks, Dr. Blond for all the "petits et grands dates". Ah ça!!! Thanks Dr. D'Arcy for letting me occupy your office for so long. If it all goes well, I will no longer need to show you respect.

I am very grateful to our collaborators at the institute of multidisciplinary research for advanced materials in Sendai (Japan). Thank you Professor Kaino, Dr. Komatsu, Dr. Suzuki, and Mr. Cai for the all the good advice.

I would like to thank Francis Hendron from the Geology department, and Dr. Tania Perova and Dr. Melnikov from the engineering department for the excellent technical assistance in the etching of the optical fibres (are you sure HF is that nasty?). I am grateful to Yuri Rakovich for the excellent technical assistance in the lifetime measurements. I would like to thank Neal Leddy from the centre for microscopical analysis for all the help with the SEM and the white light interferometer (What is life like with short hair?). I am grateful to Dr. Pons for the computation of the molecule's orbitals with use of the Trinity Centre for High Performance Computing (TCHPC) capacities. I would like to thank Christopher Smith for measuring the refractive index by use of variable angle ellipsometry.

Finally, I would like to thank my housemates for their patience and tolerance of my hair and beard as they found it scattered around the house. Thanks Dave for all the food. I know I am your second stomach. Thanks Siobhán for giving me my fair share of great chats. Thanks Magda for our sister-brother, girlfriend-boyfriend, tenant-landlord, Oprah-Dr. Phil...(the list is quite long) type relationship.

Abstract

Near-infrared optical gain in luminescent polymeric slab asymmetric waveguides has been investigated by use of amplified spontaneous emission. Upon nanosecond photopumping, the waveguides have shown a small-signal gain coefficient of $37.2 \pm 2.1 \text{ cm}^{-1}$ at 820 nm for a pump fluence of 1.57 mJ/cm^2 (314 kW/cm^2). It is shown that a small-signal gain of $19.7 \pm 2.3 \text{ dB}$ is achievable in a 1.2-mm-long waveguide. This is the largest gain reported to date for organic gain media operating in the near-infrared region of the spectrum.

Near-infrared laser emission from self-assembled luminescent polymer microcavities is reported. These microrings are formed around silica optical fibers of varying diameters (80, 125, and 200 μm) and are shown to exhibit photopumped lasing at $\sim 820 \text{ nm}$. The microrings with a 200- μm diameter have an overall quality factor of $\sim 2 \times 10^3$, which is limited by surface roughness and inhomogeneities. It is shown how the laser threshold varies inversely with both the quality factor and the diameter of the microrings. The free spectral range and the spatial coherence length of the laser output are also presented.

A cavity quantum electrodynamic enhancement of stimulated emission in polymer microcavities is reported for the first time. The enhancement of the stimulated emission cross-section is revealed through the demonstration of laser action in the microrings whose total active element population density is below that theoretically required for the onset of lasing. The lower bound of the enhancement factor is estimated to be 3.9 based on the bulk or non-cavity value of the stimulated emission cross-section and the measured cavity quality factor.

Table of Contents

Acknowledgements	I
Abstract	III
Table of Contents	IV
Chapter 1: Introduction	1
1.1 - Motivation.....	1
1.2 - Outline	3
1.3 - References.....	5
Chapter 2: Theory	6
2.1 - Basic Properties of Organic Compounds.....	6
2.1.1 - The Conjugated System	6
2.1.2 - Light-matter Interaction in Laser Dyes.....	9
2.2 - Atom-field Interactions.....	11
2.2.1 - The time-dependent Schrödinger Equation	11
2.2.2 - Einstein's Coefficients.....	14
2.3 - Organic dye: a Four-level Laser System	16
2.4 - Summary.....	18
2.5 - References.....	19
Chapter 3: Materials and Basic Spectroscopy.....	20
3.1 - Introduction.....	20
3.2 - Materials	20
3.2.1 - Laser Dyes	20
3.2.2 - Organic Matrices	22
3.2.3 - Solvents.....	24
3.3 - Density Functional Theory	25
3.4- Liquid Phase	28
3.4.1- Solvent Effect	28
3.4.2 - Lippert Equation ¹	30
3.5 - Solid Phase.....	33
3.5.1 - LDS821 Samples	33
3.5.2 - LD800 and LDS798 Samples	36
3.6 - Fluorescence Lifetime Measurements	37
3.7 - Summary.....	38
3.8 - References.....	39
Chapter 4: Optical Gain Spectroscopy.....	40
4.1 - Introduction.....	40
4.2 - A Bit of History	40

4.3 - Theory.....	41
4.3.1 - Slab Asymmetric Waveguide Theory.....	41
4.3.2 - One-dimensional Amplifier Theory.....	47
4.4 - Methodology.....	48
4.4.1 - Sample Preparation (see Appendix A).....	48
4.4.2 - Experimental Procedure.....	49
4.5 - A Near-infrared Plastic Amplifier.....	52
4.5.1 - Initial Tests.....	52
4.5.2 - Amplifier Regimes.....	53
4.5.3 - Modal gain.....	57
4.5.4 - Loss Measurements.....	58
4.5.5 - Pump Saturation.....	59
4.5.6 - Small-signal Gain.....	60
4.5.7 - LD800 and LDS798 Samples.....	61
4.6 - Fabry-Pérot Cavity Laser.....	62
4.7 - Review of Gain Media in the Near-infrared Region.....	65
4.8 - Light-emitting Devices.....	66
4.9 - Summary.....	70
4.10 - References.....	71
Chapter 5: Microring Laser Cavities.....	73
5.1 - Introduction.....	73
5.2 - Whispering Gallery Modes.....	73
5.2.1 - A Bit of History.....	74
5.2.2 - Theory.....	75
5.3 - Methodology.....	79
5.3.1 - Device Fabrication (see Appendix A).....	79
5.3.2 - Experimental Set-up.....	81
5.4 - The Microring Resonator.....	82
5.4.1 - Free Spectral Range.....	82
5.4.2 - Quality Factor.....	84
5.4.3 - Spectral Analysis: Mode Assignment.....	86
5.5 - The Microring Laser.....	88
5.5.1 - Laser Emission.....	88
5.5.2 - Laser Threshold.....	89
5.5.3 - Transverse Coherence Length.....	91
5.5.4 - Longitudinal Pumping.....	92
5.6 - Microrings in the Continuous Wave Regime.....	93
5.7 - Summary.....	95
5.8 - References.....	96
Chapter 6: Stimulated Emission Enhancement in a Microring Laser.....	98
6.1 - Introduction.....	98
6.2 - Theory.....	99
6.3 - Stimulated Emission Enhancement Factor Extraction Method.....	101
6.4 - Bulk Stimulated Emission Cross-section.....	102
6.4.1 - Quantum Yield Determination.....	102
6.4.2 - Stimulated Emission Cross-section Determination.....	104
6.5 - Device Fabrication (see appendix A).....	105
6.6 - Experimental Results.....	107

6.7 - Discussion.....	110
6.8 - Summary.....	111
6.8 - References.....	112
Chapter 7: Summary and Future Work.....	113
7.1 - References.....	116
Appendix A: Detailed Device Fabrication.....	117
Appendix B: Publications	121
Appendix C: Photograph of a Physicist	122

Chapter 1: Introduction

1.1 - Motivation

The past decade has seen intense research efforts for the development of solid-state organic gain media. Since the observation of stimulated emission from organic dyes in 1966, new classes of organic chromophores have been discovered: conjugated polymers¹ and dendrimers². These compounds all possess conjugated bonds, a chain of alternating single and double bonds. They have π electrons that are delocalised over the conjugation length and it takes wavelengths in the near-ultraviolet to the near-infrared regions to excite such molecules. These transitions are usually $\pi - \pi^*$ transitions and have large associated optical gain. One of the attractive features of organic compounds is the ability to modify the chemical structure in ways that can directly impact the properties of the materials such as absorption and emission spectra, solubility to name but a few. Also, their large emission spectrum means that dye lasers are easily tunable over a long range of wavelengths. Organic materials have other advantages over their inorganic counterparts: ease in processing and device fabrication, cost effectiveness, and high volume production. There are a number of techniques available for device fabrication in organic photonics: spin coating, photolithography, ink-jet printing, screen printing, and micromolding. These properties appear attractive for low-cost telecommunication networks.

In long-haul communication, optical fibres made from the inorganic material silica are well established because of the material's high bandwidth and transparency but have a typical core diameter in the range 5-10 μm . This small size is associated with their low flexibility and makes it difficult to fabricate, install and maintain the fibres if used in a local area network that needs a high number of connections. In recent years, plastic optical fibres (POFs) made of polymers instead of silica have started to replace coaxial cables and twisted pairs in such short-distance communication. POFs

have a low cost, are lightweight, flexible, and can be processed into large diameter fibres (~50-1000 μm) to ease connections. Furthermore, polymers no longer have the large attenuation associated with them. The dominant loss mechanism that was absorption by the overtones of bond stretching can now be overcome to a certain extent. In perfluorinated polymers for example, C-H bonds (where the fundamental vibrations fall in the 3300-3500 nm region) are replaced by C-F bonds (7600-10000 nm). Therefore, perfluorinated polymer based graded-index POF have a low-loss wavelength region from 500 to 1300 nm, with an attenuation loss of 40-60 dB/km at ~ 840 nm.³⁻⁶ The majority of work done on organic media to date has focused on light amplification in the visible region of the spectrum. Studies on near-infrared emitting organic gain media have been few and far between. It could be of great interest to develop an organic solid-state laser to replace the vertical gallium arsenide based cavity surface emitting lasers operating at 850 nm, the datacom wavelength. As there is a research push to develop organic filters, attenuators, switchers and with the already existing POFs, such a solid-state laser could be implemented in an all-plastic network. The first aim of this work is to find an organic dye that has high optical gain in the ~ 800 nm spectral region when embedded in a passive polymer.

The second aim of this work is to incorporate this organic compound into a laser of small dimensions for possible integration with passive components in optical integrated circuits and polymer waveguide-based short-distance communication networks. Among the variety of cavity structures investigated to date, self-assembled cylindrical microresonators present some advantages over other structures, namely high cavity quality factors, ease of coupling with optical waveguides^{7,8} as well as ease of fabrication. It would be of interest to investigate how the properties of these microrings acting as resonators and laser devices depend on the cavity size.

What makes such microcavities even more attractive are the beneficial cavity quantum electrodynamic (CQED) effects. Enhancement of stimulated emission⁹ and a large spontaneous emission coupling ratio¹⁰ should be possible for microrings with a volume approaching the cube of the transition wavelength. These factors could lead to a low-threshold operation, which is a prerequisite for the development of practical optically pumped amplification devices as well as for the future demonstration of an electrically pumped organic gain medium. Although CQED effects have been

predicted and also observed in cavities with a variety of shapes,⁹⁻¹⁵ they have yet to be exploited in microrings. The final aim of this project is to measure a possible enhancement of the stimulated emission cross-section in polymer microrings.

1.2- Outline

This thesis will be outlined as follows.

Chapter 2 will give a qualitative picture of light absorption and emission by and from an organic dye with special attention given to the conjugated chain in such a molecule. An organic dye is a four-level laser system and the rate for stimulated transition between two of its levels is found by solving a time-dependent Schrödinger equation.

Chapter 3 will introduce different candidates for high optical gain in the near-infrared region. The basic spectroscopic properties will be presented for these molecules when suspended in a solvent or in a polymer matrix. A numerical calculation using density functional theory will be used to find the change in dipole moment upon absorption of a photon by the molecule. The effect of solvent on the absorption and emission spectra will also be investigated.

Chapter 4 will report on the fabrication and gain spectroscopy studies of slab asymmetric waveguides with large gain in the near-infrared region. The different operation regimes below and above saturation of such an amplifier are presented. Laser operation at ~825 nm from such gain media was demonstrated by incorporating it into a low Q cavity: the Fabry-Pérot resonator. Amplified spontaneous emission in a film that has semiconducting properties is also shown.

Chapter 5 will cover the high Q laser cavity that is the dye-doped polymer microring. After outlining the fabrication technique, the properties of these microcavities will be investigated in their roles as resonators and laser devices. In particular, the effect of cavity dimensions on these properties will be studied. It will also be shown how

absorption and scattering losses affect the performance of these microrings.

Chapter 6 will verify if cavity quantum electrodynamic effects observed in certain microcavities also play a role in microrings. It will centre on the possibility of enhancing the stimulated emission cross-section.

Finally, conclusions will be drawn and future work suggested in Chapter 7.

1.3 - References

- ¹ D. D. Bradley, Proc. Int. Conf. Science and Technology of Synthetic Metals **84**, (1997).
- ² J. R. Lawrence, G. A. Turnbull, I. D. W. Samuel, G. J. Richards, and P. L. Burn, Opt. Lett. **29**, 869 (2004).
- ³ J. P. Harmon and G. K. Noren, *Optical polymers: fibers and waveguides* (American Chemical Society [distributed by Oxford University Press], Washington, D.C.[Oxford], 2001).
- ⁴ <http://www.chromisfiber.com/pdf/gigapof120sr.pdf>.
- ⁵ T. Kaino, K. Jinguji, and S. Nara, Appl. Phys. Lett. **42**, 567 (1983).
- ⁶ H. P. A. Van Den Boom, W. Li, P. K. Van Bennekom, I. T. A. Monroy, and A. Giok-Djan Khoe, IEEE J. Sel. Top. Quantum Electron. **7**, 461 (2001).
- ⁷ B. E. Little, S. T. Chu, H. A. Haus, J. A. Foresi, and J. P. A. Laine, J. Lightwave Technol. **15**, 998 (1997).
- ⁸ D. V. Tishinin, P. D. Dapkus, A. E. Bond, I. A. Kim, C. K. A. Lin, and J. A. O'brien, IEEE Photonics Tech. Lett. **11**, 1003 (1999).
- ⁹ F. Demartini, P. Mataloni, and L. Crescentini, Opt. Lett. **17**, 1370 (1992).
- ¹⁰ M. Osuge and K. Ujihara, J. Appl. Phys. **76**, 2588 (1994).
- ¹¹ A. M. Adawi, A. Cadby, L. G. Connolly, W. C. Hung, R. Dean, A. Tahraoui, A. M. Fox, A. G. Cullis, D. Sanvitto, M. S. Skolnick, and D. G. Lidzey, Adv. Mater. **18**, 742 (2006).
- ¹² A. J. Campillo, J. D. Eversole, and H. B. Lin, Phys. Rev. Lett. **67**, 437 (1991).
- ¹³ J. C. Knight, H.S.T. Driver, and G.N. Robertson, J. Opt. Soc. Am. B **11**, 2046 (1994).
- ¹⁴ M. A. Noginov, G. Zhu, M. Bahoura, C. E. Small, C. Davison, J. Adegoke, V. P. Drachev, P. Nyga, and V. M. Shalaev, Phys. Rev. B **74**, 184203 (2006).
- ¹⁵ P. Sandeep and P. B. Bisht, Chem. Phys. Lett. **371**, 327 (2003).

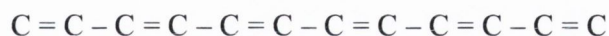
Chapter 2: Theory

In 1917, Einstein¹ predicted the possibility of stimulated emission, which finds its most notable application in the lasing process, and derived the corresponding probability coefficient. The first successful laser device was a flashlamp-pumped ruby laser operating at 694 nm reported by Maiman in 1960.² In the following years, more gain media were discovered and in 1966, laser oscillation was obtained from organic chromophores. Sorokin and Lankard³ were the first to see laser operation from such chromophores, namely the organo-metallic compound chloro-aluminium-phthalocyanine at 755.5 nm. The same year, Schäfer *et al.*⁴ observed lasing from a cyanine dye in solution. Within this chapter, a qualitative picture of the changes in a molecule upon absorption of a photon is given followed by an explanation of how the Einstein *A* and *B* coefficients can be expressed in terms of the interaction of an atom with an electric field. Finally, it is shown that an organic dye is a four-level laser system.

2.1 - Basic Properties of Organic Compounds

2.1.1 - The Conjugated System

Organic dyes show a strong absorption band in the visible light range. This property can be affiliated to an extended system of conjugated bonds: alternating single and double bonds. These double bonds are usually of the C = C form, but conjugation can extend to include lone pairs on Nitrogen or Oxygen atoms.



The single bonds are σ bonds. They can be constructed from the overlap of two s atomic orbitals, one s and one p orbital (sp , sp^2 , or sp^3 hybrid), or 2 p atomic orbitals that have their lobes aligned end-to-end. Here, the probability to find an electron is largest along the axis joining the nuclei of the bonded atoms, and has a rotational symmetry along this axis. These σ electrons are tightly bound to the nuclei and high energies corresponding to the ultraviolet spectral region (wavelengths smaller than 170 nm) are required to promote them to higher-lying molecular orbitals. Figure 2.1 shows the construction of a sigma bond from two sp^3 and is taken from [5].

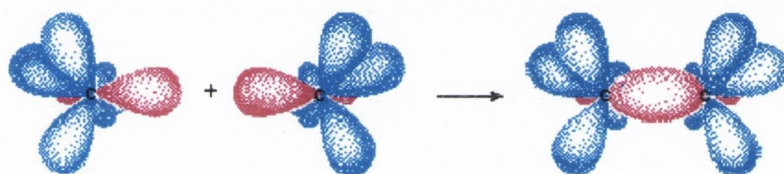


Figure 2.1 The formation of a σ bond from 2 sp^3 hybrids.

The double bonds in a conjugated molecule on the other hand, are made of both a σ and a π bond. A π bond is constructed from two $2P_z$ atomic orbitals, the lobes of which overlap sideways. Here, the probability of finding an electron is largest above and below the axis joining the two atoms and has a rotational symmetry along a line through the nucleus and perpendicular to the σ bond. When an electron is involved in a π bond, it is weakly bound compared to when it is involved in a σ bond. Hence the σ molecular orbitals have to be filled first in order to stabilise the molecule.

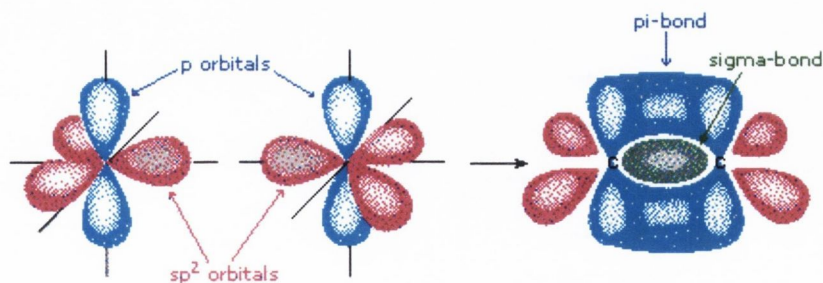


Figure 2.2 The formation of a π bond from 2 P_z orbitals. A σ bond is also formed by 2 sp^2 hybrid orbitals.

The π bonds give the conjugated molecule a planar structure as the bond energy is highest and the molecule most stable when the symmetry axes of the P_z lobes are parallel. Figure 2.2 shows the construction of a π bond from two such P_z orbitals and is taken from [5].

As mentioned before, π electrons are not tightly bound to the nuclei. In fact, for an extended system of conjugated bonds, the P_z orbitals on neighbouring nuclei overlap and the π electrons are free to move over the full conjugation length (Fig. 2.3, taken from [6]). Hence, these electrons are shared by all the nuclei of the conjugated system and are said to be delocalised.

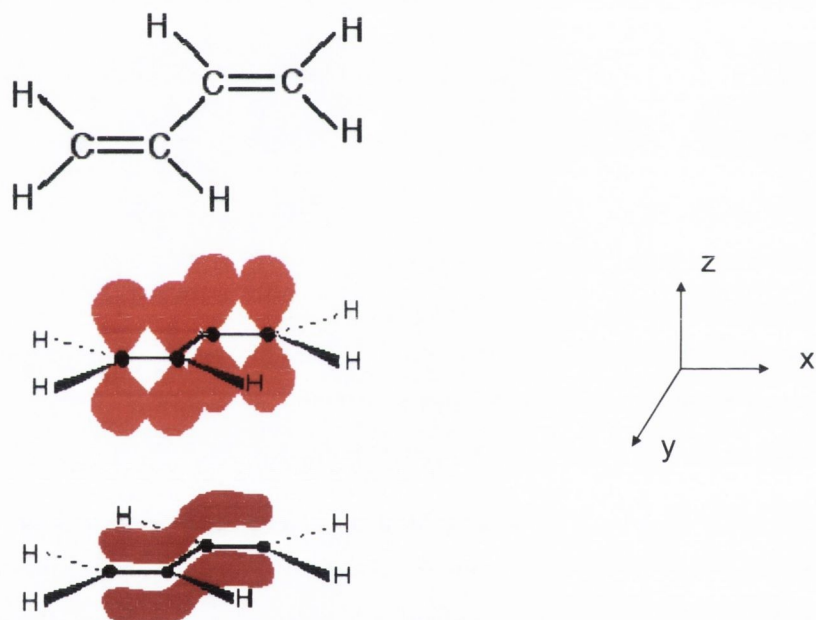


Figure 2.3 A bonding molecular orbital (bottom: red) in Butadiene (top: molecular structure) constructed from the overlap of four P_z orbitals.

All the aforementioned molecular orbitals are of the bonding type. However, molecular orbital theory says that, first the linear combination of a certain number of atomic orbitals should give an equal number of molecular orbitals. Second, there is an antibonding orbital for every bonding one. A particular bonding molecular orbital is lower in energy than the corresponding antibonding one. An antibonding orbital may have a σ symmetry (similar charge distribution to a σ bond) and is called a σ^* orbital, or a π symmetry (similar charge distribution to a π bond) and is called a π^* orbital. Lone pairs on Nitrogen or Oxygen atoms in contact with a conjugated system

can contribute to its conjugation, but not to the stability of the molecule. The corresponding molecular orbitals are termed nonbonding.

2.1.2 - Light-matter Interaction in Laser Dyes

In a conjugated molecule, the state in which all the electrons lie in the bonding or non-bonding orbitals with the lowest possible energy is called the ground state and is denoted by S_0 . When a molecule absorbs radiation, an electron is promoted from a bonding or non-bonding orbital to an antibonding orbital. In the case of organic dyes, where absorption is in the 200-800 nm range, the transitions are $n \rightarrow \pi^*$ or $\pi \rightarrow \pi^*$.

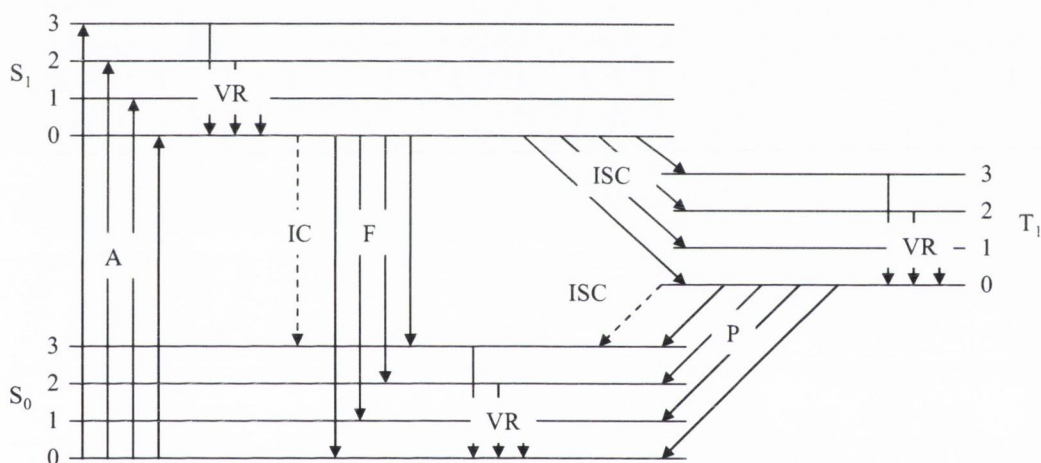


Figure 2.4 Perrin-Jablonski diagram with two singlet states (S_0 , S_1) and one triplet state (T_1). The molecule undergoes (A) absorption (VR) vibrational relaxation (IC) internal conversion, (F) Fluorescence, (ISC) intersystem crossing and (P) phosphorescence.

When in its ground state, a molecule is governed by Pauli's exclusion principle. Each molecular orbital is occupied by two electrons with opposite spin, resulting in a total spin of zero and S_0 is said to be a singlet state. Once an electron is promoted to an excited state, the two unpaired electrons are not required to have opposite signs as Pauli's exclusion principle no longer holds. If the spins stay anti-parallel upon excitation, the excited state is again a singlet state (S_1 , S_2 , S_3 ...). If on the other hand, the spins are parallel resulting in a total spin of one, they are called triplet states (T_1 , T_2 , T_3 ...).

The Perrin-Jablonski diagram (Fig. 2.4) is a convenient method of visualising the transitions between the different states (only S_0 , S_1 , and T_1 are considered here) that a molecule can undergo. Not shown in the diagram are absorption to higher lying singlet states ($S_1 \rightarrow S_2, S_3, \dots$) and triplet-triplet absorption ($T_1 \rightarrow T_2, T_3, \dots$). In organic dyes, a molecule can be lifted from the S_0 to the S_1 state by absorption of visible light. Both states are manifolds due to the coupling of the electronic states to the vibrations of the molecule. A dye molecule has typically 50 or more atoms giving rise to 150 or more normal vibrations, with each electronic level having a set of vibrational levels. Furthermore, each vibrational level has an associated set of rotational sub-levels due to collisions between the dye and solvent molecules (in solution) or phonons (in solid-state). The energy levels in the S_0 state are populated according to Boltzmann statistics. Once in the excited state, the molecule relaxes down to the lowest vibrational level of S_1 (this mechanism is known as vibrational relaxation). The energy lost by the molecule during this process is converted to heat. Next, three processes compete to deactivate the molecule from the S_1 state:

- Internal conversion, whereby an excited molecule goes from S_1 to S_0 through the overlap of their respective lower-lying and higher-lying vibrational levels, or by the quantum mechanic effect of tunnelling. The probability of the latter is inversely proportional to the energy gap between the low-lying S_1 and high-lying S_0 vibrational states.
- Fluorescence, the molecule decays from S_1 to S_0 by emitting a photon. Only few dye molecules (e.g. azulene and its derivatives) decay radiatively between the S_2 and S_0 states.⁷ In general, excitation to S_2 is followed by rapid internal conversion to S_1 .
- Singlet-triplet intersystem crossing, the molecule goes from a S_1 to a T_1 state in a mechanism similar to internal conversion but involving a spin change. The T_1 manifold lies lower in energy than the S_1 manifold because there is a less electronic repulsion in the T_1 states.

Once in T_1 state, the molecule can be excited into higher lying triplet states (T_2 , T_3, \dots) or decay radiatively to S_0 . The latter mechanism is called phosphorescence and involves a spin change and since photons carry no spin, the transition is forbidden. In other words, the phosphorescence lifetime is very long compared to the fluorescence

lifetime. The characteristic times associated with all these processes are given in Table II-I.

Table II-I The characteristic times of radiative and non-radiative processes in dye molecules.

Process	Characteristic time
Absorption	10^{-15} s
Vibrational relaxation	10^{-12} s - 10^{-10} s
Fluorescence	10^{-10} s - 10^{-7} s
Intersystem crossing	10^{-10} s - 10^{-8} s
Internal conversion	10^{-11} s - 10^{-9} s
Phosphorescence	10^{-6} s - 1 s

2.2 - Atom-field Interactions

In the previous section, a qualitative description of absorption, fluorescence, and the accompanying processes in organic dyes was given. Here, the time-dependent Schrödinger equation for atom-field interaction is solved to account for stimulated absorption and emission.

2.2.1 - The time-dependent Schrödinger Equation

The theory underlying the atom-field interaction is taken from [8]. We solve the time-dependent Schrödinger equation for an atom with two energy levels E_1 and E_2 in the presence of a light wave of angular frequency ω . Schrödinger's equation reads:

$$\hat{H}\Psi = i\hbar \frac{\partial \Psi}{\partial t} \quad (2.1)$$

where \hat{H} is the Hamiltonian, Ψ is the wavefunction, and \hbar is Planck's constant. The energy difference between the two levels is given by

$$E_2 - E_1 = \hbar\omega_0 \quad (2.2)$$

The light wave angular frequency ω is related to the resonance frequency ω_0 by $\omega = \omega_0 + \delta\omega$ where $\delta\omega \ll \omega_0$. Exact resonance thus corresponds to $\delta\omega = 0$. The standard technique to solve an equation such as Eq. 2.1, is to split the Hamiltonian into a time-independent part \hat{H}_0 which describes the atom in the absence of an external field, and a perturbation \hat{V} which accounts for the light-atom interaction

$$\hat{H} = \hat{H}_0 + \hat{V} \quad (2.3)$$

The time-independent Schrödinger equation for the unperturbed atom is given by

$$\hat{H}_0 \Psi_m = i\hbar \frac{\partial \Psi_m}{\partial t} = E_m \Psi_m \quad (2.4)$$

for the m th atomic level. It has two possible solutions, one for each energy level

$$\Psi_m(\vec{r}, t) = \Psi_m(\vec{r}) \exp(-iE_m t/\hbar) \quad \{m = 1, 2\} \quad (2.5)$$

Equation 2.5 is then used to construct the general solution of the time-dependent Schrödinger equation

$$\Psi(\vec{r}, t) = c_1(t) \psi_1(\vec{r}) e^{-iE_1 t/\hbar} + c_2(t) \psi_2(\vec{r}) e^{-iE_2 t/\hbar} \quad (2.6)$$

where the time-dependent amplitudes $c_m(t)$ satisfy the normalisation requirement

$$\sum_m |c_m(t)|^2 = 1 \quad (2.7)$$

On substituting the wave function given in Eq. 2.6 into Eq. 2.1 with \hat{H} given by Eq. 2.3, and making use of Eq. 2.4, we find

$$c_1 \widehat{V} \psi_1 e^{-iE_1 t/\hbar} + c_2 \widehat{V} \psi_2 e^{-iE_2 t/\hbar} = i\hbar \dot{c}_1 \psi_1 e^{-iE_1 t/\hbar} + i\hbar \dot{c}_2 \psi_2 e^{-iE_2 t/\hbar} \quad (2.8)$$

Now, on multiplying by ψ_1^* or ψ_2^* , integrating over space, and making use of

$$\int \psi_m^* \psi_n d^3\vec{r} = \delta_{mn} \quad (2.9)$$

where $m, n \in \{1, 2\}$, and δ_{mn} is the Kronecker delta function. We find that

$$\dot{c}_m(t) = -\frac{i}{\hbar} (c_m(t) V_{mm} + c_n(t) V_{mn} e^{-i\omega_n t}) \quad (2.10)$$

$$\text{where } V_{mn}(t) \equiv \langle m | \widehat{V}(t) | n \rangle = \int \psi_m^* \widehat{V}(t) \psi_n d^3\vec{r} \quad (2.11)$$

In the semi-classical approach, the dipole-field interaction causes a shift in the energy of the atom given by

$$\widehat{V}(t) = e\vec{x} \cdot \vec{E} = exE_0 \cos \omega t = \frac{exE_0}{2} (e^{i\omega t} + e^{-i\omega t}) \quad (2.12)$$

where the electric field $\vec{E} = (E_0, 0, 0) \cos \omega t$ and is aligned with the dipole moment $e\vec{x}$. The substitution of Eq. 2.12 into Eq. 2.11, yields the matrix element

$$V_{mn}(t) = \frac{eE_0}{2} (e^{i\omega t} + e^{-i\omega t}) \int \psi_m^* x \psi_n d^3\vec{r} \quad (2.13)$$

The dipole matrix element μ_{mn} is given by

$$\mu_{mn} = -e \int \psi_m^* x \psi_n d^3\vec{r} \equiv -e \langle m | x | n \rangle \quad (2.14)$$

Equation 2.13 then becomes

$$V_{mn}(t) = -\frac{E_0}{2} (e^{i\alpha t} + e^{-i\alpha t}) \mu_{mn} \quad (2.15)$$

The operator x has odd parity and since atomic states have either even or odd parities, $\mu_{11} = \mu_{22} = 0$. Moreover, the dipole matrix element represents a measurable quantity and must be real, $\mu_{21} = \mu_{12}^*$ which implies that $\mu_{21} = \mu_{12}$. Hence Eq. 2.10 reduces to

$$\dot{c}_m(t) = i \frac{\Omega_R}{2} \left(e^{i(-1)^n(\omega - \omega_0)t} + e^{-i(-1)^n(\omega + \omega_0)t} \right) c_n(t) \quad (2.16)$$

where the Rabi frequency reads

$$\Omega_R = \left| \frac{E_0 \mu_{12}}{\hbar} \right| \quad (2.17)$$

2.2.2 - Einstein's Coefficients

Let us examine Eq. 2.16 in the weak-field limit where the interaction between the atom dipole and the driving field is small. The atom is assumed to be in the lower level ($c_1(0) = 1$, $c_2(0) = 0$) when the light is turned on at $t = 0$. In the weak-field limit, we can also make the further approximation that there is little change in the energy level population, $c_1(t) = 1 \gg c_2(t)$. Equation 2.16 then gives

$$\begin{aligned} \dot{c}_1(t) &= 0 \\ \dot{c}_2(t) &= \frac{i}{2} \Omega_R \left(e^{-i(\omega - \omega_0)t} + e^{i(\omega + \omega_0)t} \right) \end{aligned} \quad (2.18)$$

The solution for $c_2(t)$ with $c_2(0) = 0$ is

$$c_2(t) = \frac{i}{2} \Omega_R \left[\frac{e^{-i\delta\omega} - 1}{-i\delta\omega} + \frac{e^{i(\omega+\omega_0)t} - 1}{i(\omega+\omega_0)} \right] \quad (2.19)$$

where we made use of $\omega = \omega_0 + \delta\omega$. According to the rotating wave approximation, for small values of $\delta\omega$, the second term in brackets in Eq. 2.19 can be neglected. The probability $P_{12}(t)$ for the atom to make the transition from level 1 to 2 in time t is given by

$$P_{12}(t) = |c_2(t)|^2 = \left(\frac{\Omega_R}{2} \right)^2 \left(\frac{\sin \delta\omega t/2}{\delta\omega/2} \right)^2 \quad (2.20)$$

Now, let suppose that the light irradiating the atom is from a broad-band lamp. Its spectral energy density $u(\omega)$ must then satisfy

$$\frac{1}{2} c \epsilon_0 E_0^2 = \int u(\omega) d\omega \quad (2.21)$$

Also, the atomic transition line is no longer assumed to be a delta function and is given the width $\Delta\omega$. Substituting Eq. 2.17 into Eq. 2.21 and the result into Eq. 2.20, then yields

$$|c_2(t)|^2 = \frac{\mu_{12}^2}{2\epsilon_0 \hbar^2} \int_{\omega_0 - \Delta\omega/2}^{\omega_0 + \Delta\omega/2} u(\omega) \left(\frac{\sin(\omega - \omega_0)t/2}{(\omega - \omega_0)/2} \right)^2 d\omega \quad (2.22)$$

If $u(\omega)$ is broad compared to the spectral line, it can be replaced by its resonance value $u(\omega_0)$ in Eq. 2.22 and taken out of the integral. Solving the integral then yields

$$|c_2(t)|^2 = \frac{\pi}{\epsilon_0 \hbar^2} \mu_{12}^2 u(\omega_0) t \quad (2.23)$$

Equation 2.23 says that the probability of finding the molecule in level 2 increases

linearly with time.

It was assumed so far that the atomic dipole moment was aligned parallel to the electric field of the light. However, dipoles are usually randomly orientated with an angle θ to the light polarisation and $\vec{x} \cdot \vec{E}_0$ has to be replaced by $\langle xE_0 \cos \theta \rangle = xE_0/3$ when taking the average over θ . The transition probability per unit time W_{12} is then

$$W_{12} \equiv B_{12}^{\omega} u(\omega_0) = |c_2|^2 / t = \frac{\pi}{3\epsilon_0 \hbar^2} \mu_{12}^2 u(\omega_0) \quad (2.24)$$

where B_{12}^{ω} is also known as the Einstein B coefficient for stimulated absorption

$$B_{12}^{\omega} = \frac{\pi}{3\epsilon_0 \hbar^2} \mu_{12}^2 \quad (2.25)$$

Equation 2.25 gives the transition probability for stimulated emission $B_{12}^{\omega} = B_{21}^{\omega} = B^{\omega}$ as shown by Einstein. The transition probability for spontaneous emission (fluorescence) is also known as the Einstein A coefficient and is related to the B coefficient by

$$A^{\omega_0} = \frac{h\omega_0^3}{\pi^2 c^3} B^{\omega_0} \quad (2.26)$$

Einstein derived the A and B coefficients using a thermodynamics treatment.

2.3 - Organic dye: a Four-level Laser System

An organic dye can be understood as a four-level laser system (see Fig. 2.5). At room temperature, only the lowest vibrational level of the S_0 state is substantially populated and is level 0 of this laser system. When a photon is absorbed, the molecule is excited into level 3 made from the vibrational active levels of the S_1

state. After vibrational relaxation has taken place, the molecule reaches level 2, the lowest vibrational level of the S_1 state, which is also the upper laser level. The molecule then decays by photon emission to level 1, the lower laser level, which is made of the vibrational active levels of the S_0 state. The molecule eventually returns to level 0.

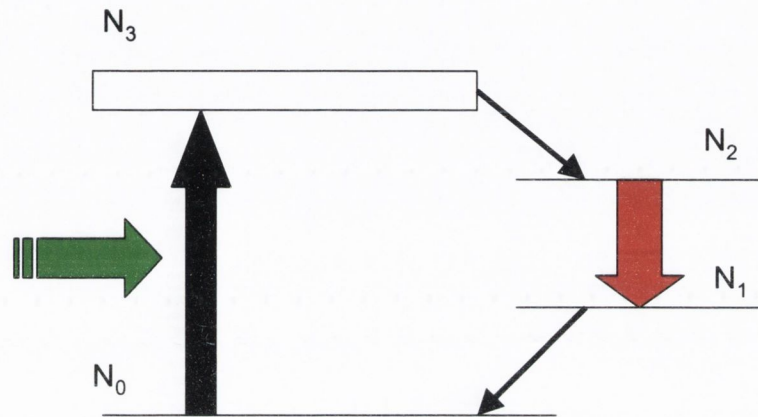


Figure 2.5 Schematic diagram of an organic dye as a four-level laser system.

If we assume that the laser is oscillating on a single mode, and pumping and mode energy densities are uniform inside the gain medium, and that the population in level 1 is negligible, the rate equations are then given by

$$\begin{aligned} \frac{dN_2}{dt} &= R_p - B\phi N_2 - \left(\frac{N_2}{\tau_2} \right) \\ \frac{d\phi}{dt} &= V_a B (\phi + 1) N_2 - \left(\frac{\phi}{\tau_c} \right) \end{aligned} \quad (2.26)$$

where N_2 is the population in level 2, R_p is the pumping rate, ϕ is the photon density, τ_2 is the lifetime of level 2, V_a is the mode volume, and τ_c is the cavity photon lifetime. The factor B is given by $B\phi = B_{12}u(\omega)$, where B_{12} and $u(\omega)$ are taken from the previous section. The product $V_a B N_2$ in the lower equation accounts for spontaneous emission.

2.4 - Summary

All organic dyes owe their colouring properties to an extended system of conjugated bonds, which absorbs strongly in the visible region. The conjugated bonds are made of σ and π bonds with the latter giving the molecule a planar structure. Upon absorption of a photon, an electron is promoted to a higher lying orbital in terms of the energy. The electron returns to the ground-state through radiative decay (fluorescence or phosphorescence) or non-radiative decay (internal conversion). The processes of spontaneous emission, and stimulated absorption and emission, essential to laser operation are given by the Einstein A and B coefficients, respectively. Organic dyes, when fluorescent, form a four-level laser system.

2.5 - References

- 1 A. Einstein, *Physikalische Zeitschrift* **18**, 121 (1917).
- 2 T. H. Maiman, *Nature* **187**, 493 (1960).
- 3 P. P. Sorokin and J. R. Lankard, *IBM J. Res. Develop.* **10**, 162 (1966).
- 4 F. P. Schäfer, W. Schmidt, and J. Volze, *Appl. Phys. Lett.* **9**, 306 (1966).
- 5 <http://www.cem.msu.edu/~reusch/virtualtext/intro3.htm>.
- 6 <http://www.chemguide.co.uk/analysis/uvvisible/bonding.html#top>.
- 7 F. P. Schäfer and K. H. Drexhage, *Dye lasers* (Springer, Berlin, 1977).
- 8 Mark Fox, *Quantum optics: an introduction* (Oxford University Press, Oxford, 2006).

Chapter 3: Materials and Basic Spectroscopy

3.1 - Introduction

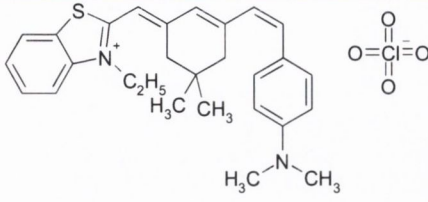
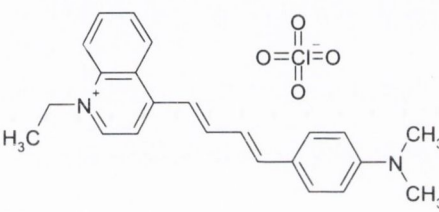
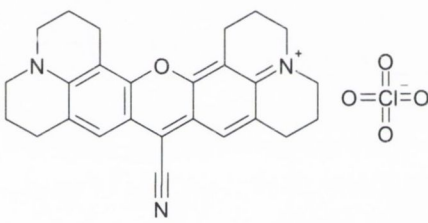
This chapter introduces the different organic compounds that were investigated as suitable materials for optical amplification and lasing in the near-infrared region. As an extension to the theory presented in Chap. 2, density functional theory was used to calculate the change in dipole moment in a solvated chromophore upon the absorption of light. The calculated absorption spectrum was compared to the experimental data. The remainder of the chapter is devoted to basic spectroscopic studies (absorption and fluorescence) of organic dyes embedded in polymer matrices and fluorescence lifetime measurements.

3.2 - Materials

3.2.1 - Laser Dyes

A large number of laser dyes are commercially available with the majority having both their absorption and emission peaks in the 400-700 nm range. In general, laser dyes fluorescing in the near-infrared region tend to have a lower quantum yield than those emitting in the visible region. The reason being that internal conversion from the S_1 to the S_0 state, which competes with radiative decay, becomes more efficient as the energy gap between the ground and excited electronic states gets smaller.¹

Table III-I Molecular structure of three near-infrared emitting dyes and their full chemical names and abbreviations.

Molecular structure	Name	Abbreviation
	2-(6-(p-dimethylaminophenyl)-2,4-neopentylene-1,3,5-hexatrienyl)-3-ethylbenzothiazolium perchlorate	LDS821; Styryl 9
	4-(4-(4-dimethylamino)phenyl)-1,3-butadienyl)-1-ethylquinolinium perchlorate	LDS798; Styryl 11
	9-Cyano-2,3,6,7,12,13,16,17-octahydro-1H,5H,11H,15H-xantheno[9,2,3,4-ij:5,6,7,-i'j')diquinolizin-4-ium perchlorate	LD800; Rhodamine 800

One aim of this project was to find and characterise organic dyes suitable for high gain amplification in the 800 nm region, where perfluorinated polymers have a low-loss region. LDS821, LD800, and LDS798 were purchased from Exciton, Inc to that effect. LD800 was chosen as it is a highly absorptive chromophore in solution.² Kobayashi *et al.*³ had demonstrated laser emission from LDS821 molecules embedded in a polymer matrix. LDS821, LDS798 and LD800 are cationic ions with a perchlorate counter ion. The molecular structure of these three laser dyes, along with their full chemical names and abbreviations, are shown in Table III-I.

The organic dye Styryl 9M has a molecular structure similar to LDS821. The difference lies in the side-group attached to the benzothiazole group. Styryl 9M has a methyl-group in place of the ethyl-group in a LDS821 molecule. The Lambdachrome catalogue² that lists the Styryl 9M, states that the ethyl-derivative shows similar

performance but has a lower photochemical stability in continuous wave pumped dye lasers.

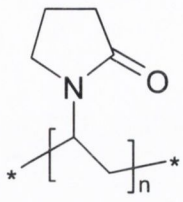
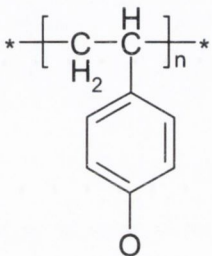
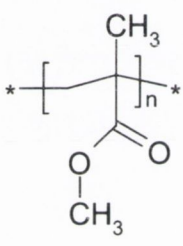
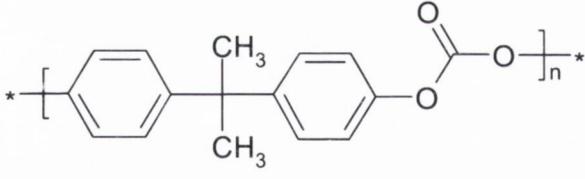
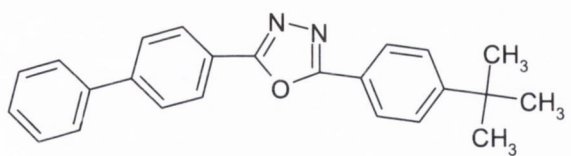
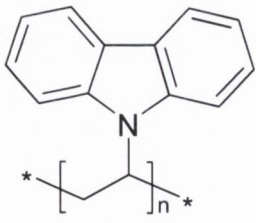
3.2.2 - Organic Matrices

Organic dyes dissolved in a solvent and drop-cast on a substrate tend to crystallise and the resulting neat films are not suitable for optical amplification for several reasons. First, dye molecules are highly absorptive species and a pump beam would be absorbed within the film's surface layer. As the chromophores lying deeper are not excited, they do not contribute to stimulated emission. Second, dye molecules that are in close proximity to each other (10 nm or less), would have their fluorescence quenched.⁴ Dispersing the dye molecules in a polymer matrix has been a popular choice to resolve these issues. When choosing a host polymer, several criteria have to be taken into account.

1. Solubility: the dye molecule should dissolve well in the polymer to prevent aggregation for the reason stated previously and to avoid an increase in scattering losses.
2. Film-forming properties: the polymers should appear flat and transparent, and for the gain measurements, they should give facets with high optical quality where the substrate they are layered upon is scratched and cleaved.
3. Photostability: various mechanisms are responsible for photodegradation in dye molecules and one might be less efficient in one polymer matrix than in the other.
4. Gain factor at a particular wavelength: the fluorescence and gain spectra are polymer dependent.

The molecular structure of the materials used as matrices, along with their common names and abbreviations, are shown in Table III-II.

Table III-II Molecular structure of the organic matrices with common names and abbreviations.

Molecular structure	Name (Abbreviation)
	Polyvinylpyrrolidone (PVP)
	Poly(4-vinylphenol) (PVPh)
	Poly(methyl methacrylate) (PMMA)
	Poly(Bisphenol A carbonate) (PC)
	2-(4-Biphenyl)-5-(4- <i>tert</i> -butylphenyl)-1,3,4-oxadiazole (Butyl-PBD)
	Poly(9-vinylcarbazole) (PVK)

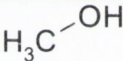
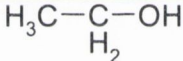
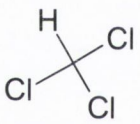
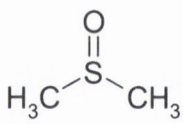
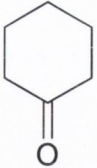
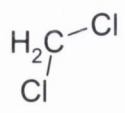
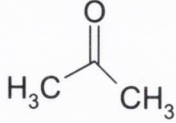

The compounds PVP, PVPh, PMMA, and PC are passive polymers that do not absorb or emit light in the spectral region of interest. Moreover, they do not transport

charge. PVK is a conjugated polymer that also acts as a hole-transporting material. Butyl-PBD is an organic dye that also acts as an electron-transporting material. Both materials absorb in the 300-350 nm range and fluoresce in the blue region.⁵

3.2.3 - Solvents

Organic dyes have the potential to be used in liquid or solid phase. Similar to the case of polymer matrices, the choice of solvent for a gain medium in the liquid phase is important.

Table III-III Chemical structures of the solvents, with common names and abbreviations.

Structure	Name	Structure	Name
	Methanol		Ethanol
	Chloroform		DMSO (Dimethyl sulfoxide)
	Cyclohexanone		DCM (Dichloromethane)
	Acetone		(THF) Tetrahydrofuran

Ionic compounds such as LDS821, LDS798, and LD800 are expected to dissolve well in polar solvents (e.g. alcohols) while an uncharged compound should show good solubility in less polar solvents.⁴ The molecular structure of the solvents, along with their common names and some common abbreviations, are shown in Table III-III.

3.3 - Density Functional Theory

Time-dependent Density Functional Theory (TD-DFT) can be used to calculate the electronic energy levels and the absorption spectrum of a laser dye. In the present case, TD-DFT deals with the response of the molecule, initially in the ground state, when perturbed by an incoming light wave. It is assumed that this perturbation was switched on very slowly (adiabatic approximation) in the distant past, which makes it first order. The perturbation for the case of a molecule interacting with impinging light, is a sinusoidally-varying electric field of angular frequency ω . The response of the associated dipole-moment to the perturbation is quantified by its mean polarisability $\alpha(\omega)$. It can then be shown that $\alpha(\omega)$ is related to the electronic absorption spectrum by⁶

$$\alpha(\omega) = \sum_I \frac{f_I}{\omega_I^2 - \omega^2} \quad (3.1)$$

Here ω_I is the excitation energy ($E_I - E_0$) between ground and excited state. The sum runs over all the possible excited states I of the system. Equation 3.1 implies that the mean polarisability only diverges for $\omega = \omega_I$. The factors f_I are the corresponding oscillator strengths.

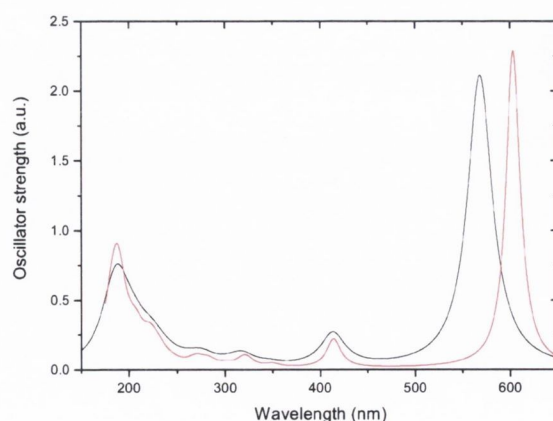


Figure 3.1 The computed absorption spectra of LDS821 in vacuum (black line) and ethanol (red line).

The computation was done at the TD-B3LYP/6-31G* level using the Gaussian 03 software. The perchlorate ion was not taken into account to simplify the calculation. Figure 3.1 shows the calculated absorption spectra of LDS821 for a molecule first in vacuum and then surrounded by ethanol molecules. There is a 35 nm-shift of the main absorption peak when the molecule is dissolved in ethanol, a consequence of the rearrangement of the orbital molecules as the dye is polarised by the solvent molecules. This effect will be discussed to a greater extent in Section 3.4. In vacuum, the transition had an oscillator strength f_l of 2.11, while in ethanol, it was 2.28.

Figure 3.2 shows how well the computed absorption spectrum matches the experimental spectrum (see Section 3.4). The experimental peak is at 589 nm, while the computed value was 603 nm, giving an error of 0.05 eV. The discrepancy can be attributed to neglecting the counter ion in the calculation. The typical error for estimating the excitation energies in TD-DFT is 0.2-0.3 eV.⁷ The linewidth of the computed peak was chosen arbitrarily. TD-DFT gives no information on the broadening suffered by a transition.

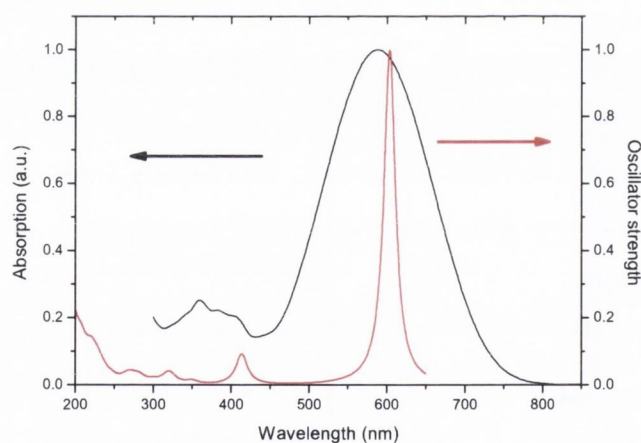


Figure 3.2 The experimental (black line) and computed (red line) absorption spectra of LDS821 in ethanol.

The main constituent of the LDS821 molecule is a stable arrangement of 64 nuclei and 230 electrons. The highest occupied molecular orbital (HOMO) has orbital number 115 with an energy of -7.29 eV in vacuum. The lowest unoccupied molecular orbital (LUMO) is at energy -5.22 eV. The HOMO and LUMO orbitals are depicted in Fig. 3.3. The HOMO has a total dipole moment of 8.61 D, while the

LUMO has a dipole moment of 5.82 D. The x, y, and z components of these dipole moments are given in Table III-IV. There is a change of 2.79 D in the dipole moment upon absorption of a photon. It is worth noting that the dipole moment in the excited state is smaller than in the ground state. Hence the molecule is more polarised in its ground state than in its excited state.

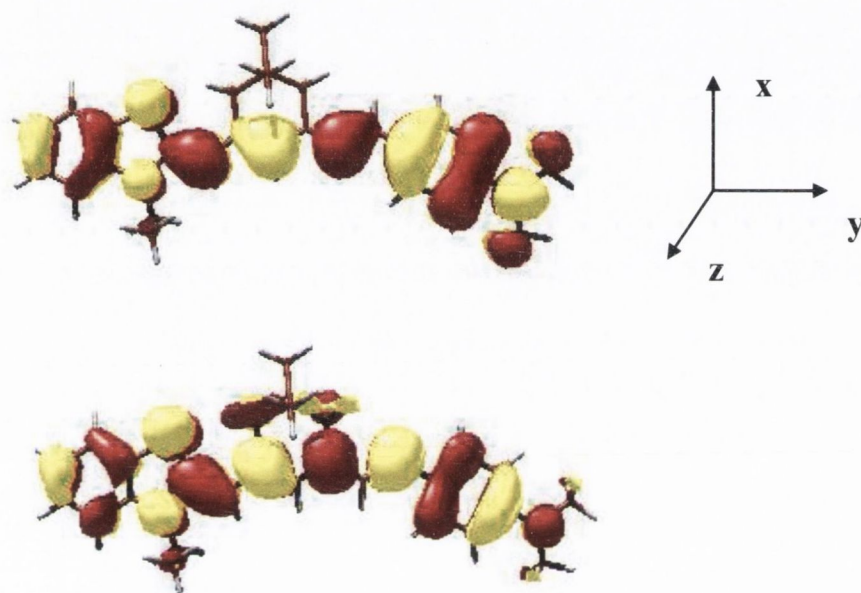


Figure 3.3 The HOMO (top) and LUMO (bottom) of LDS821 in vacuum.

LDS821 is a hexamethine hemicyanine dye and an electron donor-acceptor molecule. The computed HOMO and LUMO of the molecule shown in Fig. 3.3 suggest that there is a charge shift from the (dimethylamino)phenyl group towards the benzothiazolinium group.

Table III-IV The x, y, z components of the dipole moment in ground and excited state.

Dipole moment	Ground state (D)	Excited state (D)
x	2.99	4.24
y	8.06	3.99
z	0.56	0.26
Total	8.61	5.82

3.4- Liquid Phase

A more detailed account of the sample preparation for this section and the following (Section 3.5) is given in appendix A.

3.4.1- Solvent Effect

This section explores the solvent effect on the spectroscopic properties (absorption and emission) of an organic dye. Absorption of a photon by a dye molecule occurs on timescale so short (10^{-15} s) compared to nuclear motion (10^{-13} s) that the accompanying electronic motion ($\mu_g \rightarrow \mu_e$) happens within a rigid nuclear matrix R_n (Franck-Condon principle).⁸ In other words, the orientation of the solvent molecules does not change during absorption. Once in the excited state, the new electronic configuration induces a rearrangement (named vibrational relaxation in Section 2.1.2) of the surrounding solvent nuclei (R_n^*) in order to minimize the free energy. Within this new rigid nuclear matrix, the dye molecule will then decay back to its initial electronic ground state. Finally, the new electronic configuration induces a redistribution of the solvent molecules, which is none other than the initial configuration R_n (Fig. 3.4). The solvent molecules distribution R_n and R_n^* , and hence the dipole moments μ_g and μ_e , will depend on the choice of solvent, and so will the spectroscopic properties of a particular dye.

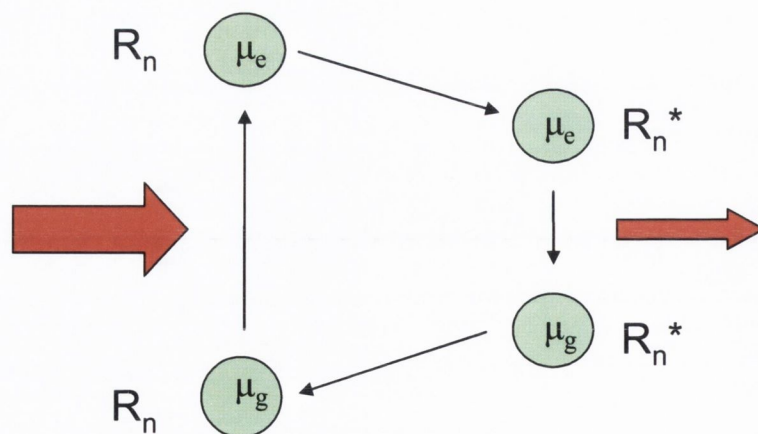


Figure 3.4 The various dipole moments and nuclei frameworks during absorption and emission of a photon.

LDS821 solutions of 0.012 mg/ml were prepared in 8 different solvents and poured into glass cuvettes of 1 cm path length. Steady-state absorbance spectra were recorded with a Cary 1600 series spectrophotometer (Fig. 3.5) with a double beam path. They are broad with full width at half maximum (FWHM) of 160 nm or more.

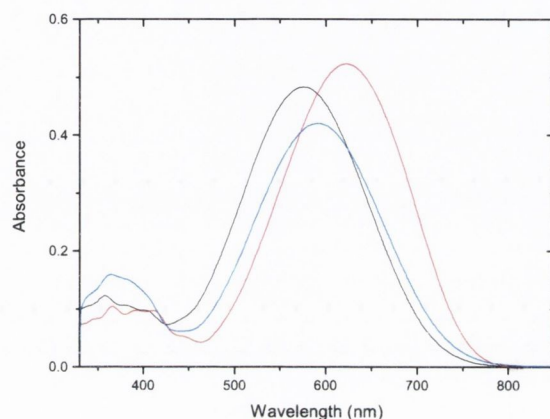


Figure 3.5 Absorbance spectra of LDS821 molecules in methanol (black line), chloroform (red), and cyclohexanone (blue).

From the three solvents shown in the Fig. 3.5, methanol has the highest polarity while chloroform has the lowest (see Table III-VI in the following section). On the whole, there is blue-shift of the absorption spectrum for the more polar solvents. This behaviour can be explained in terms of solute-solvent interaction. The results of the numerical calculation in the previous section showed the HOMO to be more polar than the LUMO. Therefore, when the molecule is dissolved in a polar solvent, the energy of its HOMO will decrease more than the energy of its LUMO. Thus, the energy difference in a polar solvent is larger than in a non-polar solvent, and there is a shift of the absorption spectrum to shorter wavelengths.

To record the fluorescence spectra (Fig. 3.6), a continuous wave argon ion with a pump power of 14 mW was used as the pump source. The emission from the solution was collected with a light-guide at an angle of 90° relative to the excitation source, dispersed in a 0.25m spectrograph and analysed with a charged-coupled device camera. There is also a dependence of the dye's emission spectrum on the solvent's polarity, but it is less pronounced than in the absorption case. All the absorption and fluorescence peaks' wavelengths and the corresponding Stokes' shifts are given in

Table III-V.

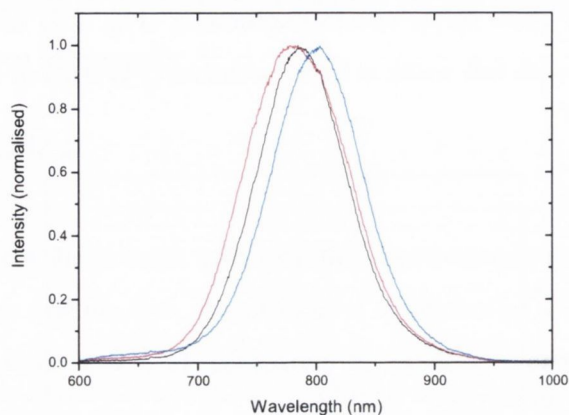


Figure 3.6 Photoluminescence spectra of LDS821 molecules in methanol (black line), chloroform (red), and cyclohexanone (blue).

Table III-V Absorption and emission peaks' wavelengths and Stokes' shift for LDS821 in various solvents.

Solvent	Absorption peak (nm)	Fluorescence peak (nm)	Stokes' shift (nm)
Methanol	575	790	215
Ethanol	587	790	203
Acetone	573	793	220
DMSO	576	808	232
Cyclohexanone	590	799	209
DCM	641	784	143
THF	592	794	202
Chloroform	622	783	161

3.4.2 - Lippert Equation¹

An organic molecule in a solvent can be approximated by a dipole residing at the centre of a sphere (the Onsager cavity) surrounded by an isotropically polarisable

sphere. The energy of the dipole is then given by

$$E_{dipole} = -\mu R_{or} \quad (3.2)$$

where μ is the dipole moment and R_{or} is the orientational reactive field induced in the solvent by the dipole. R_{or} is parallel to the dipole but opposite in direction and its magnitude is given by

$$R_{or} = \frac{1}{2\pi\epsilon_0} \frac{\mu}{a^3} \Delta f \quad (3.3)$$

where Δf is the orientation polarisability of the solvent, ϵ_0 is the permittivity of free space, and a is the Onsager cavity radius. The orientation polarisability is given by

$$\Delta f = \frac{\epsilon - 1}{2\epsilon + 1} - \frac{n^2 - 1}{2n^2 + 1} \quad (3.4)$$

where ϵ is the dielectric constant and n is the refractive index. The Lippert-Mataga equation, converted into SI units from [1] gives the Stoke's shift for a solvated molecule as

$$\tilde{\nu}_a - \tilde{\nu}_f = \frac{\Delta f}{2\pi\epsilon_0 h c a^3} (\mu^* - \mu)^2 + \Delta \tilde{\nu}_v \quad (3.5)$$

where $\tilde{\nu}_a$ and $\tilde{\nu}_f$ are the wavenumbers of the absorption and fluorescence spectra, respectively. The dipole moments for the ground and excited states are given by μ and μ^* , respectively. $\Delta \tilde{\nu}_v$ is the Stokes' shift in vacuum, h is Planck's constant, and c is the speed of light.

Table III-IV gives the Stokes's shift of LDS821 in various solvents of decreasing polarisability. Methanol is the most polar solvent ($\Delta f = 0.308$) while chloroform is the least polar solvent ($\Delta f = 0.150$). The results presented in Table III-VI were

plotted in Fig. 3.7. The data points were fitted with a linear curve which had a slope of 10202.5 cm^{-1} . By using Eq. 3.5 and the value of 2.79 D for the change in dipole moment upon excitation, the Onsager cavity radius was found to be 1.97 Å, which corresponds approximately to the length of the molecule. A small radius means that the interaction between the dye and the solvent molecules is strong.

Table III-VI Solvents along with their dielectric constant⁹ and refractive index⁹ (values given for wavelengths in the 500-600 nm range), polarisability and the Stokes' shift for LDS821.

Solvent	ϵ	n	Δf	Stokes' shift (cm^{-1})
Methanol	32.66	1.3284	0.308	4733
Ethanol	24.55	1.3614	0.289	4377
Acetone	20.56	1.3587	0.284	4841
DMSO	46.45	1.4793	0.263	4985
Cyclohexanone	15.50	1.4510	0.241	4433
DCM	8.93	1.4242	0.217	2845
THF	7.58	1.4072	0.209	4297
Chloroform	4.89	1.4459	0.150	3305

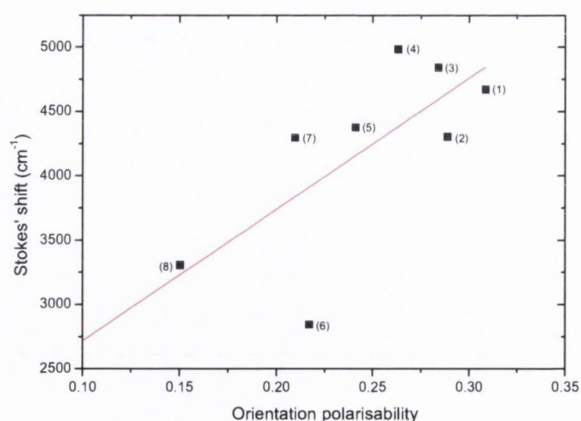


Figure 3.7 Stokes' shift as a function of orientation polarisability for LDS821 dissolved in (1) Methanol, (2) Ethanol, (3) Acetone, (4) DMSO, (5) Cyclohexanone, (6) DCM, (7) THF, and (8) Chloroform.

3.5 - Solid Phase

3.5.1 - LDS821 Samples

3.5.1.1 - Absorption Cross-section Theory

The intensity of a light beam $I(d)$ that has travelled a distance d through a sample with a concentration of N absorbing molecules per cm^3 is expressed by Beer's law

$$I(d) = I_0 e^{-N\sigma d} \quad (3.6)$$

I_0 is the intensity of a light beam before entering the absorbing sample. The term σ is called the absorption cross-section and indicates the strength of the absorption transition. Rearranging Eq. 3.6, and taking a logarithmic base 10 on both sides, yields

$$\log\left(\frac{I(d)}{I_0}\right) = \log(e^{-N\sigma d}) \quad (3.7)$$

The left hand-side of Eq. 3.7 is equal to the optical density, which is also equal to the negative of the absorbance A ,

$$A = -\log\left(\frac{I(d)}{I_0}\right) \quad (3.8)$$

Substituting Eq. 3.8 into 3.7, using $\log(x) = \ln(x)/\ln(10)$, and rearranging, we obtain

$$A = \frac{\sigma Nd}{\ln(10)} \quad (3.9)$$

The density of absorbing molecules in a polymer matrix is given by

$$N = (\%w) \frac{N_a \rho_{pol}}{M_{dye}} \quad (3.10)$$

where M_{dye} is the molar mass of the dye, N_a is Avogadro's number, $(\%w)$ is the dye to polymer weight ratio, and ρ_{pol} is the density of the polymer. The absorption cross-section σ_{abs} is then given by

$$\sigma_{abs} = \frac{\ln 10 M_{dye}}{N_a} \frac{1}{(\%w) \rho_{pol}} \frac{A}{d} \quad (3.11)$$

3.5.1.2 - Results

To prepare the samples, specified amounts of the dye and a polymer (PVP, PVPh, PMMA, or PC) were added to an adequate solvent. In each case, the maximum amount of dye was dissolved in the solution. 100 μ l of the solution was then drop-cast on Pyrex substrates and the samples were left to dry overnight. The absorbance spectrum was taken with the same apparatus as for the liquid state samples. The absorption cross-section spectra are shown in Fig. 3.8.

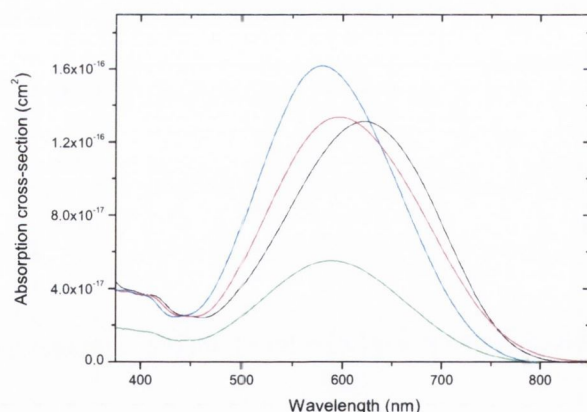


Figure 3.8 Absorption cross-section spectra for LDS821 molecules in PVPh (black line), PC (red), PMMA (blue), and PVP (green).

Table III-VII gives the absorption cross-section values of LDS821 doped into different polymer films at 532 nm. This is the emission wavelength of the second-harmonic of the Nd: yttrium aluminium garnet laser used as the pump source for the

results presented in the subsequent chapters. The thickness of the drop-cast films were measured with a Zygo New View 100 scanning white light interferometer that had a 40× Mirau microscope objective. The density values ρ_{pol} were taken from [10]. The second column gives the ratio of the dye to the inert polymer weights (%w).

The corresponding photoluminescence spectra of LDS821 are shown in Fig. 3.9. The Stokes' shift that varies between 150 and 200 nm depending on the host polymer is large, which would imply low reabsorption of the fluorescence in an amplifier or a laser device. This facilitates population inversion and hence low amplified spontaneous emission or laser threshold.

Table III-VII Absorption cross-section values at 532 nm for LDS821 molecules in various polymer matrices.

Polymer	(%w)	ρ_{pol} (g/cm ³)	z ($\times 10^{-4}$ cm)	A	Stokes' shift (nm)	σ_{abs} at 532 nm ($\times 10^{-16}$ cm ²)
PVP	0.4	1.25	14.59	0.144	193	0.4
PVPh	0.4	1.16	14.76	0.253	161	0.75
PC	0.5	1.20	41.002	1.099	195	0.9
PMMA	0.4	1.20	21.765	0.639	183	1.24

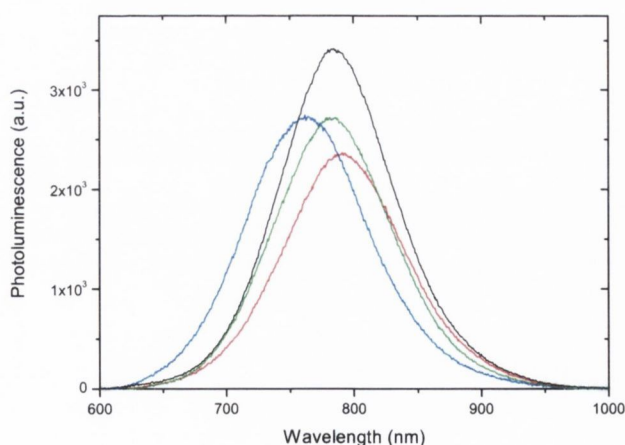


Figure 3.9 Photoluminescence spectra for LDS821 molecules in PVPh (black line), PC (red), PMMA (blue), and PVP (green).

3.5.2 - LD800 and LDS798 Samples

In this section, the basic spectroscopy of LD800 and LDS798 is briefly discussed. The dye LD 800 exhibits two vibronic peaks in both its absorption and emission spectra (Fig. 3.10). This dye is highly absorptive (like most Rhodamine dyes) with an absorption cross-section of $4.5 \times 10^{-16} \text{ cm}^2$ at its peak (701 nm). However, it has a lower value ($1.7 \times 10^{-17} \text{ cm}^2$) at 532 nm, the emission wavelength of the pump source used in this work. Furthermore, there is a Stokes' shift of only 24 nm between the main vibronic peaks, a factor detrimental to laser action.

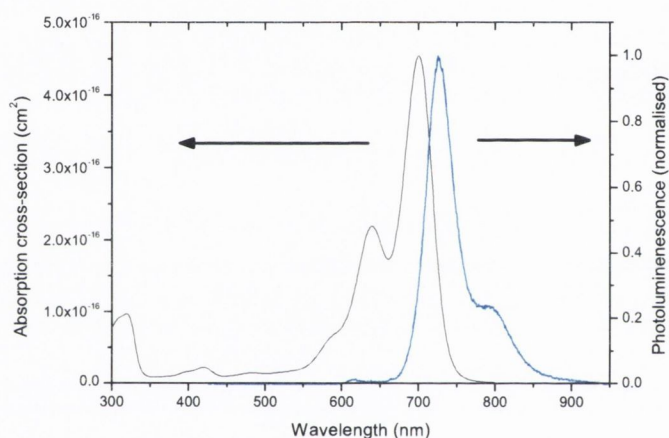


Figure 3.10 Absorption cross-section (black line) and PL (blue line) spectra of LD800 in a PVP matrix.

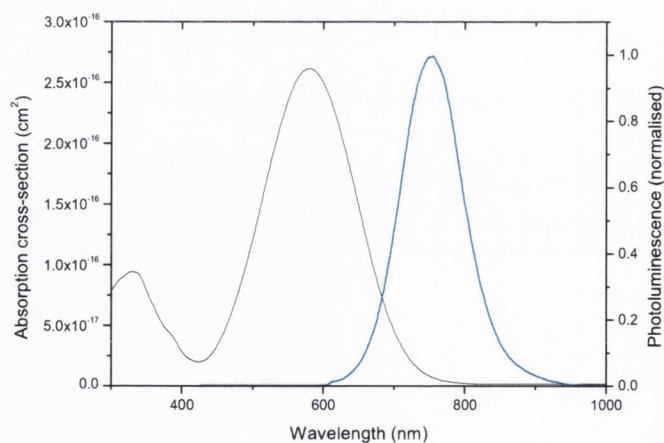


Figure 3.11 Absorption cross-section (black line) and PL (blue line) spectra of LDS798 in a PVP matrix.

LDS 798 has a large Stokes' shift of 171 nm (Fig. 3.11) and the large absorption cross-section of $2 \times 10^{-16} \text{ cm}^2$ at 532 nm. It also has a large FWHM of 102 nm, which has favourable implication for broad-band amplification.

3.6 - Fluorescence Lifetime Measurements

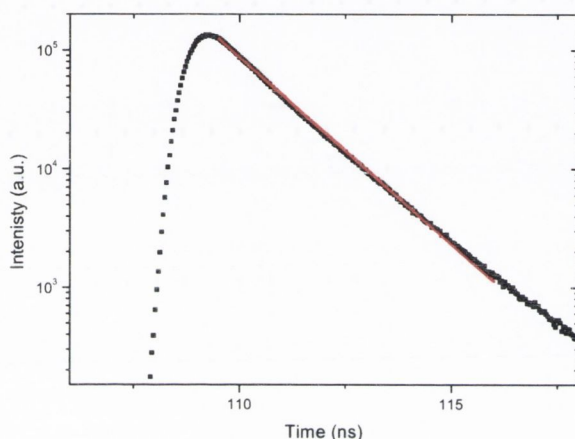


Figure 3.12 Fluorescence intensity recorded as a function of time for a LDS821 doped PVP matrix on a semi-log scale.

The fluorescent lifetime was measured with the MicroTime 200 fluorescence lifetime microscope system from PicoQuant. The excitation source was a laser diode with an emission wavelength of 470 nm, a pulse length of 50 ps and a repetition rate of 40 MHz. The detector was a single photon avalanche diode. The measured intensity $I(t)$ from the sample as a function of the elapsed time t is given by the expression

$$I(t) = Ae^{-t/\tau} \quad (3.12)$$

where A is a constant and τ is the fluorescence lifetime. The fluorescence intensity in Fig. 3.12 was fitted with Eq. 3.12 yielding a value of 1.4 ns for LDS821 in a PVP matrix.

3.7 - Summary

This chapter focused on the basic spectroscopic properties of the different organic materials used in the course of this work. Absorption and emission spectra for the three near-infrared dyes in solvents or solid-state matrices were recorded and analysed. In particular, a blue-shift in the absorption spectrum of the LDS821 molecule in polar solvents was observed. This is in agreement with the results of a numerical calculation based on density functional theory that revealed that LDS821 has a larger dipole moment when in the ground state. A comparison of the three near-infrared dyes absorption spectra when embedded in a polymer showed that LDS798 and LDS821 had a larger cross-section than LD800 at 532 nm. The results presented in this chapter will be used in the subsequent chapters.

3.8 - References

- ¹ B. Valeur, *Molecular fluorescence: principles and applications* (Wiley-VCH, Weinheim, 2002).
- ² U. Brackmann, *Lambdachrome laser dyes* (Lambda Physik GmbH, Goettingen, 1994).
- ³ T. Kobayashi, J.-B. Savatier, G. Jordan, W. J. Blau, Y. Suzuki, and T. Kaino, *Appl. Phys. Lett.* **85**, 185 (2004).
- ⁴ F. P. Schäfer and K. H. Drexhage, *Dye lasers* (Springer, Berlin, 1977).
- ⁵ M. A. Diaz-Garcia, S. F. De Avila, and M. G. Kuzyk, *Appl. Phys. Lett.* **80**, 4486 (2002).
- ⁶ W. Koch and M. C. Holthausen, *A chemist's guide to density functional theory* (Wiley-VCH, Weinheim, 2001).
- ⁷ P. Carloni and F. Alber, *Quantum medicinal chemistry* (Wiley-VCH, Weinheim, 2003).
- ⁸ R. M. Eisberg and R. Resnick, *Quantum physics of atoms, molecules, solids, nuclei, and particles* (John Wiley, New York, 1974).
- ⁹ C. Reichardt, *Solvents and solvent effects in organic chemistry* (Wiley-VCH, Weinheim, 2003).
- ¹⁰ J. E. Mark, *Physical properties of polymers handbook* (AIP Press, New York, 1996).

Chapter 4: Optical Gain Spectroscopy

4.1 - Introduction

This chapter is dedicated to finding an organic dye that would allow high gain amplification at ~ 800 nm. The slab asymmetric waveguide was selected as the amplifying structure and the various theories underlying its functioning are discussed in Section 4.3. The waveguides were fabricated using the spin-coating technique and the net gain coefficients were measured at different pump fluences by use of the variable-stripe-length method.¹ Both the loss coefficient and the unsaturated small-signal gain are given as they are among the important parameters that govern the performance of an amplifier. Next, a waveguide was turned into a lasing device by pumping it over its entire length. Its operating characteristics such as laser threshold and polarisation contrast were measured. Finally, amplified spontaneous emission (ASE) in the near-infrared region was shown from an organic layer that had semiconducting properties.

4.2 - A Bit of History

In 1870, John Tyndall (who hails from county Carlow) gave the Royal Society in London the first practical demonstration of light guiding through total internal reflection (TIR). In his experiment (Fig. 4.1, taken from [2]) water poured from an elevated container to a lower-lying one. Tyndall then directed a beam of sunlight through this water stream, coupling it in on one side and having it emerge further down. The audience saw the light beam following a zigzag path inside the bent path of the water. Tyndall referred to his set-up as a “light-pipe” and it is acknowledged

these days as being a forerunner of the optical fibre used in modern communication technologies.

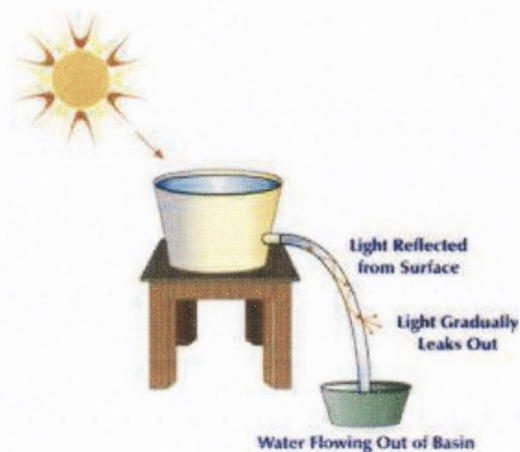


Figure 4.1 A sketch of Tyndall's experiment: a beam of sunlight inside a water stream undergoes multiple reflections at the water-air interface.

4.3 - Theory

4.3.1 - Slab Asymmetric Waveguide Theory

The slab asymmetric waveguide, along with the channel waveguide and the optical fibre, are the common light-guiding devices used in the transmission of information at optical frequencies. The physics underlying the functioning of the former have been outlined in many textbooks.^{3,4}

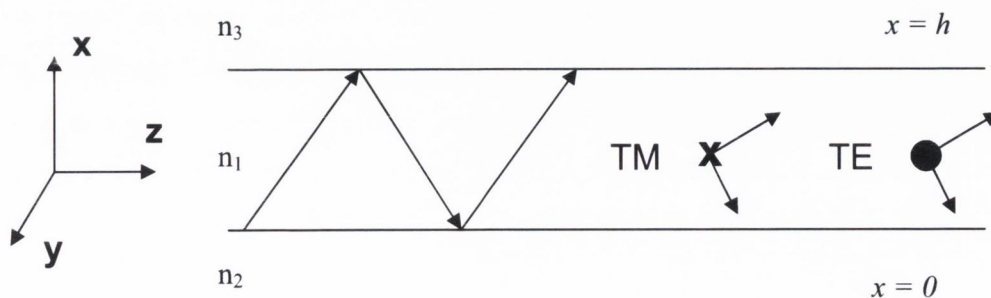


Figure 4.2 Light-guiding in a slab asymmetric waveguide.

Light is confined inside a slab waveguide by TIR. Such a waveguide is made of three layers (Fig. 4.2) with the so-called core sandwiched between two layers of smaller refractive indices: cover and substrate. If cover and substrate are made of the same material (and thus have the same refractive index), the waveguide is said to be symmetric, otherwise it is antisymmetric.

The index profile for the waveguide depicted in Fig. 4.2 is given by

$$n(x) = \begin{cases} n_1 = n_{core}, & 0 < x < h \\ n_2 = n_{substrate}, & x < 0 \\ n_3 = n_{cover}, & x > h \end{cases} \quad \text{where } n_1 > n_2 > n_3 \quad (4.1)$$

4.3.1.1 - Geometric Optics Treatment

In order for a ray to be totally reflected at the interface to a medium of lower refractive index, it has to strike it at an angle Θ larger than the critical angle Θ_{crit} . Starting with Snell's law of refraction, the condition for TIR at each interface is derived as

$$\Theta \geq \begin{cases} \Theta_{12,crit} & \text{with } \sin \Theta_{12,crit} = \frac{n_2}{n_1} \\ \text{or} \\ \Theta_{13,crit} & \text{with } \sin \Theta_{13,crit} = \frac{n_3}{n_1} \end{cases} \quad (4.2)$$

However, not every ray that fulfils the requirement stated in Eq. 4.2 becomes a guided mode. A waveguide, such as the one drawn in Fig. 4.2, should be able to confine light travelling in the positive and negative z direction. For two waves of opposite direction to pass through the same region at the same time, they have to combine to form a standing wave. In other words, incident and reflected waves at a particular point and time should have a phase shift that is a multiple of 2π . This is known as the transverse resonance condition

$$2\kappa h - 2\phi_{12} - 2\phi_{13} = 2\nu\pi \quad (4.3)$$

where κ is the propagation constant, ϕ_{ij} is the phase change at the interface ij ($i, j = 1, 2, 3$) and ν is an integer.

4.3.1.2 - Electromagnetic Treatment

The geometric optics treatment can only be used in the particular case of a waveguide consisting of layers of homogeneous dielectric materials. For general solutions, the electromagnetic treatment has to be used. We will derive the solutions for the case of transverse electric (TE) modes, which have their electric field perpendicular to the xz plane (full circle in Fig. 4.2). The solutions with transverse magnetic (TM) modes (with magnetic field represented by X in Fig. 4.2) will be stated at the end of the section. The starting point of the derivation is the scalar wave equation

$$\nabla^2 E_{yi}(x, z) + n_i^2 k_0^2 E_{yi}(x, z) = 0 \quad (i = 1, 2, 3) \quad (4.4)$$

where E_{yi} is the electric field amplitude in the i th layer and in the y -direction (TE polarisation, see Fig. 4.2), n_i is the refractive index in the i th layer, and k_0 is the wavevector. Equation 4.4 has solutions of the form

$$E_{yi}(x, z) = E_i(x) \exp(-j\beta z) \quad (4.5)$$

The waves described by Eq. 4.5 have their electric field in the y -direction and move at a constant speed in the z -direction. The propagation constant is given by β . Replacing $E_{yi}(x, z)$ in Eq. 4.4 with its value in Eq. 4.5 results in

$$\frac{d^2 E_i}{dx^2} + [n_i^2 k_0^2 - \beta^2] E_i = 0 \quad (4.6)$$

We are looking for solutions to Eq. 4.6 that are modes, i.e. solutions that have their energy confined inside the waveguide. The fields should be standing waves inside the core layer and evanescent fields outside it and are chosen to have the form

$$\begin{aligned}
\text{in the core:} & \quad E_1 = E \cos(\kappa x - \phi) \\
\text{in the substrate:} & \quad E_2 = E' \exp(\gamma x) \\
\text{in the cover:} & \quad E_3 = E'' \exp[-\delta(x - h)]
\end{aligned} \tag{4.7}$$

where the constants κ , γ , and δ are given by

$$\begin{aligned}
\kappa &= \sqrt{n_1^2 k_0^2 - \beta^2} \\
\gamma &= \sqrt{\beta^2 - n_2^2 k_0^2} \\
\delta &= \sqrt{\beta^2 - n_3^2 k_0^2}
\end{aligned} \tag{4.8}$$

The boundary conditions state that the field and its gradient must be continuous at each interface. At the core-substrate interface ($x = 0$),

$$\left. \begin{aligned} E' &= E \cos(\phi) \\ \gamma E' &= -\kappa E \sin(-\phi) \end{aligned} \right\} \rightarrow \tan \phi = \frac{\gamma}{\kappa} \tag{4.9}$$

while at the core-cover interface ($x = h$),

$$\left. \begin{aligned} E'' &= E \cos(\kappa h - \phi) \\ -\delta E'' &= -\kappa E \sin(\kappa h - \phi) \end{aligned} \right\} \rightarrow \tan(\kappa h - \phi) = \frac{\delta}{\kappa} \tag{4.10}$$

By using $\tan(\alpha - \beta) = [\tan(\alpha) - \tan(\beta)] / [1 + \tan(\alpha) \tan(\beta)]$, a standard trigonometrical identity, we can rewrite the left-hand side of Eq. 4.10 as

$$\tan(\kappa h - \phi) = \frac{[\tan(\kappa h) - \tan \phi]}{[1 + \tan(\kappa h) \tan \phi]} \tag{4.11}$$

Substituting the value of $\tan \phi$ from Eq. (4.9) we obtain

$$\left[\tan(\kappa h) - \frac{\gamma}{\kappa} \right] / \left[1 + \tan(\kappa h) \frac{\gamma}{\kappa} \right] = \frac{\delta}{\kappa} \quad (4.12)$$

Finally, after some rearrangement

$$\tan(\kappa h) = \frac{\kappa[\gamma + \delta]}{\kappa^2 - \gamma\delta} \quad (4.13)$$

Equation 4.13 is the eigenvalue equation for the TE modes. In the case of TM modes, it is given by

$$\tan(\kappa h) = \frac{\kappa \left[\left(\frac{n_1}{n_2} \right)^2 \gamma + \left(\frac{n_1}{n_3} \right)^2 \delta \right]}{\kappa^2 - \frac{n_1^4}{n_2^2 n_3^2} \gamma \delta} \quad (4.14)$$

Equation 4.13 and 4.14 are both transcendental equations (they have no analytical solutions), which means that the β -values must be found numerically.

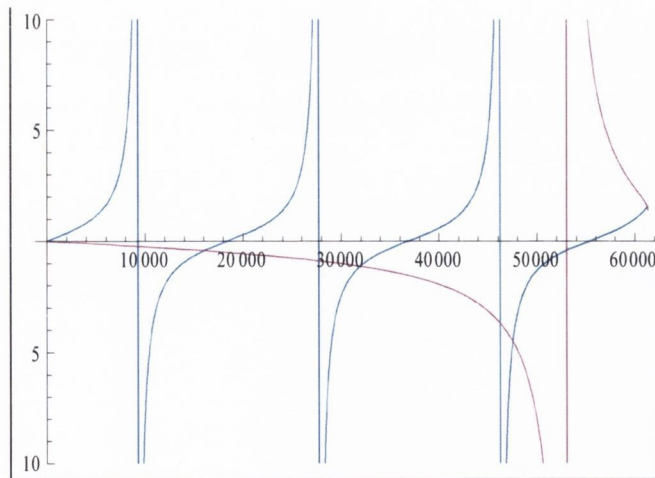


Figure 4.3 The intersection points of the curves are the TE solutions to Eq. 4.13. The abscissa axis is in cm^{-1} , the wave vector units.

The TE and TM modes supported by the waveguides used in the experimental part of this chapter can support were calculated with the Mathematica software. The input

data was

$$\begin{aligned} n_1 &= 1.7 & \lambda &= 820 \text{ nm} \\ n_2 &= 1.5 & h &= 1.7 \mu\text{m} \\ n_3 &= 1 \end{aligned}$$

The functions $\tan(\kappa h)$ (blue line) and $\kappa[\gamma + \delta]/\kappa^2 - \gamma\delta$ (purple line) are drawn in Fig. 4.3 their intersection points gave the solutions to the eigenvalue equation Eq. 4.13. The corresponding β -values were 16026, 31926, and 47478 cm^{-1} . The same waveguides would also support three TM solutions. The electric field intensity patterns for the three TE modes supported by the slab asymmetric waveguide described above are shown in Fig. 4.4. The 1st, 2nd, and 3rd modes have 1, 2, and 3 maxima, respectively. Their fields vary sinusoidally inside the waveguide and exponentially outside, as expected.

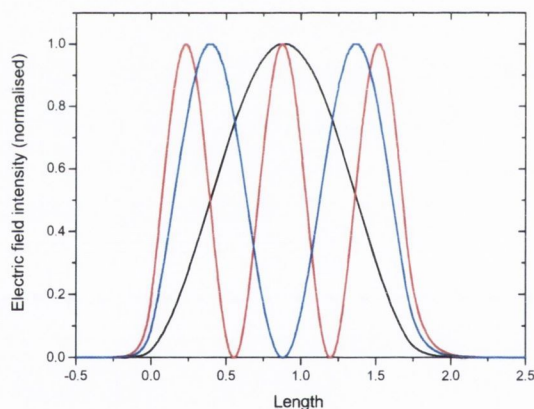


Figure 4.4 Electric field patterns for the three TE modes supported by a 1.7 μm thick waveguide with mode 1 (black), 2 (blue), and 3 (red).

Due to the large difference in refractive indices between the polymer layer and the glass and air layers, the modes are well confined inside the guide. The 1st mode has the best confinement with 99.3% of its field inside the guide. 96.9% of the second mode is confined in the waveguide and 91.6% in the case of the third mode.

4.3.2 - One-dimensional Amplifier Theory

Two methods are commonly used to measure the gain induced by organic molecules. In the pump-probe method,⁵ a probe signal is coupled into the excited region and the gain coefficient is deduced from the change in its intensity after propagation through the waveguide. This approach presents two challenges. First, it requires the use of two beams, for which the spatial and temporal alignment has to be precise. This is a difficult undertaking in these studies, where the samples are only 1.7 μm thick slab asymmetric waveguides and the probe wavelength is in the near-infrared region. Second, ASE from the excited region adds non-negligible noise to the amplified probe beam and has to be taken into account. The variable-stripe-length method by Shaklee *et al.*¹ on the other hand, only requires a pump beam and makes use of the ASE itself to extract the gain.

The underlying theory for the variable-stripe-length method is the one-dimensional amplifier approximation, which works well for planar waveguides with large gain.⁶ It is assumed here that the spontaneous and stimulated emissions are independent of each other in such an amplifier. The light intensity I coming from the waveguide pumped at power P_0 is then given by

$$\frac{dI}{dz} = AP_0 + \gamma I \quad (4.15)$$

where γ is the net single-pass gain, AP_0 is the fraction of spontaneous emission that travels along the amplifier axis and γI is the stimulated emission term. The solution may be obtained by rewriting the equation as

$$\frac{dI}{AP_0 + \gamma I} = dz \quad (4.16)$$

By integrating both sides, we obtained

$$\frac{1}{\gamma} \ln(AP_0 + \gamma I) = l + c \quad (4.17)$$

where l is the amplifier's length and c is the integration constant. Now, reshuffling Eq. 4.17 and taking the exponential on both sides

$$AP_0 + \gamma I = e^{\gamma(l+c)} = Ce^{\gamma l}, \text{ where } C = e^{\gamma c} \quad (4.18)$$

The boundary condition $I(0) = 0$, leads to

$$I = \frac{AP_0}{\gamma} (e^{\gamma l} - 1) \quad (4.19)$$

According to Eq. 4.19, the output intensity will vary with the length of the excitation stripe.

4.4 - Methodology

4.4.1 - Sample Preparation (see Appendix A)

Initial investigations showed that the photostability of the dye was dependent on the host polymer. Kobayashi *et al.*⁷ used poly(1-vinyl-2-pyrrolidone) (PVP) when measuring the gain in drop-cast films doped with LDS821 molecules. In the results presented here, Poly(4-vinyl-phenol) (PVPh) is preferred instead. Thin films made with PVPh or PVP both appeared transparent with no visible scattering. However, LDS821 molecules were more photostable when dispersed in a PVPh matrix. The output of a PVPh film at a particular fluence would remain constant for a longer amount of time than that of a PVP-film. Moreover, under high pump fluences, the PVP films would lose their colour as degradation took place, while the PVPh films would not. These observations indicate that a different mechanism is the main cause for photodegradation in the different polymers.

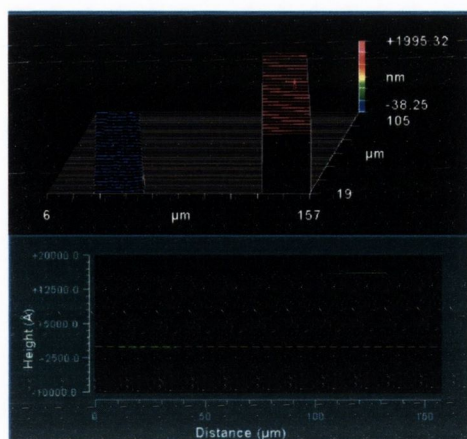


Figure 4.5 White light interferometer software's interface that shows the surface profile of the films, which is uniform.

The slab asymmetric waveguides were prepared by the spin-coating technique. To make up the solution, 2 mg of LDS821 powder and 500 mg of PVPh were dissolved in 2 ml of Cyclohexanone. This dye weight is the maximum that is soluble in such a solution. Next, 100 μl of the solution was dropped on a Pyrex film (2.5×2.5 cm), which was then spun at 3000 rpm. The films were left to dry and after evaporation of the solvent had a thickness of 1.7 μm , as measured by white light interferometry. As a guided mode shape depends on the thickness of the guide, it is important that the films have a uniform surface profile. Figure 4.5 shows that this is the case here. The thickness value varied by less than 0.1 μm over the length of the films, except near the substrate's edge. To avoid the edge bead region, the Pyrex substrate was cleaved by scoring it with a diamond scribe and breaking it. The cleaved edge was used for the gain measurements.

4.4.2 - Experimental Procedure

The variable-stripe-length experiment was set-up as followed (see Fig. 4.6). The excitation source was the second harmonic output of a Q-switched Nd: yttrium aluminium garnet laser. It had a 532 nm wavelength, a 5 ns pulse duration, and a 10 Hz repetition rate. Its beam divergence was measured by recording the transmitted power through a 1 mm pinhole at distances of 10-50 cm of the laser. From the recorded data, a beam waist of 1 mm and a M^2 -factor of 16 were deduced. These factors were then used to calculate the beam propagation through lenses using the

ABCD matrices method.

In the experimental set-up, the laser output was first directed through two polarisers. Rotating the first would allow varying the transmitted beam's power. The second was aligned to only let TM-polarised light through. An angle of 0° between the polarisers meant maximum transmitted output.

The beam was then passed through two cylindrical lenses with a 5 cm focal length and arranged perpendicular to each other. Such a set-up gave the beam a horizontal shape at the sample position.

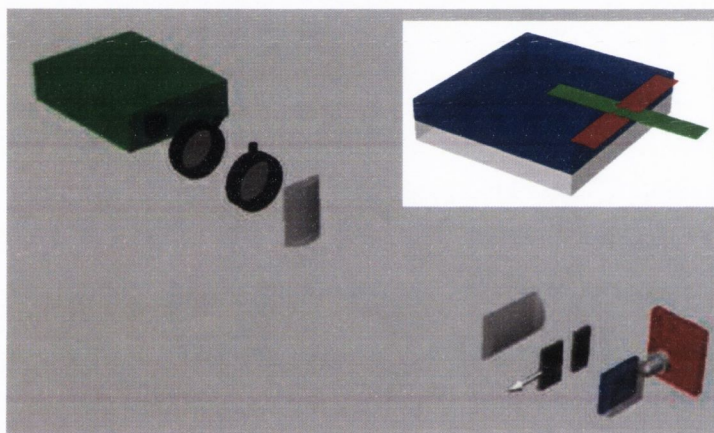


Figure 4.6 Experimental set-up used for the gain spectroscopic studies. Inset: Sketch of the waveguide. The green and red stripes indicate the pump stripe directions (see Fig 4.7 and 4.8).

To control the excitation length, a slit was formed with two razor blades where the first is fixed and the second is mounted on a stepping motor. The latter was controlled by a program written in LabView. The set-up was such that the fixed razor blade and the sample had their edges aligned. The slit width was varied from 0-3 mm in steps of $50\ \mu\text{m}$ by moving the second blade away from the sample. In order to avoid optical feed-back from the sample edge, and therefore laser oscillation, the sample was tilted by a small angle in the plane of the pump stripe. Light emitted from the excited stripe region was collected along the direction of the stripe, through a $40\times$ microscope objective. A filter was used to block the strong scattered light at 532 nm and the transmitted light was analyzed with a spectrograph (0.25 m spectrometer equipped with a 150 grooves/mm grating blazed at 500 nm) attached to

a charge-coupled device camera. The resolution of the detection system was ~ 3 nm. For a better signal-to-noise ratio, integration was taken over 20 shots for all the data presented here and all the measurements were performed under ambient conditions.

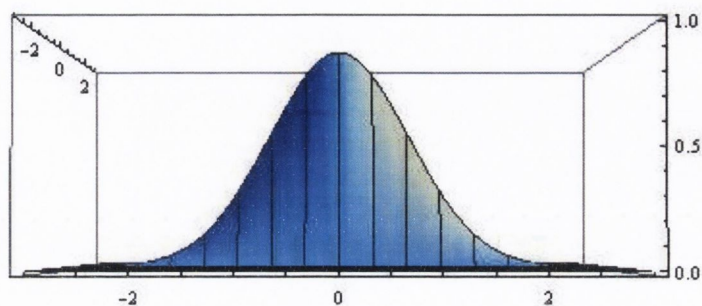


Figure 4.7 Calculated beam profile in the direction perpendicular to the sample edge (along the green stripe in inset of Fig 4.6). The abscissa axis is in cm.

To extract reliable and reproducible gain values, it is important that the beam pump profile is uniform over the excitation length. The distance between first and second lens was therefore made large to obtain a wide pump stripe. In the direction perpendicular to the sample edge, the beam had a calculated length of 3.2 cm (Fig. 4.7) and its intensity peak was aligned with the sample edge. The beam profile on the sample could be approximated to a top-hat profile as the excitation length had a maximum value of 3 mm.

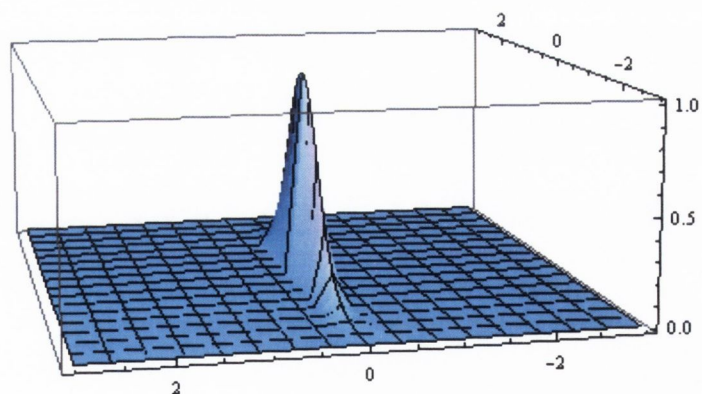


Figure 4.8 Calculated beam profile in the direction parallel to the sample edge (along the red stripe in inset of Fig. 4.6). The abscissa axis is in cm.

The distance between the second lens and the sample was short, close to the focal

length, to make the pump stripe small and thus confine the ASE beam to a narrow region (Fig. 4.8). In this case, the pump width was calculate to be 400 μm . When ASE occurs in a such long, narrow stripe, most of the light is emitted from the ends of the stripe.⁸

4.5 - A Near-infrared Plastic Amplifier

4.5.1 - Initial Tests

This section focuses on the LDS821-doped samples. Initial tests on LD800-doped samples, which have a small Stokes' shift, showed that they had a very high ASE threshold when pumped at 532 nm where they have low absorption (see Chap. 3). One possible way of reducing this threshold is by a Förster energy transfer.⁹ Here, the samples are doped additionally with another chromophore (the donor). The latter is highly absorptive at the pump wavelength and is primarily excited. After excitation, it decays by transferring its energy resonantly and non-radiatively to the initial chromophore (the acceptor). The acceptor then decays radiatively.

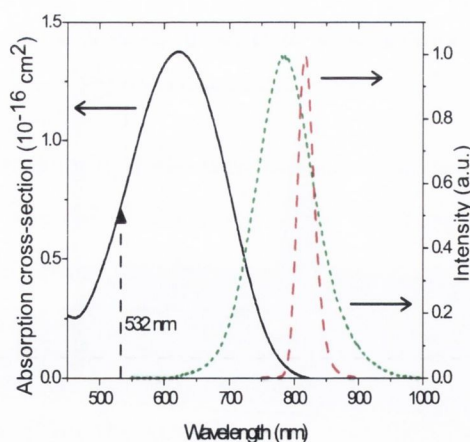


Figure 4.9 Absorption cross-section (black) and steady-state photoluminescence (green) spectra of LDS821 in PVPh together with the ASE spectrum (red) taken at 0.79 mJ/cm^2 .

The samples were doped with the dyes DCM and Rhodamine 6G as they emission

spectra overlap with the absorption spectra of LD800. The doping ratios were 1:1 to 5:1 for Rhodamine 6G/DCM: LD800 but no ASE was observed in the near-infrared region. Therefore at an early stage of these studies, it was decided that LD800 would not be investigated any further. Yamashita *et al.*¹⁰ extensively studied LDS798 and how it compares to LDS821 will be the subject of Section 4.7. ASE emission spectra of LD800 and LDS798 in a PVP matrix will be shown in Section 4.5.7.

In order to optimise the experimental set-up, the lead given in [6] was followed. The slit was positioned close to the sample to minimize the effects of pump beam divergence and diffraction. Moreover, a microscope objective with a small numerical aperture was chosen in order to collect only the light propagating parallel to the amplifier axis. Finally, the microscope objective was positioned so that its focus spot was not inside the sample. Following these rules, the gain coefficients measured were reasonable and reproducible.

Upon photoexcitation, the photoluminescence spectrum showed a dramatic narrowing. The initially broad photoluminescence spectrum (~100 nm at FWHM) collapsed into a much narrower band of approximately 30 nm when the film was pumped at a fluence of 0.79 mJ/cm² (158 kW/cm²) with a 2-mm-long stripe (dashed curve in Fig. 4.9). The absorption cross-section spectrum is also shown in Fig. 4.9. The peaks of the ASE and PL spectra did not match. The waveguide only became transparent to re-absorption for wavelengths beyond 820 nm and it was the emission at this wavelength that experienced the greatest increase.

In all the subsequent measurements, the peak intensity of the ASE spectrum was recorded as a function of amplifier's length.

4.5.2 - Amplifier Regimes

4.5.2.1 - Linear Regime Operation

Light emitted from the facet of a one-dimensional amplifier of very short length is dominated by the isotropic spontaneous emission rather than the more directional ASE signal. The exponential function in Eq. 4.19 can be expanded as a Taylor series

$$e^{\gamma l} = \sum_{n=0}^{\infty} \frac{(\gamma l)^n}{n!} = 1 + \gamma l + \frac{(\gamma l)^2}{2!} + \frac{(\gamma l)^3}{3!} + \dots \quad (4.20)$$

For small values of the gain-length product γl , 2nd order terms and higher can be neglected. Eq. 4.19 then simply reads

$$I(\lambda, l) = AP_0 l \quad (4.21)$$

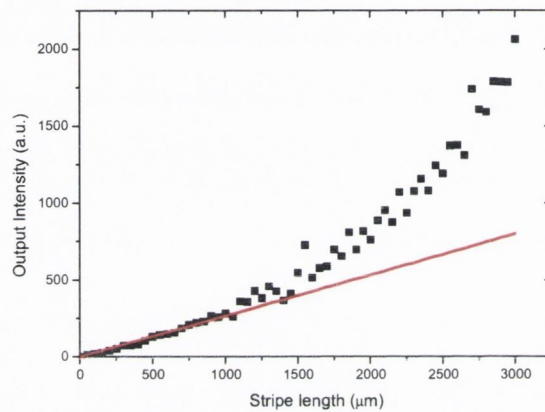


Figure 4.10 Peak output intensity plotted as a function of stripe length at 0.2 mJ/cm^2 at 820 nm . The data points showed a linear increase up to a stripe length of $1000 \text{ }\mu\text{m}$.

Equation 4.21 predicts that the peak output from the amplifier at 820 nm varies linearly with the excitation length. Gain amplification has a negligible effect here and the output is dominated by the spontaneous emission. Figure 4.10 shows how the output intensity varies with stripe length for a sample pumped at 0.2 mJ/cm^2 . The data points can be divided into two regions. Up to an excitation length of $\sim 1000 \text{ }\mu\text{m}$, they can be fitted with a linear curve. In this region, the output is mostly made up of spontaneous emission, which is isotropic and increases proportionally with the number of excited molecules. Above the $1000 \text{ }\mu\text{m}$ limit, the data points start to diverge from the linear fit. The ASE signal has become comparable in intensity to the spontaneous emission. It grows quicker than the spontaneous emission and is well confined in a direction parallel to the waveguide's axis for a narrow excited region.

4.5.2.2 - Amplifier in a Superlinear Regime

Figure 4.11 shows typical plots of the output intensity at 820 nm of LDS821-doped PVPh waveguides as a function of pump stripe length at three different pump fluences. The data points were fitted with Eq. 4.19

$$I = \frac{AP_0}{\gamma}(e^{\gamma l} - 1)$$

The fit was performed with the Origin software, with AP_0 and γ as the adjusting parameters. Since the detection system is not capable of resolving the ASE output pulses, the gain deduced from Eq. 4.19 is the average gain over the 5-ns pulse duration.

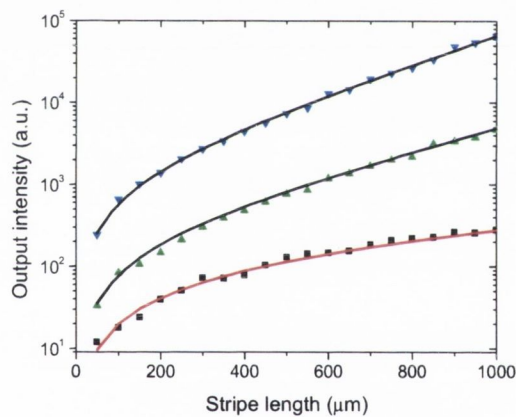


Figure 4.11 Peel output intensity as a function of excitation stripe length for a series of pump fluences: 0.20, 1.18, and 1.57 mJ/cm² from bottom to top, respectively.

By repeating the measurement on several samples, the average gain coefficients were obtained. For the low pump fluence of 0.20 mJ/cm² (40 kW/cm²), the gain coefficient had a value of $5.1 \pm 0.6 \text{ cm}^{-1}$ (Table IV-I in Section 4.5.6). In an unsaturated regime, as it is the case here, the gain coefficient will increase with pump fluence to finally reach a value of $37.2 \pm 2.1 \text{ cm}^{-1}$ at 1.57 mJ/cm² (314 kW/cm²). For large values of γl , the non-exponential term of Eq. 4.19 can be neglected and it then reads

$$I = \frac{AP_0}{\gamma} e^{\gamma l} \quad (4.22)$$

On a semi-logarithmic scale, Eq. 4.22 predicts that data points corresponding to such large values will be arranged on a straight line (Fig. 4.11). For a pump fluence of 1.18 mJ/cm^2 , the amplifiers with a length of more than $500 \text{ }\mu\text{m}$ will be in this regime when experiencing a gain of 27.5 cm^{-1} . The value $e^{27.5 \times 0.05} = 3.95$ would dominate the non-exponential term in Eq. 4.19. The “turn-on” point where an amplifier reaches the superlinear regime occurs at shorter stripe lengths for larger gain coefficients.

4.5.2.3 - Gain Saturation Regime

Equation 4.19 is only valid when the amplifier is operated in the unsaturated regime. As the stripe length is increased in the gain experiment, it will eventually reach a value for which the data points will exhibit a deviation towards smaller intensities than predicted by Eq. 4.19 (Fig. 4.12).

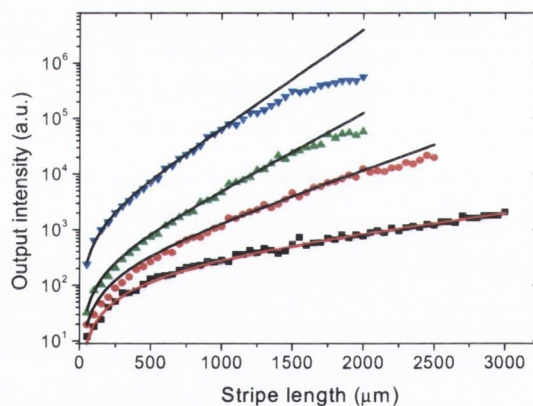


Figure 4.12 Peak output intensity as a function of excitation stripe length for a series of pump fluences: 0.20 , 0.79 , 1.18 , and 1.57 mJ/cm^2 from bottom to top, respectively.

When gain saturation occurs, the gain coefficient decreases and the amplifier becomes less efficient. This gain saturation is a consequence of the finite number of excited molecules available in the amplifier for stimulated emission. As the ASE signal grows, it becomes strong enough to extract the major portion of the inversion

energy into the directional beams by stimulated emission. No saturation of the ASE beam was observed when the samples were pumped at 0.20 mJ/cm^2 over a 3 mm excitation length. The saturation length is a function of the gain coefficient and it was 1.22 mm for a gain of 37.2 cm^{-1} at 1.57 mJ/cm^2 . For larger gain values, the ASE grows quicker and reaches its saturation intensity at shorter stripe lengths.

4.5.3 - Modal gain

The variable-stripe-length method allows varying three different parameters: the length of the excited region, the pump fluence, and the wavelength of the detected amplified luminescence. It is important to investigate the third parameter as organic dyes luminesce over a $100 \mu\text{m}$ wide range and thus have broad-band gain.

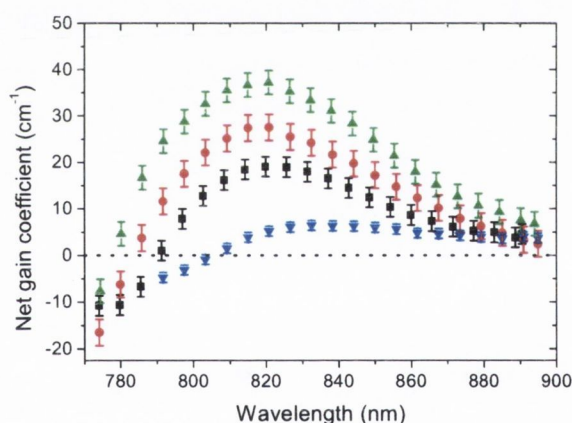


Figure 4.13 Gain spectra for a series of pump fluences: 0.20 , 0.79 , 1.18 , and 1.57 mJ/cm^2 from bottom to top, respectively.

The gain coefficient spectra are shown in Fig. 4.13 For the low pump fluence of 0.2 mJ/cm^2 , the gain peak is at $\sim 830 \text{ nm}$. For greater pump fluences, this peak shifts to shorter wavelengths. This shift can be explained in terms of the ground state's population. With increasing pump fluence, the number density of molecules in the ground state, which are responsible for re-absorption of ASE, decreases, and consequently, the gain peak shifts towards the blue end of the spectrum.

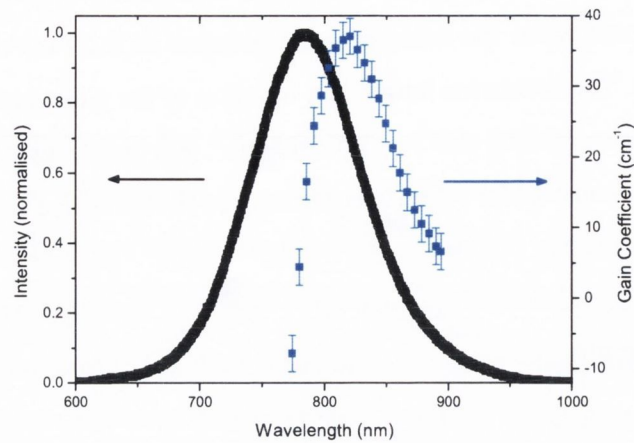


Figure 4.14 Photoluminescence (black line) and gain (blue data points) spectra.

Figure 4.10 showed that PL and ASE spectra did not peak at the same wavelength for the LDS821-doped polymer samples. Figure 4.14 compares PL and gain spectra. The latter is shifted to the red with respect to the former. The gain spectrum is also asymmetric in shape, falling sharply at shorter wavelengths. As pointed out, both characteristics are explained in terms of the self-absorption by the dye molecules. The gain spectrum is also much wider than the ASE spectrum (see Fig. 4.9), which demonstrates the dramatic effect that a small change in gain coefficient has on the emission spectrum.

4.5.4 - Loss Measurements

The performance of an amplifier depends on the inherent loss coefficient. In order for the spontaneous emission to be amplified, it first has to overcome the waveguide losses. The net single-pass gain $\gamma(\lambda)$ in Eq. 4.19 is actually given by

$$\gamma(\lambda) = \Gamma \gamma_{in}(\lambda) - \alpha(\lambda) \quad (4.23)$$

where Γ is the confinement factor, $\gamma_{int}(\lambda)$ is the intrinsic single-pass gain coefficient, and $\alpha(\lambda)$ is the loss coefficient.

The set-up used to measure the loss coefficient is very similar to the one used in the variable-stripe-length experiment. Here, the excited area was kept constant but displaced horizontally relative to the sample edge for a certain pump power. The ASE beam that is generated in the photoexcited region is attenuated by re-absorption and scattering as it propagates through the unpumped region of length d , following the Beer-Lambert law (Fig. 4.15)

$$I_{\alpha} = I_o(\lambda) \exp[-\alpha(\lambda)d], \quad (4.24)$$

where I_{α} is the intensity at the sample edge of an ASE signal of initial intensity I_o .

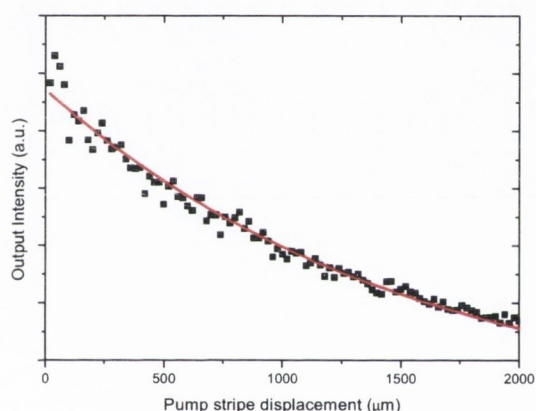


Figure 4.15 Output intensity as a function of pump stripe displacement.

By use of I_o and $\alpha(\lambda)$ as adjusting parameters, the data were fitted to Eq. 4.24 to give a loss coefficient of $7.3 \pm 1.0 \text{ cm}^{-1}$ at 820 nm, where the ASE spectrum has its peak for large pump fluences. This method is easier to perform than other methods that require prism couplers, grating couplers, or end-fire coupling from an external source into the waveguide.

4.5.5 - Pump Saturation

In Fig. 4.16, the net gain coefficient is plotted against the pump fluence. Although the thin films are doped to a maximum, the ratio of dye to polymer weight is nevertheless small. Therefore for large pump fluences, as the ground-state population

is depleted and fewer molecules are available for pump absorption, the excited state population saturates. This saturation effect can be seen in Fig. 4.16, where the net gain coefficient value deviates from a linear increase for pump fluences above 1.57 mJ/cm².

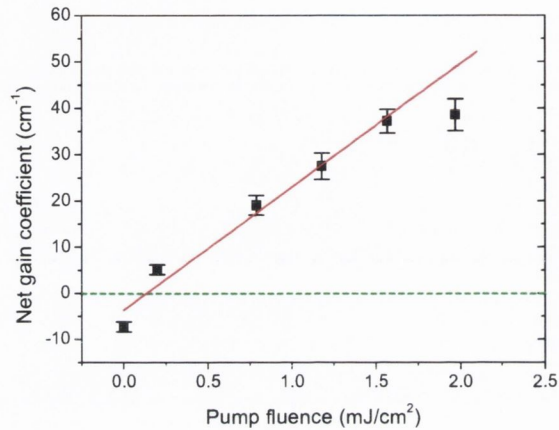


Figure 4.16 Net gain coefficient plotted as a function of pump fluence.

The transparency pump fluence is the value for which gain and loss inside the waveguide are equal. It is given by the intersection between the fit to data points below saturation and the $\gamma(\lambda) = 0$ curve. It takes the value of 0.14 mJ/cm² (28 kW/cm²), which corresponds to an excited-state population of 3.8×10^{16} cm⁻³ or a fractional population of 0.7 %.

4.5.6 - Small-signal Gain

To gain further insight into the behaviour of the amplifier, the small-signal gain was characterised,

$$G(\lambda) = 10 \log[\exp[\gamma(\lambda)L_s]] \quad (4.25)$$

where L_s is the unsaturated excitation stripe length. The net gain coefficient, saturation length, and corresponding small-signal gain are given in Table IV-I. It was found that an unsaturated small-signal gain of 19.7 ± 2.3 dB is achievable in a

1.2-mm waveguide.

Table IV-I For a series of pump fluences, the net gain coefficient $\gamma(\lambda)$, the saturation length L_s , and the small-signal gain are given. The values are taken from Fig. 4.12.

P (mJ/cm ²)	$\gamma(\lambda)$ (cm ⁻¹)	L_s ($\times 10^{-1}$ cm)	$\gamma(\lambda) \times L_s$	G (dB)
0.20	5.1 ± 0.6	–	–	–
0.79	19.0 ± 1.5	1.98 ± 0.17	3.76 ± 0.62	16.3 ± 2.7
1.18	27.5 ± 1.9	1.63 ± 0.12	4.48 ± 0.64	19.4 ± 2.8
1.57	37.2 ± 2.1	1.22 ± 0.07	4.54 ± 0.51	19.7 ± 2.3

Kobayashi *et al.*¹¹ studied the optical gain and saturation behaviour in polymer waveguides doped with the dye B2080 emitting at 500 nm. McGehee *et al.*¹² measured the gain in thin films of the conjugated polymer BuEH-PPV which has its amplified spontaneous peak at 562 nm. Both found that gain saturation sets in for gain-length product values in the range 4-4.5 as it the case here (as can be seen in table IV-I).

4.5.7 - LD800 and LDS798 Samples

Figure 4.17 shows the emission spectra from spin-coated films of LD800 and LDS798 in a PVP matrix. The pump set-up was the same as described previously. LD800 shows stimulated emission on its vibronic peak at 804 nm. The spectrum was taken at a pump fluence of 3.7 mJ/cm² and the FWHM was 12 nm. The ASE threshold is larger for LD800 than for LDS821 films at a pump wavelength of 532 nm. The gain is not large for the thin films under these conditions. LDS798 had its ASE peak at 800 nm with a FWHM of 15 nm at 92 μ J/cm². How the gain coefficient in LDS798 compares to that in LDS821 will be discussed in Section 4.7.

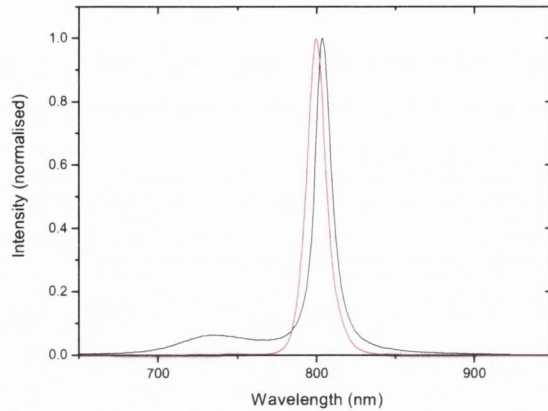


Figure 4.17 ASE emission spectra from thin films of LD800 (black) and LDS798 (red).

4.6 - Fabry-Pérot Cavity Laser

Once stimulated emission is possible, laser oscillation can be achieved by inserting the gain medium into a resonator. An example of such a resonator is the Fabry-Pérot cavity where optical feed-back is provided by two plane mirrors parallel to each other (Fig. 4.18).

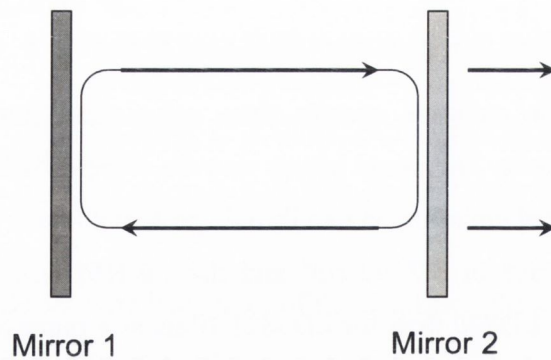


Figure 4.18 Fabry-Pérot cavity where a wave that starts with intensity I_0 has intensity I_R after a round-trip.

Let us consider a wave that starts just inside mirror 1, propagates through the gain medium, is reflected by mirror 2 (reflection coefficient is R_2), propagates again through the gain medium and is reflected by mirror 1 (R_1) to complete the round-trip. At this point, the intensity of the wave is given by

$$I_R = I_0 \delta^2 R_1 R_2 e^{2\gamma_{in} L} \quad (4.26)$$

where I_R and I_0 are the round-trip and original intensities, respectively. The intrinsic single pass gain is denoted by γ , the single-pass loss by δ , and L is the resonator length. At threshold, the gain compensates the losses in the medium and $I_R = I_0$, which leads to

$$\delta^2 R_1 R_2 e^{2\gamma_{in} L} = 1 \quad \rightarrow \quad \gamma_{in} = \frac{1}{2L} \ln \left(\frac{1}{\delta^2 R_1 R_2} \right) \quad (4.27)$$

The previous sections have shown that high gain coefficients are achievable in the near-infrared region with LDS821 molecules embedded in a PVPh matrix. A slab asymmetric waveguide can be made into a laser that does not require external mirrors. Reflection of the travelling beam back into the gain layer is achieved at the waveguide's facets. These polymer-air interfaces have a Fresnel reflectivity R of 0.04 for rays perpendicular to the interface. Thus, a waveguide effectively constitutes a Fabry-Pérot cavity when pumped over its entire length.

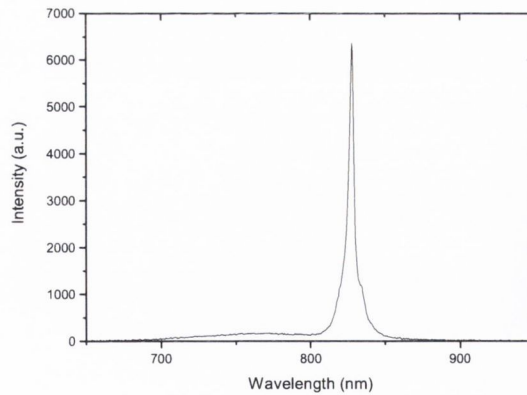


Figure 4.19 Laser emission spectrum from a slab asymmetric waveguide with its facets providing the feed-back with no polarisation selective element.

The laser devices were fabricated by spin-coating a 250 g/l LDS821-PVPh cyclohexanone solution at 3000 rpm onto $12 \times 12 \text{ mm}^2$ SiO_2 substrate, effectively

giving the resonators a length of 12 mm. The samples had a thickness of 1.7 μm . Compared to the VSL experiment, the distance between the two cylindrical lenses was increased from 73.4 to 107 cm to insure a uniform illumination along the samples. The pump stripe had the dimensions $4.51 \times 0.12 \text{ cm}^2$. Figure 4.19 shows the emission from one edge of the Fabry-Pérot laser when pumped at $72.5 \mu\text{J}/\text{cm}^2$. The emission has a sharp peak at 827 nm with a FWHM of only 4.5 nm. No polariser was used between the sample and the detection system.

Now, by inserting a polariser just before the detection system, the polarisation of the laser emission was measured. The polarisation contrast is defined as¹³

$$C = \frac{I_{TM} - I_{TE}}{I_{TM} + I_{TE}} \quad (4.28)$$

where I_{TM} and I_{TE} are the transverse magnetic and transverse electric polarised output signals, respectively. The ratio of TM to TE polarisation was found to be 3.5:1 at the emission peak, which gives a polarisation contrast of 0.55. The dominance of the TM polarisation is possibly explained in terms of the pump TM polarisation. As the dye molecules are randomly orientated in the polymer matrix, those with their dipole moment oriented parallel to the pump's electric field will be preferably excited. The emission from these molecules would then be in the plane of the waveguide and consequently, the overall emission is mostly TM polarised.

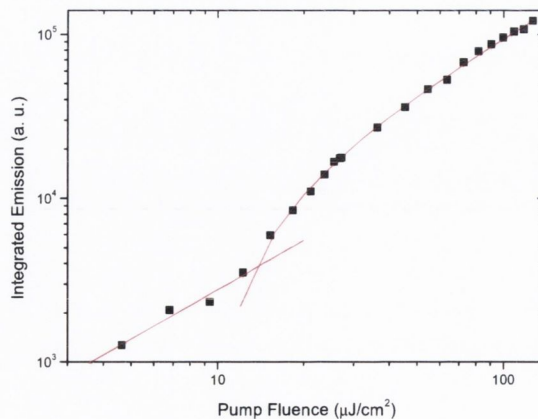


Figure 4.20 Integrated emission spectrum as a function of pump fluence on a log-log plot. The S-curve is indicative of laser emission.

Figure 4.20 is a double logarithmic plot of the integrated emission as a function of the pump fluence. The S-form of the fit to the data points is indicative of laser operation. The laser threshold is given by the intersection of the two lines at $13.5 \mu\text{J}/\text{cm}^2$.

4.7 - Review of Gain Media in the Near-infrared Region

Yamashita *et al.*¹⁰ reported a low ASE threshold from PVP waveguides doped with the near-infrared dye LDS 798. These waveguides had their ASE peaks at $\sim 800 \text{ nm}$ and they exhibited a maximum net gain coefficient of 35 cm^{-1} , which is close to our value of 37.2 cm^{-1} , albeit for a lower pump fluence of $74 \mu\text{J}/\text{cm}^2$ ($93 \text{ kW}/\text{cm}^2$). This difference in pump fluence could be attributed to a few factors. First, a much shorter pump pulse duration of 800 ps is used in [10].

In general, the pump duration strongly affects the efficiency of the creation of excited species. The number density of the excited state is given by

$$N_2 = \sigma_p \frac{NE_p}{\hbar\omega} \frac{\tau_f}{\tau_p} \left[1 - \exp\left(-\frac{\tau_f}{\tau_p}\right) \right] \quad (4.29)$$

where σ_p is the absorption cross section at the pump wavelength, N is the total dye population, E_p is the pump fluence, ω is the angular frequency of the pump light, τ_f is the fluorescence lifetime, and τ_p is the pump pulse duration. Here the quantity in the brackets in Eq. 4.29, which is a function of the ratio of the fluorescence lifetime and pump pulse duration, infers that the subnanosecond pumping is much more efficient than use of 5-ns pump pulses for a gain medium with a nanosecond metastable lifetime. Second, the dye concentration used in our study was $0.4 \text{ wt}\%$ owing to the limited solubility of the dye in the polymer solution as opposed to $2 \text{ wt}\%$ in [10]. Third, the absorption cross-section of LDS821 at the pump wavelength of 532 nm ($0.7 \times 10^{-16} \text{ cm}^2$) is somewhat smaller than that of LDS798 at 565 nm ($1.0 \times 10^{-16} \text{ cm}^2$).

Optical amplification in the near-infrared with an organic dye as the chromophore is a relatively unexplored field (Table IV-II). Casalboni *et al.*¹⁴ have reported a gain coefficient of 10.5 cm^{-1} at 1270 nm from the organic dye IR1051 when incorporated into sol-gel waveguides and pumped at 300 W/cm^2 . Yang *et al.*¹⁵ observed ASE centered a $1.14 \mu\text{m}$ from zirconia-organically modified silicates waveguides doped with the organic dye IR26. The ASE threshold was 8.6 mJ/cm^2 and its FWHM was 15 nm.

Table IV-II Gain coefficients in various gain media.

Gain media	ASE wavelength (nm)	Pump pulse length (ns)	Pump power (kW/cm^2)	Gain (cm^{-1})
LDS821	820	5	314	37.2
GaAs	820	10	10^4	1700
IR1051	1270	-	0.3	10.5
LDS798	800	0.8	92.5	35

Shaklee *et al.*¹ reported a gain of 1700 cm^{-1} at 800 nm for photo-pumped n-doped films of Gallium Arsenide (GaAs). This measurement was done at the very low temperature of 2 K. Semiconductors tend to exhibit larger gain coefficients than organic dyes. The differential gain in semiconductors is of the order of the stimulated emission cross-section in organic dyes (10^{-16} cm^2). However, the emissive species density achievable in the former is larger by orders of magnitude than that in a dye gain medium.

4.8 - Light-emitting Devices

In 1987, Tang *et al.*¹⁶ showed that it is possible to fabricate an organic light-emitting diode (OLED) with high electrical efficiency and thus sparked increased interest in the field of organic electroluminescence. They used a double layer of the hole-transporting small molecule triarylamine and the light emitting and electron

transporting 8-hydroxyquinoline aluminium (Alq_3). This double layer was sandwiched between a transparent indium tin oxide (ITO) anode and an aluminium/magnesium cathode. A natural development to OLEDs would be a current-injected plastic laser. However, such a device has not been achieved yet due to the large required current densities, the absorption losses due to the metallic contacts and charge carriers, and triplets formation. In this section, ASE in the near-infrared is demonstrated from LDS821 doped in an organic layer that is electrically conductive. The Sketch of a OLED is shown in Fig. 4.21.

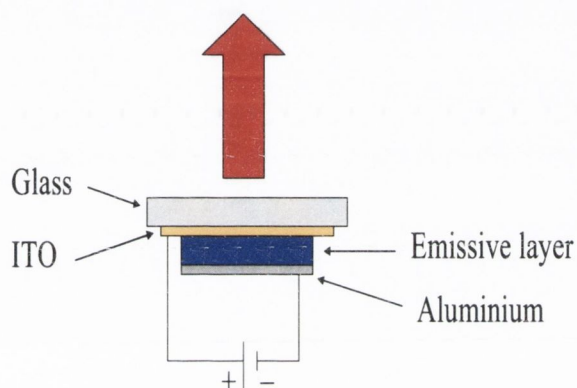


Figure 4.21 Sketch of an organic light-emitting diode.

The LDS 821 bulk powder was not suitable for vapour deposition onto the substrate (dry process). Thermogravimetric analysis and differential scanning calorimetry experiments showed that LDS821 deteriorates ($230\text{ }^\circ\text{C}$) before it melts ($245\text{ }^\circ\text{C}$). Instead, the OLEDs were fabricated by a wet process.

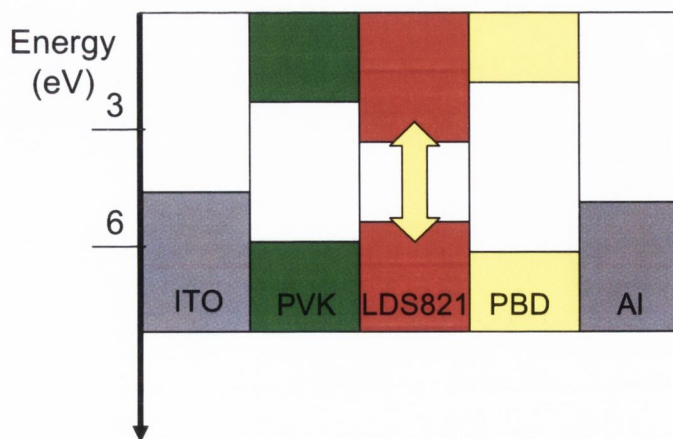


Figure 4. 22: Energy diagram of the materials used in the organic light-emitting diode.

The dye Butyl-PBD, which molecular structure was given in Section 3.2.2, was used as the electron transporting material. It has an electron mobility of $2 \times 10^{-5} \text{ cm}^2/\text{Vs}$.¹⁷ The conjugated polymer Poly(9-vinylcarbazole) (PVK) was used as the hole transporting material. It has a hole mobility of $2 \times 10^{-5} \text{ cm}^2/\text{Vs}$.¹⁸ The ionization potential and the bandgap energy were 5.2 and 2.1 eV for LDS 821, 5.8 and 3.6 eV for PVK, 6.0 and 4.1 eV for Butyl-PBD^{19,20} (see Fig. 4.22). Suzuki¹⁹ therefore suggested that the LDS821 molecules act as effective carrier-trapping and radiative-recombination centres for the EL.

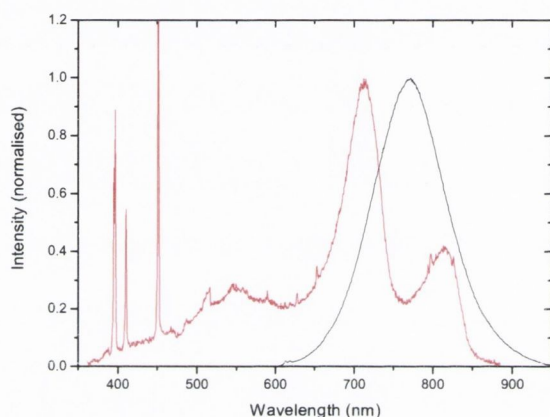


Figure 4.23 Electroluminescence (red) and photoluminescence (black) spectra.

A chloroform solution of PVK, Butyl-PBD (30 wt%) and LDS 821 (1 wt%) was spun-cast onto $1.2 \times 1.2 \text{ cm}^2$ SiO_2 substrate coated with $20 \Omega/\square$ ITO. Next, the films were dried under vacuum and were measured to have a thickness of 50 nm. Finally, the sample was covered with a shadow mask to give six individual LEDs and a 80 nm-thick Aluminium layer was vacuum deposited onto the film. The resulting devices were single monolayer structures with an ITO anode and an Aluminium cathode (Fig. 4.21).

Figure 4.23 shows the electroluminescence (EL) spectrum (red line) seen through the substrate side (bottom emission). The turn-on voltage ranged between 10 and 25 V. The EL in the near-infrared region (700-900 nm) dominated the emission at shorter wavelengths where PVK and Butyl-PBD emit spontaneously. Light emission from the devices was short-lived and the sharp peaks at the shorter wavelengths were

indicative of device failure. Figure 4.24 shows the I-V characteristic of such a device and in this particular case, a current of 0.2 A/cm^2 caused the device to break. One possible explanation is the small thickness of the emissive layer. However, thicker devices failed as well. More important is the fact that the devices were not fabricated in a glove-box and thus, the cathode-organic interface was exposed to atmospheric oxygen and water.

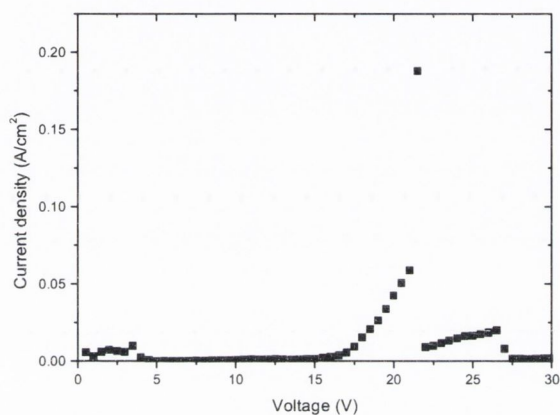


Figure 4.24 I-V characteristic of a LDS821 OLED

Figure 4.23 also shows the photoluminescence (PL) spectrum superimposed upon the EL spectrum. The PL has a peak at 770 nm while the EL has two peaks at 712 and 814 nm. Kobayashi *et al.*⁷ observed a second peak in the 700-750 spectral region at shorter wavelengths for LDS821-doped PVP waveguides at high pump fluences.

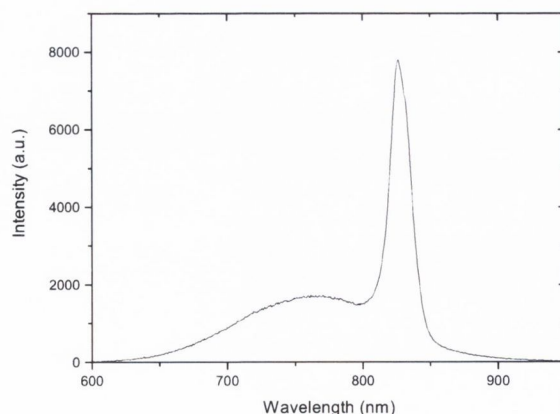


Figure 4.25 ASE spectrum of LDS821 dispersed in a film with semiconducting properties.

This peak could be of the same origin as the 712 nm peak in the EL spectrum and both caused by degradation. In the work published by Suzuki,¹⁹ the EL matched the PL.

Figure 4.25 is the emission from the emissive layer discussed above on an ITO-glass substrate. The sample was pumped over its entire length and the spectrum has an ASE peak at 826 nm with a FWHM of 20 nm. No input-output characteristic could be taken as photodegradation was important at large pump fluences. The spectrum shown in Fig. 4.25 was taken at 1.25 mJ/cm^2 . Finally, the thin films were coated with a layer of Aluminium by vacuum deposition. Such devices resemble the LEDs fabricated previously. When pumped through the ITO side, these films showed only spontaneous emission even for high pump fluences. By increasing the pump beam even further, the pump beam will eventually remove the aluminium and only then will spectral narrowing occur. It can be concluded that aluminium is not suitable as cathode material for ASE operation.

4.9 - Summary

In summary, a large gain coefficient of $37 \pm 2.1 \text{ cm}^{-1}$ and small-signal gain of $19.7 \pm 2.3 \text{ dB}$ were demonstrated at 820 nm in 1.2 mm long luminescent polymer waveguides under nanosecond photopumping. This is the largest gain reported to date for organic gain media operating in the near-infrared region of the spectrum. It was also found that the loss coefficient has a value of 7.3 cm^{-1} and the transparency fluence has a value of 0.14 mJ/cm^2 . Laser emission was achieved by incorporating the organic dye into a Fabry-Pérot cavity. These results will provide an impetus for the development of a compact photopumped amplifier operating in the 0.8- μm communication band. Finally, LDS821 dispersed into a film with semiconducting properties showed ASE operation. An adequate cathode material needs to be found to obtain ASE from films with the structure of an OLED.

4.10 - References

- ¹ K. L. Shaklee, R. E. Nahory, and R. F. Leheny, *J. Lumin.* **7**, 284 (1973).
- ² <http://www.fiber-optics.info/fiber-history.htm>.
- ³ R. R. A. Syms and J. Cozens, *Optical guided waves and devices* (McGraw-Hill, London, 1992).
- ⁴ A. Yariv and P. Yeh, *Photonics: optical electronics in modern communications* (Oxford University Press, Oxford, 2007).
- ⁵ M. A. Reilly, B. Coleman, E. Y. B. Pun, R. V. Penty, I. H. White, M. Ramon, R. Xia, and D. D. C. Bradley, *Appl. Phys. Lett.* **87**, 231116 (2005).
- ⁶ L. D. Negro, P. Bettotti, M. Cazzanelli, D. Pacifici, and L. Pavesi, *Opt. Comm.* **229**, 337 (2004).
- ⁷ T. Kobayashi, J.-B. Savatier, G. Jordan, W. J. Blau, Y. Suzuki, and T. Kaino, *Appl. Phys. Lett.* **85**, 185 (2004).
- ⁸ M. D. McGehee, R. Gupta, S. Veenstra, E. K. Miller, M. A. Díaz-García, and A. J. Heeger, *Phys. Rev. B* **58**, 7035 (1998).
- ⁹ M. Berggren, A. Dodabalapur, R. E. Slusher, and Z. Bao, *Nature* **389**, 466 (1997).
- ¹⁰ K. Yamashita, T. Kuro, K. Oe, and H. Yanagi, *Appl. Phys. Lett.* **88**, 241110 (2006).
- ¹¹ T. Kobayashi, M. Flammich, G. Jordan, R. D'arcy, M. Rütger, W. J. Blau, Y. Suzuki, and T. Kaino, *Appl. Phys. Lett.* **89**, 131119 (2006).
- ¹² M. D. McGehee, R. Gupta, E. K. Miller, and A. J. Heeger, *Synthetic Metals* **102**, 1030 (1999).
- ¹³ A. Camposeo, E. Mele, L. Persano, D. Pisignano, and R. Cingolani, *Opt. Lett.* **31**, 1429 (2006).
- ¹⁴ M. Casalboni, F. De Matteis, V. Merlo, P. Proposito, R. Russo, and S. Schutzmann, *Appl. Phys. Lett.* **83**, 416 (2003).
- ¹⁵ Y. Yang, C. Ye, W. Ni, K. Wong, M. Wang, D. Lo, and G. Qian, *J. Sol-Gel Sci. Techn.* **44**, 53 (2007).

- ¹⁶ C. W. Tang and S. A. Vanslyke, Appl. Phys. Lett. **51**, 913 (1987).
- ¹⁷ Y. Kawabe and J. Abe, Appl. Phys. Lett. **81**, 493 (2002).
- ¹⁸ T. H. Lee, K. L. Tong, S. K. So, and L. M.-L. Leung, J. J. App. Phys. **44**, 543 (2005).
- ¹⁹ H. Suzuki, Appl. Phys. Lett. **76**, 1543 (2000).
- ²⁰ H. Suzuki, Appl. Phys. Lett. **80**, 3256 (2002).

Chapter 5: Microring Laser Cavities

5.1 - Introduction

It was shown in Chap. 4 that it is possible to achieve laser oscillation in the near-infrared region from dye-doped plastic thin films using the simplest form of optical resonators: the Fabry-Pérot cavity. In the present chapter, laser emission is reported from microrings instead. These laser devices are peculiar in that no external mirrors are required to provide optical feed-back. They are both gain medium and resonator with the feed-back provided by total internal reflection (TIR) at the cavity boundary. In short, a microring is a cavity small in size with a high quality factor and a strong coupling between spontaneous emission and the lasing modes, characteristics that should facilitate a low laser threshold. Although a simple technique to fabricate microrings has been long known,¹ it is the work published by Kuwata-Gonokami *et al.*² that sparked renewed activity in the plastic microring field. Microcavities are of interest in both fundamental (cavity quantum electrodynamic effects)³ and applied research (filters, switches and modulators).⁴ Furthermore, electroluminescence has been observed from light-emitting diodes in the form of a microring.⁵ Thus, a microring is a possible geometry for the elusive current-injected organic laser. In this chapter, the operating characteristics of a microring as a resonator (free spectral range, quality factor, mode assignment) and as a laser device (laser emission, laser threshold, transverse coherence) are investigated under photo-pumping. Special attention is given to the effect of cavity size on the quality factor and the laser threshold.

5.2 - Whispering Gallery Modes

A microring consists of a core made of a low refractive index material (typically

silica glass) surrounded by a gain medium of a higher refractive index. The surrounding air with a low refractive index constitutes the third layer. The microring supports the so-called whispering gallery modes (WGMs). These are rays that travel around the gain layer by bouncing off the outer wall through total internal reflection (TIR) and fold back upon themselves (Fig. 5.1).

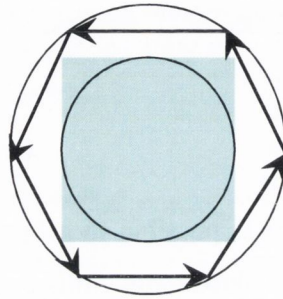


Figure 5.1 A possible path followed by a whispering gallery mode.

5.2.1 - A Bit of History

St Paul's cathedral in London includes in its architecture a Whispering Gallery, which runs around the inside of the dome. Its name arises from the curious fact that a whisper spoken against its wall can be heard by another person whose ear is against another point along the gallery wall. Surprisingly, a whisper is more effective than a shout. Other circular buildings around the world exhibit the same phenomenon (Fig. 5.2).

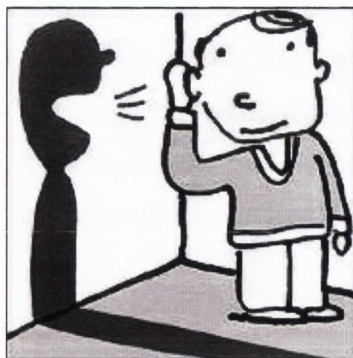


Figure 5.2 A sketch that illustrated an article on a newspaper's webpage on the science behind the whispering gallery at Grand Central terminal in New York..⁶The shape of the walls is misleading.

Lord Rayleigh was the first to explain the phenomenon and attributed it to sound creeping along curved walls. These sound waves would suffer little diffraction as they were supported by the “whispering gallery” modes, i.e. acoustical resonances inside the dome. Bates⁷ later showed that low frequencies (whispers are made of high frequencies) are also well projected. However, the success attained with a whisper is due to its low intensity, which does not give rise to audible echoes.

5.2.2 - Theory

The mechanisms underlying the whispering gallery mode theory can be found in [8]. First, the propagation of a wave through a dielectric medium is described by the wave equation. In its scalar form, it reads

$$\nabla^2 E + k^2 E = 0 \quad (5.1)$$

where E is the electric field amplitude and k is the wavevector. $k^2 = \omega^2 n^2 / c^2$, ω is the angular frequency, n is the refractive index, and c is the velocity of light in vacuum.

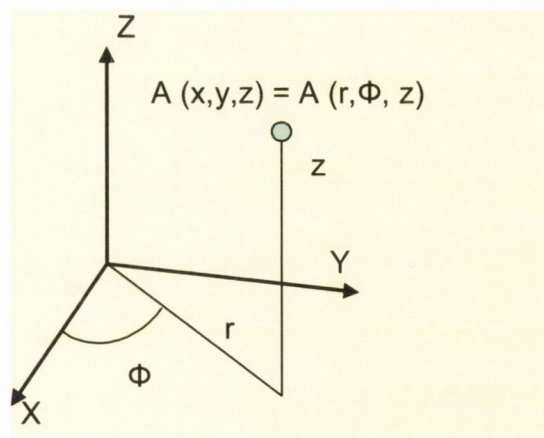


Figure 5.3 Cylindrical (r, ϕ, z) and rectangular (x, y, z) coordinate systems

The wave equation can be solved in 11 different orthogonal coordinate systems.⁸ We choose the cylindrical coordinates as the most convenient for the microring case as

these resonators have a cylindrical symmetry. The cylindrical coordinates (Fig. 5.3) are the axial coordinate z , the radial coordinate r , and the azimuthal angle ϕ . They are expressed in the Cartesian coordinates x , y , and z as

$$\begin{aligned} r &= \sqrt{x^2 + y^2} \\ \phi &= \arctan\left(\frac{x}{y}\right) \\ z &= z \end{aligned} \tag{5.2}$$

In cylindrical coordinates, the Laplacian operator is given by

$$\nabla^2 = \frac{1}{r} \frac{\partial}{\partial r} \left(r \frac{\partial}{\partial r} \right) + \frac{1}{r^2} \frac{\partial^2}{\partial \phi^2} + \frac{\partial^2}{\partial z^2} \tag{5.3}$$

The wave equation in cylindrical coordinates then reads

$$\frac{\partial^2 E}{\partial r^2} + \frac{1}{r} \frac{\partial E}{\partial r} + \frac{1}{r^2} \frac{\partial^2 E}{\partial \phi^2} + \frac{\partial^2 E}{\partial z^2} + k^2 E = 0 \tag{5.4}$$

Equation 5.4 can be separated into three constituents, each of which depends on a single coordinate. We therefore seek solutions of the form

$$E = R(r)\Theta(\phi)Z(z) \tag{5.5}$$

Substituting Eq. 5.5 into Eq. 5.4, multiplying it by $1/R\Theta Z$ and rearranging it, yields

$$\left[\frac{1}{R} \frac{\partial^2 R}{\partial r^2} + \frac{1}{rR} \frac{\partial R}{\partial r} + k^2 \right] + \left[\frac{1}{r^2} \frac{1}{\Theta} \frac{\partial^2 \Theta}{\partial \phi^2} \right] = - \left[\frac{1}{z} \frac{\partial^2 Z}{\partial z^2} \right] \tag{5.6}$$

As both the left- and right-hand side of Eq. 5.6 depend on different variables, they must be equal to a constant, which we defined as k_z^2 . We can then write

$$-\left[\frac{1}{Z} \frac{\partial^2 Z}{\partial z^2}\right] = k_z^2 \quad (5.7)$$

A possible solution of Eq. 5.7 for $k_z \neq 0$ is

$$Z(z) = A_z e^{jk_z z} + B_z e^{-jk_z z} \quad (5.8)$$

Substituting Eq. 5.7 into Eq. 5.6, and multiplying the latter by r^2 , we can separate it into its r and ϕ dependence

$$\left[\frac{r^2}{R} \frac{\partial^2 R}{\partial r^2} + \frac{r}{R} \frac{\partial R}{\partial r} + (k^2 - k_z^2) r^2\right] = -\left[\frac{1}{\Theta} \frac{\partial^2 \Theta}{\partial \phi^2}\right] = m^2 \quad (5.9)$$

where m is a constant for the same reason stated above. Multiplying Eq. 5.9 by R/r^2 and setting $k_c^2 = k^2 - k_z^2$, yields

$$\left[\frac{\partial^2 R}{\partial r^2} + \frac{1}{r} \frac{\partial R}{\partial r} + \left(k_c^2 - \frac{m^2}{r^2}\right) R\right] = 0 \quad (5.10)$$

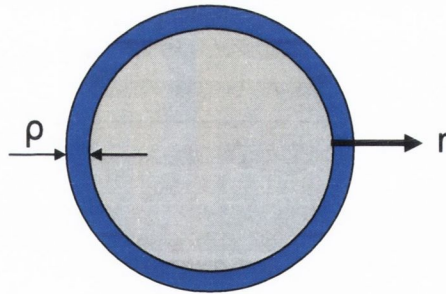


Figure 5.4 Top view of a microring (blue) with thickness ρ wrapped around an optical fibre (grey).

Equation 5.10 is a Bessel's differential equation if its third term is non-zero. We can then solve the Helmholtz equation for the particular case of transverse electric fields in lossless circular waveguides. A sketch of a microring is given in Fig. 5.4. To

simplify the problem, we use following approximation as the boundary condition at the gain layer-air interface ($r = \rho$),

$$\left. \frac{\partial E(r, \phi, z)}{\partial r} \right|_{r=\rho} = 0 \quad (5.11)$$

The solution to Eq. 5.6 is given by

$$E(\rho, \phi, z) = [A_z e^{-jk_z z} + B_z e^{jk_z z}] [A_\phi \sin m\phi + B_\phi \cos m\phi] J_m(k_c r) \quad (5.12)$$

where J_m is a Bessel function of the first kind and order m and A_z, B_z, A_ϕ , and B_ϕ are normalization constants. As the two terms in brackets in Eq. 5.12 do not depend on the variable r , the boundary condition given in Eq. 5.11 can be reduced to

$$J'_m(k_c \rho) = \frac{dJ_m(k_c \rho)}{dx} = 0 \quad (5.13)$$

Denoting the n th zero of $J'_m(k_c \rho)$ by X_{mn} , we have $X_{mn} = \rho k_c = \rho k_{cm}$. This gives the eigensolutions

$$E_m = [A_{zm} e^{-jk_z z} + B_{zm} e^{jk_z z}] [A_\phi \sin m\phi + B_\phi \cos m\phi] J_m\left(\frac{X_{mn} r}{\rho}\right) \quad (5.14)$$

X_{mn} is known as the size parameter and can be written as

$$X_{mn} = \frac{n_{eff} \omega_{mn} \rho}{c} \quad (5.15)$$

Equation 5.14 represents a standing wave that circumnavigates the microring. Index m of X_{mn} is known as the azimuthal mode number and indicates the order of the Bessel function. Index n is known as the radial mode number and gives the number

of internal field maxima in the radial direction.

It is worth pointing out that Eq. 5.13 can only be used as an approximation to describe the modes of the polymer microrings. This is due to several factors. First, there is not a strict cancellation of the electric field at the boundary where an evanescent wave exists. Second, due to surface roughness, the microrings used in experiments were not perfect cylinders as assumed above. Third, waveguiding can occur inside the gain layer as it is sandwiched between materials of lower refractive indices. Frolov *et al.*⁹ even observed a modulation of the emission spectrum when waveguided modes and WGMs were in resonance. They also showed that WGMs can propagate inside a glass core that is only partly covered with a gain layer.

5.3 - Methodology

5.3.1 - Device Fabrication (see Appendix A)

The microrings were fabricated by a simple and inexpensive technique pioneered by Weber *et al.*¹ It consists of dip-coating a glass fibre in a solvent in which a polymer and a dye have been dissolved. The technique works equally well when the solution is made up of a solvent and a conjugated polymer.^{5,9-11} Microrings formed on polymer^{5,12} and gold⁵ fibres have also been reported. They can also be fabricated on a substrate by standard photolithographic methods that involves UV radiation and reactive ion etching.¹³

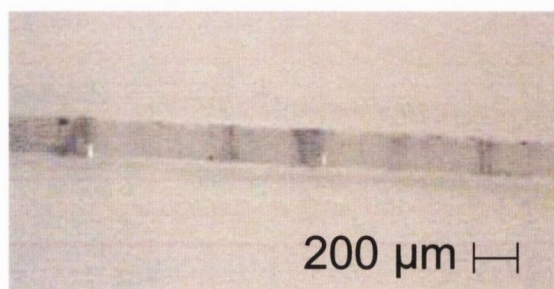


Figure 5.5 A picture of several rings on a silica fibre taken with an optical microscope.

A variety of silica optical fibres with core diameters of 80, 125, and 200 μm were bought from Newport, Inc. The 200 μm fibres had a thick plastic jacket layer that was removed with a razor blade. All three types of fibres were then placed separately into sulphuric acid at 90 °C for two hours to remove the plastic buffer layer. After the etching process, they were washed thoroughly with deionised water. To fabricate the microrings, the silica fibres were dipped by hand into the dye-polymer-solvent solution and then quickly removed. As the fibre was pulled out of the solution, several droplets would form around it due to adhesion effects and surface tension (Fig 5.5). Adhesion between two materials can be due to a number of interactions: ionic bonds, covalent bonds, hydrogen bonds, Lewis acid-base interactions, and van der Waals forces.¹⁴ Surface tension is a property of a liquid, which forces it to minimize its surface area. A liquid would behave like a membrane under tension and when free-falling for example, takes the form of a sphere as this shape offers the smallest possible surface area.

The polymer microrings formed with the dip-coating method had the barrel droplet geometric shape¹⁵, where the droplet covers the entire perimeter of the fibre. The clam-shell geometrical shape resembles a droplet drop-cast on a flat substrate as it only covers a small portion of the fibre's perimeter. Frolov *et al.*⁹ showed that laser emission is possible when the gain layer only partly covers the fibre.

The polymer concentration in the solvent is an important factor in microring fabrication. If the solution is too thick, the microrings will be too large and no laser peaks would be seen in their emission spectrum. If the solution is too thin, no microrings that are visible to the naked eye, are formed. Although the polymer PVPh was used for the results presented in Chap. 4, it was found that PVP was a more adequate polymer. Indeed, PVPh dissolves best in cyclohexanone, which has a high boiling point. A microring that dries slowly will be subject to more stress effects than one that dries fast. Precisely, a 100g/l solution of PVP in chloroform gives the best results. The microrings made from such solutions wetted longer lengths of the optical fibres and had a more uniform surface than if made from a PVP-ethanol solution for example. After evaporation of the solvent in air, each fibre would hold several microrings (Fig. 5.5) containing 0.5 wt% of the active dopant LDS 821. A picture of a 200 μm -diameter microring taken with a scanning electron microscope can be seen

in Fig. 5.6. The microring was 500 μm long and 10 μm thick. As the fabrication technique was quite simple, the ring in Fig. 5.6 does not have a perfect cylindrical shape and inhomogeneities can be observed on its surface. However as can be seen in Section 5.3.2, the pump stripe had a width of 50 μm and the middle more homogeneous part of the ring was pumped.

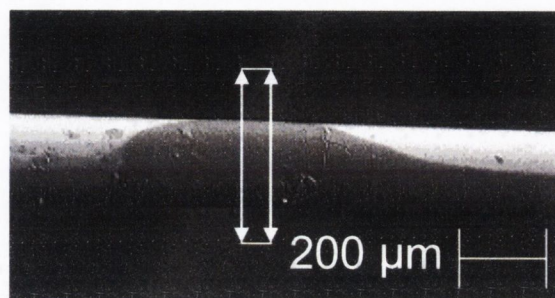


Figure 5.6 A picture of the 200 μm -diameter microring taken with a scanning electron microscope. The arrows indicate the long edges of the pump beam.

The microrings used in these studies were fabricated at room temperature. One possible way to improve the quality of the microrings would be to use fibres that have been cooled or heated, as surface tension usually increases as temperature decreases.¹⁶ Moreover, as the microrings' fabrication was quite simple, it could only be controlled to a certain extent. There should be more parameters that affect the quality of the rings and not just the choice of fibre, solvent, polymer, and polymer concentration. Logically, the drawing speed, the drawing angle, and the local polymer concentration fluctuations at the solution surface will have a great effect as well. The discussion on microring fabrication will be continued in Chap. 6.

5.3.2 - Experimental Set-up

The pump geometry used to investigate the operating characteristics of the microrings was similar to the one used for the gain spectroscopy studies on thin films (Fig. 5.7). The second harmonic (532 nm) of a Nd:YAG laser was passed through two polarisers. The second polariser was aligned in order to only transmit transverse electric polarised light while the first could be rotated to vary the pump intensity. The

beam was then formed into a thin stripe (with a width of 50 μm) by two cylindrical lenses. The microrings were positioned in the centre of the pump stripe for uniform illumination. The fibres were mounted on a vertical translational stage. Light emitted from the microrings was collected with a light guide and directed, through a 532 nm cut filter, to the entrance slit of the detection system. The spectrograph was set to its high resolution grating (1800 grooves/mm) for a resolution of 0.22 nm. With the low resolution grating (150 grooves/mm for a resolution of 3 nm), a single broad emission peak was seen at 830 nm from the microrings when pumped above the laser threshold. All the measurements were performed at room temperature under standard atmosphere.

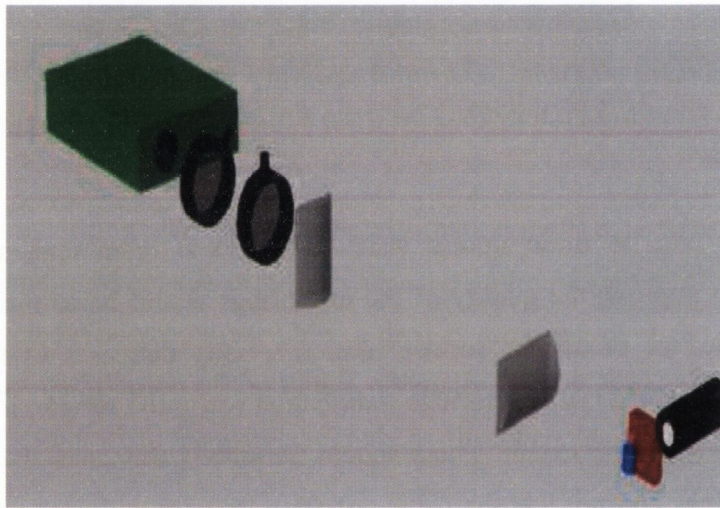


Figure 5.7: Experimental set-up for the study on microrings.

5.4 - The Microring Resonator

5.4.1 - Free Spectral Range

Microrings can be thought of as Fabry-Pérot resonators rolled around the outside of the optical fibre. As such, they support modes that satisfy the round-trip phase condition $A(\lambda) = 2\pi q$, where q is an integer. In analogy to the case of a Fabry-Pérot cavity of length L , the free spectral range (FSR) of a microring is given by

$$FSR = \frac{\lambda^2}{2n_{eff}L} = \frac{\lambda^2}{\pi n_{eff}D} \quad (5.16)$$

where $L = \pi D/2$, D is the diameter of the fibre, λ is the wavelength, and n_{eff} is the effective refractive index.

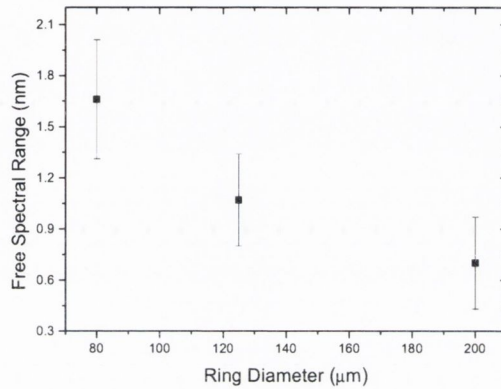


Figure 5.8 The average FSR is plotted as a function of ring diameter.

LDS821-doped PVP films have a bulk refractive index of 1.518 at 830 nm as measured using the prism-coupling method. This work was done by Pr. Kaino and co-workers at the Tohoku University (Japan). If it is assumed that the effective and bulk refractive indices are equal, the measured mode spacing for various diameters in Fig. 5.8 are in good agreement with the values predicted by Eq. 5.16 (Table V-I). This shows that the WGMs are well-confined inside the LDS821-doped layer.

Table V-I Theoretical and experimental values for the free spectral range.

Fibre diameter (μm)	Theoretical values (nm)	Experimental values (nm)
200	0.71	0.70 ± 0.27
125	1.13	1.07 ± 0.27
80	1.76	1.66 ± 0.35

5.4.2 - Quality Factor

The quality factor is defined as 2π times the number of optical cycles required for the cavity mode field to decay to $1/e$ of its initial value.² It indicates how long a photon would stay inside the cavity before being absorbed or leaking out. At a pump fluence close to the threshold value, the quality factor can be obtained from the emission spectrum by use of the relation $Q = \lambda/\Delta\lambda$ where $\Delta\lambda$ is the full-width at half maximum (FWHM). However, $\Delta\lambda$ was close to the resolution maximum of the detection system (0.22 nm) for the 200 μm -diameter rings. Therefore, instead of extracting the absolute value for the quality factor, a lower limit was placed on it by assuming that the relation $\Delta\lambda < FSR/2$ has to hold in order to distinguish adjacent peaks. The lower limit for the quality factor then reads

$$Q_{\text{lim}} = \frac{2\lambda}{FSR} \quad (5.17)$$

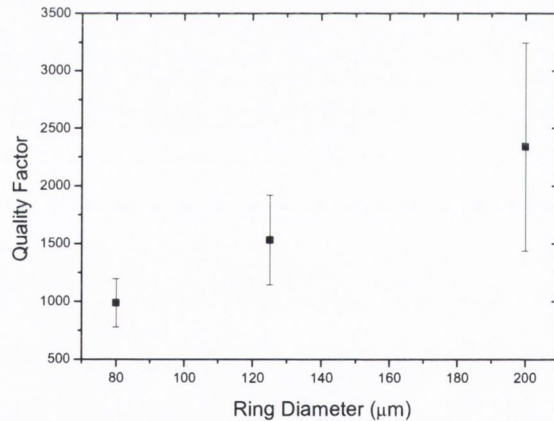


Figure 5.9 The total quality factor Q_{total} is plotted for microrings with various diameters.

The lower limit of the cavity quality factors are plotted as a function of microring diameter in Fig. 5.9. The polymer microrings show larger Q_{total} with increasing diameter. The overall quality factor Q_{total} is a summation over three major contributions:

$$\frac{1}{Q_{total}} = \frac{1}{Q_{abs}} + \frac{1}{Q_{scat}} + \frac{1}{Q_{cav}} \quad (5.18)$$

Q_{cav}^{-1} corresponds to the intrinsic diffraction photon leakage associated with the curvature of the cavity and is infinitely small for large-sized cavities. Q_{scat}^{-1} describes the losses due to light scattering by surface roughness and inhomogeneities (local density fluctuations, impurities) in the film. The absorption limited quality factor Q_{abs} is given by

$$Q_{abs} = \frac{2\pi n_{eff}}{\alpha\lambda} \quad (5.19)$$

where α is the absorption coefficient of the polymer gain medium. The absorption edge of the guest dye-molecules extends into the near-infrared region and the absorption coefficient α of the dye in solid-state form was measured to be $\alpha = 4 \text{ cm}^{-1}$ at 820 nm. Using Eq. 5.19, a value of 3×10^4 for Q_{abs} at 820 nm was obtained.

The leakage of photons due to imperfect reflection is small and Q_{cav} is several orders of magnitude higher than Q_{abs} and can therefore be neglected. As seen in Fig. 5.9-, a device with a diameter of 200 μm has an average Q_{total} of 2.3×10^3 . Using Eq. 5.18, Q_{scat} was calculated to be 2.5×10^3 , which is small in comparison with the value of 3×10^4 for Q_{abs} . This means that the upper limit for Q_{total} is set by Q_{scat} rather than by Q_{abs} . This in turn explains why the total quality factor is largest for the 200 μm -rings. The microcavities, which were all fabricated with the same technique, should exhibit the same surface roughness. The latter would play a more detrimental role for smaller sized microcavities. In the microsphere case for example,¹⁷

$$Q_{scat} = \frac{\lambda^2 D}{2\pi^2 \sigma^2 B} \quad (5.20)$$

where σ and B are the root-mean square size and the correlation length of surface inhomogeneities, respectively.

5.4.3 - Spectral Analysis: Mode Assignment.

The emission spectrum of a microring is the overlap between its cavity modes and the gain bandwidth of the chromophores. By analyzing the Fourier transform of the emission spectrum, each emission peak can be assigned a mode number. The transmitted intensity through a Fabry-Pérot resonator is given by¹⁸

$$I(\beta) = \frac{(1-R)^2 e^{-2\kappa\beta L} + 4 \sin^2(\psi)}{(1-R e^{-2k\beta L})^2 + 4R e^{-2\kappa\beta L} \sin^2(\psi + n\beta L)} \quad (5.21)$$

where β is the wavenumber, k is the absorption index, R is the power reflectance of the laser mirrors, L is the cavity length, and $\psi = \arctan\left(-2k/n^2 + k^2 - 1\right)$ is the phase change of the light due to the facet reflection. Taking the Fourier transform of Eq. 5.21 yields

$$I(d) = |1 - R \exp(2i\psi)|^2 \times \sum_{m=0}^{\infty} \sum_{l=0}^{\infty} \frac{R^{l+m} \exp[-2i\psi(l-m)]}{kL(l+m+1) + i[\pi d + nL(l-m)]} \quad (5.22)$$

where m and l are integers. The Fourier transforms $I(d)$ will only have real values when the expression $[\pi d + nL(l-m)]$ in the denominator is zero.

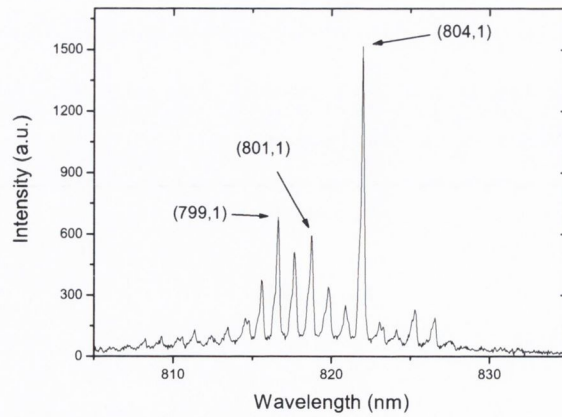


Figure 5.10 Emission from a 125 μm ring pumped at 2.15 mJ/cm^2

In the case of a microring $2L = \pi D$ and the Fourier spectrum would consist of a set of diminishing harmonic peaks with abscissae that are at multiples of $d = nD/2$, where d is the average pathlength of a mode around the microring. The emission spectrum of a 125 μm -ring at $2.15 \text{ mJ}/\text{cm}^2$ was chosen for the mode assignment (Fig 5.10). The spectrum features several evenly spaced sharp peaks distributed over a range of 15 nm at around 820 nm. These peaks were assigned their respective Bessel functions as follows. The emission spectrum was first converted from the wavelength to the wavevector space, given in μm^{-1} , as suggested in [19]. A Fourier transform (in pathlength space) was performed with the FFT option in the Origin graphing software. The result is plotted on a log scale in Fig. 5.11. The spacing between adjacent peaks then yields the pathlength, $n_{\text{eff}}D/2$. The size parameter X_{mn} , which was introduced in a previous section (Eq. 5.15) can be rewritten as

$$X_{mn} = \frac{\pi n_{\text{eff}} D}{\lambda} \quad (5.23)$$

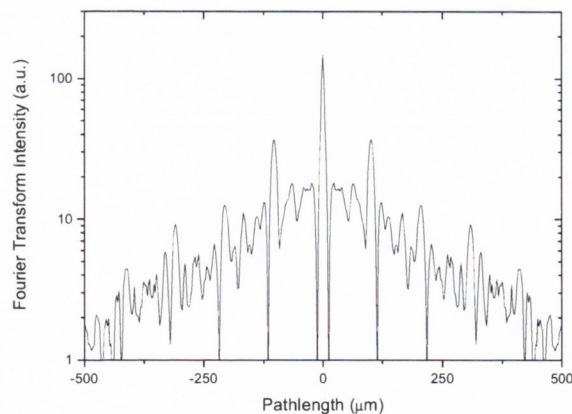


Figure 5.11 Fourier transform of the emission spectrum in Fig. 5.10.

A pathlength of 102.77 μm was obtained from Fig. 5.11. The product, $n_{\text{eff}}D/2$ acquired with this method is more accurate for this particular ring than if calculated using Eq. 5.16 because the refractive index varies with wavelength and the manufacturer gives an error of 3 μm for the fibre diameter.

As a starting point for the mode assignment, the peak with the highest intensity

(821.983 nm) was chosen. Substituting the value of $102.77 \mu\text{m}$ from the Fourier transform into Eq. 5.23, X_{mn} was found to have the value of 785. The first zero of the Bessel function 785 calculated with the Mathematica software has the value 962.31, which is much larger than the wavelength of the observed peak. A possible explanation for this discrepancy is that the effective refractive index n_{eff} used here is essentially an average as each mode should experience a different refractive index. The Bessel function 804 is closer to the observed peak wavelength with a value of 821.367 nm. The entire spectrum can then be explained with successive Bessel functions, with $X_{mn} = 798$ for the short wavelength peak and $X_{mn} = 808$ for the long wavelength peak. Three modes in Fig. 5.8 were labelled with their corresponding Bessel functions. The difference between the predicted and experimental peak wavelengths is larger than that given in [19,20]. A possible explanation is that the microrings used here have a rougher surface, which has an effect on the pathlength, than the ones studied in [19,20].

5.5 - The Microring Laser

5.5.1 - Laser Emission

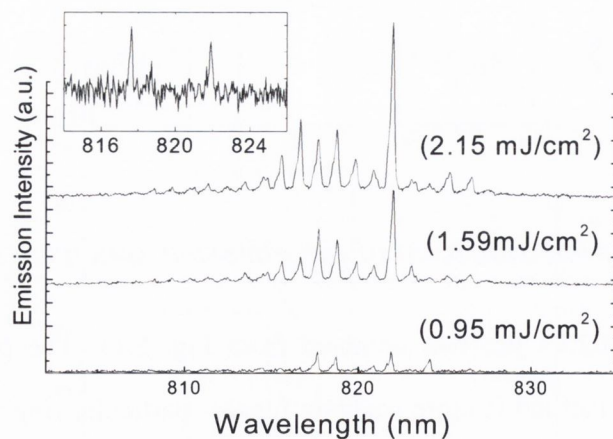


Figure 5.12 Emission spectra for a $125 \mu\text{m}$ -microring for increasing pump fluences (from bottom to top). Inset: Emission spectrum at 0.71 mJ/cm^2 , just above laser threshold.

Microrings have a circular shape and thus their laser emission is in the plane. As the pump fluence was increased, sharp peaks were observed in the emission spectrum above a certain value, the laser threshold. Below that value, the integrated emission over the range allowed by the detection system varied proportionally with the pump fluence, indicating spontaneous emission. The rings' emission spectra in the present studies did not exhibit the periodic modulation observed by Frolov *et al.*⁹ They attributed the different sets of peaks to a rise in Q_{cav} whenever waveguide modes and WGMs were in resonance.

Figure 5.12 shows the emission spectra from a microring with a diameter of 125 μm for a series of pump fluences above the laser threshold. The spectra feature several evenly spaced sharp peaks distributed over a range of 15 nm at ~ 820 nm. The inset in Fig. 5.12 shows the spectra of two cavity modes at 818 and 822 nm, which were taken at $720 \mu\text{J}\cdot\text{cm}^{-2}$, a fluence slightly above threshold. The appearance of such peaks is further proof that optical feed-back is provided as they are much sharper than the broad spectrum corresponding to spontaneous emission or ASE.

5.5.2 - Laser Threshold

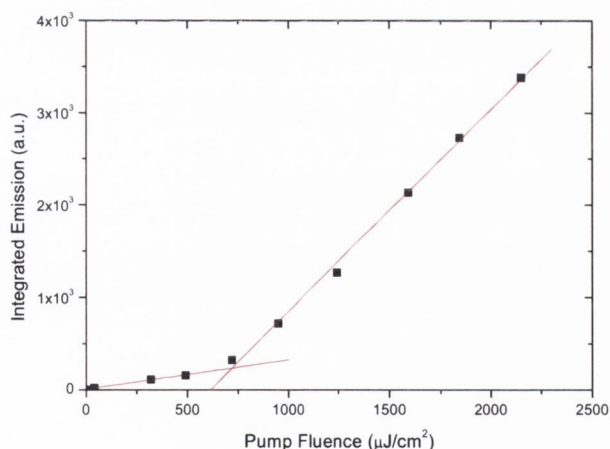


Figure 5.13 Input-output characteristic corresponding to the spectra given in Fig. 5.12. The laser threshold was found to be $718 \mu\text{J}/\text{cm}^2$.

Figure 5.13 shows the spectrally integrated emission intensity plotted as a function of pump fluence for the same microring as in Fig. 5.12. As expected for lasing, the

output shows a linear increase above threshold, which was found to be $\sim 718 \mu\text{J}\cdot\text{cm}^{-2}$ from the intersection of two straight lines fitted to the data points. Each self-assembled microring has slightly varying dimensions, which could result in a certain variation in the threshold values. An average was therefore taken over the threshold values measured for different microrings. The results are presented in Fig. 5.14, where the error bars give the standard error. The average threshold is seen to decrease with the increasing diameter of the microrings ranging from 80 to 200 μm .

The dependence of the laser threshold on the size of the microresonators can be explained with use of the expression for the threshold pump density P_{th}/V given in [21]. Simplified, it reads

$$\frac{P_{th}}{V} \propto \frac{1}{Ql} \quad (5.24)$$

where Q is the quality factor and l is the cavity length. Equation 5.24 states that the laser threshold should decrease with increasing quality factor and cavity length. This is the case here, the cavity length ($l = \pi D$) is largest for the 200- μm rings and it is known from Section 5.4.2 that the quality factor is largest for the 200 μm -diameter rings. Ben Messaoud *et al.*¹³ also found the threshold values of dye-doped microdisks (they have cylindrical symmetry just like the microrings) to be larger for cavities with smaller radius.

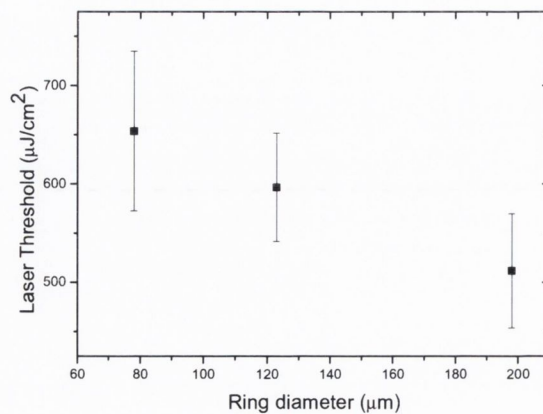


Figure 5.14 Laser threshold depicted as a function of the microring diameter.

5.5.3 - Transverse Coherence Length

Transverse coherence describes how far apart two points from the same source can be located in a direction transverse to the direction of observation and still exhibit coherent properties over a range of observation points.²² If light emitted from these two points interfere at a point a , then the distance from a to point b where the interference effects cease, is called the transverse coherence length (Fig. 5.15) and is given by

$$\zeta = \frac{r\lambda}{s} = \frac{\lambda}{\Delta\theta} \quad (5.25)$$

where r is the distance between the source and the observation plane, s is the distance between the two source points, λ is the wavelength, and $\Delta\theta$ is the angle covered by the emission.

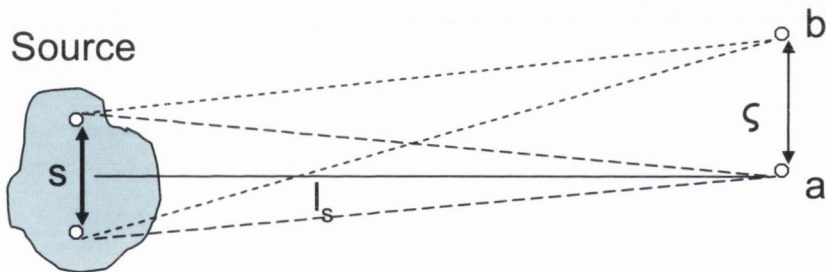


Figure 5.15 Transverse coherence length ζ .

To measure the transverse coherence length, a 1 mm pinhole was positioned in front of the light guide used to collect the emission from the microring. By varying the height of the pinhole and the light guide simultaneously (parallel to the fibre axis), the emission from the microring was monitored in steps of 0.25 mm (Fig. 5.16).

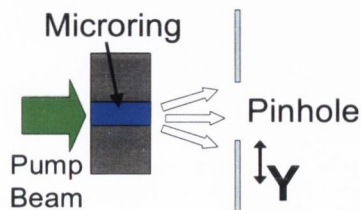


Figure 5.16 Schematic diagram for the set-up to measure the intensity distribution through a 1 mm pinhole.

Figure 5.17 shows the measured intensity distribution. A Gaussian curve was fitted to the data points, a FWHM of 3 mm, then gives an angle $\Delta\theta$ of 0.5 rad. From Eq. 5.25, the transverse coherence length is then equal to 1.6 μm at 820 nm. The small transverse coherence length ($<$ the pump width of 50 μm) indicates that the microring suffers from light scattering due to inhomogeneities and surface roughness of the polymer layer. This result confirms that losses due to light scattering make a major contribution to the reduction of the overall quality factor. Frolov *et al.*⁹ on the other hand, found that the Q -factor for their microrings was limited by reabsorption. Their microrings had their laser emission concentrated in a small cone of 0.03 rad, which is much smaller than the value of 0.5 rad found in the present studies.

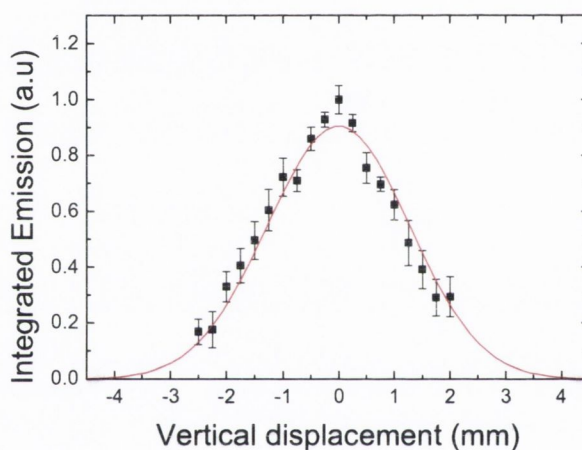


Figure 5.17 Emission of a microring with a diameter of 200 μm . The data points were well-fitted with a Gaussian curve (FWHM: 3 mm).

5.5.4 - Longitudinal Pumping

The technique used here, whereby the microring is pumped from the outside, is called transverse pumping. Dou *et al.*²³ used a different approach, they end-fired the pump beam into the optical fibre supporting the microrings and referred to it as longitudinal pumping. Such a configuration would be ideal to amplify a signal along a fibre in a telecommunications network,²⁴ an alternative to a plastic optical fibre directly doped with the laser dye.²⁵ In the longitudinal pumping configuration, the travelling pump beam, which is confined inside the fibre, refracts into the microring

once it reaches it, due to the higher refractive index of the polymer layer. Longitudinal pumping should allow for a more uniform excitation of the gain layer whereas in the transverse pump configuration, only one side of the microring is pumped. Also, there should be less surface roughness at the glass-polymer interface than at the air-polymer interface. Dou *et al.*²³ and subsequent authors²⁰ showed that the microrings' emission is not affected by the configuration used. These findings were confirmed in initial tests in this work but it was decided not to investigate longitudinal pumping any further. To compare the laser threshold in both geometries, Dou *et al.* normalised the pump fluences either to the beam diameter (transverse pumping) or the microring height (longitudinal pumping). However this approach appeared limited as light propagation inside an optical fibre differs to the free space case. No other meaningful method to compare the pump fluences in the different geometries could be worked out and longitudinal pumping was abandoned.

5.6 - Microrings in the Continuous Wave Regime

The microrings were investigated under continuous wave (CW) illumination in the transverse pumping configuration as well. The excitation source was an argon ion laser. At the pump wavelength of 488.5 nm, the LDS821 molecules in the PVP matrix had an absorption cross-section of $0.2 \times 10^{-16} \text{ cm}^2$. The emission spectrum recorded under these conditions was similar to the photoluminescence collected from drop-cast films (Chap. 3) but did not change for higher pump fluences. There was no spectral narrowing indicative of ASE. Moreover, the microrings' emission spectra did not feature sharp peaks either indicative of laser emission.

The total coupling efficiency η of continuous wave light into a ring resonator would be proportional to both the pumping efficiency and the radiative coupling efficiency.²⁶ The pumping efficiency is the ratio between the intensity effectively entering a cavity mode and the total intensity incident upon the microring. For a rough estimate, the scattering cross-sectional mode area can be approximated by $2r\lambda$ and the pump stripe area by $2rw$, where r is the microring radius and w is the

pump width. Therefore, only the portion λ/w of the pump beam interacts with the mode.

The radiative coupling efficiency into one mode is given by Q_{cav}/Q_{total} . The latter is the ratio between the radiative (Q_{cav}) and total (Q_{total}) quality factors, where each is proportional to its respective interaction area.²⁷ Just as in the case of a waveguide, microrings have evanescent fields associated with their modes but due to the finite curvature of the rings, these fields become propagative and light escapes from the cavity. These optical losses are quantified by Q_{cav} . Light can also be coupled into the microring through these evanescent fields and this coupling is therefore also proportional to Q_{cav} .

Light from all the cavity modes is coupled out over the entire surface of the microring, which has the area $2\pi r w$. A particular cavity mode would have the area $2\pi r \lambda$. The ratio of these two areas is also λ/w and the overall efficiency is then given by

$$\eta < (\lambda/w)^2 \quad (5.26)$$

Equation 5.26 actually gives the upper limit for the coupling efficiency. As stated in Section 5.4.2, Q_{cav} is large compared to Q_{scat} , and therefore most of the light is coupled into the microring through scattering rather than through the evanescent fields. The radiative coupling efficiency is therefore given by Q_{scat}/Q_{total} , which is infinitesimally small compared to Q_{cav}/Q_{total} .

Furthermore, in the case of microrings under CW illumination, reabsorption by the triplet states has to be taken into account. The microrings never reach laser threshold because of the accumulation of molecules in these states. The inter-system crossing rate (see Chap. 2) might be small, but the constant supply of excited states under CW illumination leads to a non-negligible triplet-state population. The latter has a long lifetime (up to a few seconds for certain dyes) and decay non-radiatively unless the molecules are phosphorescent dyes. Furthermore, the triplet state absorption often

shows a strong overlap with the spontaneous emission spectrum and the stimulated emission is reabsorbed. Recently, it was claimed that CW laser emission was achieved from a dye-doped polymer matrix but the triplet-state absorption issue was not discussed.²⁸ In the pulsed regime on the other hand, laser threshold can be reached. Losses due to triplet state absorption are negligible in this case, as the intercrossing lifetime is longer than the pump pulse length. Below laser threshold, the cavity modes are not visible because of the weakness of the emission intensity as stated above. Above laser threshold, gain amplification means that the signal in the cavity modes has a much stronger intensity, the mode peaks become dissociable from the background noise.

5.7 - Summary

In summary, luminescent polymer microrings were fabricated by the dip-coating technique on a variety of silica optical fibres with diameters of 80, 125, and 200 μm . Laser emission at ~ 820 nm was observed from these devices under nanosecond photo-pumping. These microcavities have a low laser threshold, a high Q -factor and narrow spectral lines (a FWHM of 0.7 nm for the 200 μm -diameter rings). The emission spectra of such microrings could be explained by matching the emission peaks to Bessel functions. Next, by characterising the laser threshold of the devices with varying cavity diameters, it was shown that the laser threshold was inversely proportional to these diameters. This was explained in terms of Q -factor and cavity length. Finally, it was revealed that the microrings suffered from scattering, which limited their Q -factor. This finding was confirmed by the small value of the spatial coherence length of their laser emission.

5.8 - References

- 1 H. P. Weber and R. Ulrich, *Appl. Phys. Lett.* **19**, 38 (1971).
- 2 M. Kuwata-Gonokami, R. H. Jordan, A. Dodabalapur, H. E. Katz, M. L. Schilling, R. E. Slusher, and S. Ozawa, *Opt. Lett.* **20**, 2093 (1995).
- 3 A. J. Campillo, J. D. Eversole, and H. B. Lin, *Phys. Rev. Lett.* **67**, 437 (1991).
- 4 V. S. Ilchenko and A. B. Matsko, *IEEE J. Sel. Top. Quantum Electron.* **12**, 15 (2006).
- 5 S. V. Frolov, A. Fujii, D. Chinn, Z. V. Vardeny, K. Yoshino, and R. V. Gregory, *Appl. Phys. Lett.* **72**, 2811 (1998).
- 6 <http://www.nytimes.com>
- 7 A. E. Bate, *Proceedings of the Physical Society* **2**, 293 (1938).
- 8 E. J. Rothwell and M. J. Cloud, *Electromagnetics* (CRC Press, Boca Raton 2001).
- 9 S. V. Frolov, M. Shkunov, Z. V. Vardeny, and K. Yoshino, *Phys. Rev. B* **56**, R4363 (1997).
- 10 Y. Kawabe, Ch Spiegelberg, A. Schulzgen, M. F. Nabor, B. Kippelen, E. A. Mash, P. M. Allemand, M. Kuwata-Gonokami, K. Takeda, and N. Peyghambarian, *Appl. Phys. Lett.* **72**, 141 (1998).
- 11 G. Ramos-Ortiz, Ch Spiegelberg, N. Peyghambarian, and B. Kippelen, *Appl. Phys. Lett.* **77**, 2783 (2000).
- 12 A. Tulek and Z. V. Vardeny, *Appl. Phys. Lett.* **91**, 121102 (2007).
- 13 T. Ben Messaoud, D. Wright, E. Toussaere, S. X. Dou, and J. Zyss, *Synth. Met.* **138**, 347 (2003).
- 14 R. D. Adams, *Adhesive bonding : science, technology and applications* (CRC Press [Woodhead Publishing], Boca Raton [Cambridge], 2005).
- 15 G. Mchale and M. I. Newton, *Colloids and Surfaces A* **206**, 79 (2002).
- 16 H. D. Young, R. A. Freedman, A. L. Ford, and T. R. Sandin, *Sears and Zemansky's university physics* (Addison-Wesley, San Francisco, 2000).

- ¹⁷ M. L. Gorodetsky, A. A. Savchenkov, and V. S. Ilchenko, *Opt. Lett.* **21**, 453 (1996).
- ¹⁸ D. Hofstetter and R. L. Thornton, *Appl. Phys. Lett.* **72**, 404 (1998).
- ¹⁹ R. C. Polson, G. Levina, and Z. V. Vardeny, *Appl. Phys. Lett.* **76**, 3858 (2000).
- ²⁰ T. Ben-Messaoud, S. X. Dou, E. Toussaere, A. Potter, D. Josse, G. Kranzelbinder, and J. Zyss, *Synth. Met.* **127**, 159 (2002).
- ²¹ A. E. Siegman, *Lasers* (Oxford University Press, Oxford, 1986).
- ²² W. T. Silfvast, *Laser fundamentals* (Cambridge University Press, Cambridge, 2004).
- ²³ S. X. Dou, E. Toussaere, T. Ben-Messaoud, A. Potter, D. Josse, G. Kranzelbinder, and J. Zyss, *Appl. Phys. Lett.* **80**, 165 (2002).
- ²⁴ Z. Vally Vardeny, *Nature* **416**, 489 (2002).
- ²⁵ G. Jordan, *Optical characterisation of blue-green emitting gain media*, Trinity College, 2006).
- ²⁶ A. B. Matsko and V. S. Ilchenko, *IEEE Sel. Top. Quantum Electron.* **12**, 3 (2006).
- ²⁷ A. B. Matsko, A. A. Savchenkov, R. J. Letargat, V. S. Ilchenko, and L. Maleki, *J. Opt. B* **5**, 272 (2003).
- ²⁸ H. Nakanotani, C. Adachi, S. Watanabe, and R. Katoh, *Appl. Phys. Lett.* **90**, 231109 (2007).

Chapter 6: Stimulated Emission Enhancement in a Microring Laser

6.1 - Introduction

High quality microcavity resonators are of interest for fundamental research in the field of quantum electrodynamics (QED). In 1946, E.M. Purcell predicted¹ that the spontaneous emission transition rate of an atom can be altered by modifying either the density of modes or the electric field strength at the location of the atom. In other words, the fluorescent lifetime is not an intrinsic property of an atom or of a molecule. In a cavity with dimensions of the order of the transition wavelength, optical confinement in one or more dimensions induces a rearrangement of the free-space density of modes and therefore an enhancement (Fig. 6.1, taken from [2]) or inhibition of the spontaneous emission.

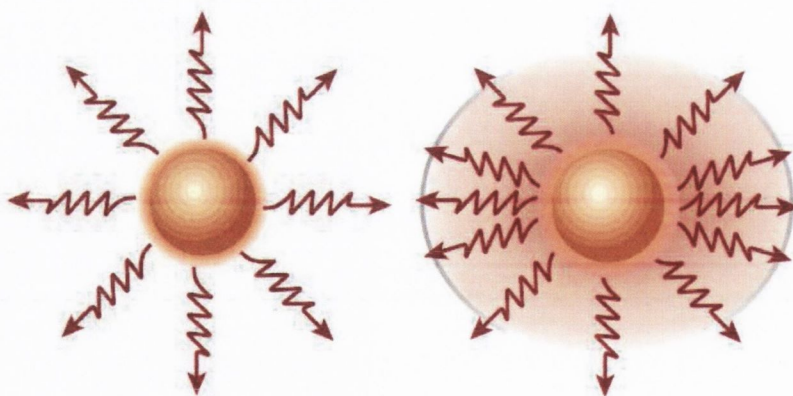


Figure 6.1 Purcell enhancement of spontaneous emission in a cavity.

As the Einstein B coefficient is proportional to the A coefficient (see Chap. 2), the spontaneous emission enhancement factor, known as the Purcell factor, also gives the

enhancement of the stimulated emission cross-section in the cavity. Purcell factors have been investigated for a variety of small molecule-doped resonators: Fabry-Pérot,^{3,4} droplets,⁵ capillaries^{6,7}, beads,⁸ and micropillars.⁹ However, although publications on dye-doped polymer microrings¹⁰⁻¹² often state that they are of interest for fundamental studies on QED effects, there have been no reports on the subject. In this chapter, a cavity enhancement of the stimulated emission cross-section is demonstrated in these resonators.

6.2 - Theory

Spontaneous emission can be seen as the interaction between matter and vacuum field fluctuations. The theory presented here is adapted from [13]. Its transition rate is given by Fermi's golden rule (similar to Eq. 2.24 of Chap. 2):

$$W = \frac{2\pi}{\hbar^2} |M_{12}|^2 g(\omega) \quad (6.1)$$

where M_{12} is the transition matrix element and $g(\omega)$ is the photon density of states. The latter will vary with the cavity size (see Fig. 6.2) and so will the spontaneous emission transition rate (Eq. 6.1).

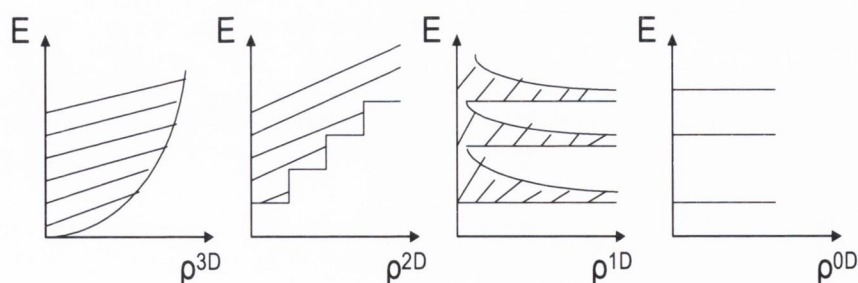


Figure 6.2 Energy as a function of density of states for bulk (3D), quantum well (2D), quantum wire (1D), quantum dot (0D).

We consider the case of a two-level atom placed inside a zero-dimensional cavity of volume V_0 . If the cavity volume is large enough so that the atom can be thought of as

being in free space, then

$$g(\omega) = \frac{\omega^2 V_0}{\pi^2 c^3} \quad (6.2)$$

For such an atom, the photon density of states has a finite value for closely spaced wavelengths and a continuum of cavity modes is available into which to decay. However, as the cavity size is reduced, the number of cavity modes decreases as well. Eventually, the cavity can be made so small that only one mode (full width at half maximum, $\text{FWHM} = \Delta\omega_c$) is close to the emission frequency of the atom ω_0 . This can be expressed as

$$\int_0^\infty g(\omega) d\omega = 1 \quad (6.3)$$

Equation 6.3 is satisfied if $g(\omega)$ takes the form of a normalised Lorentzian function. At the transition angular frequency ω_0

$$g(\omega_0) = \frac{2}{\pi\Delta\omega_c} \frac{\Delta\omega_c^2}{4(\omega_0 - \omega_c)^2 + \Delta\omega_c^2} \quad (6.4)$$

If the atom is in exact resonance with the cavity ($\omega_0 = \omega_c$), Eq. 6.4 reduces to

$$g(\omega_0) = \frac{2}{\pi\Delta\omega_c} = \frac{2Q}{\pi\omega_0} \quad (6.5)$$

The ratio of the transition rate in a cavity to that in free space is given by the Purcell factor $F_P = W^{cav}/W^{free}$. At exact resonance and with the dipoles oriented along the field direction, the Purcell factor's figure of merit is given by²

$$F_P = \frac{3Q(\lambda/n)^3}{4\pi^2 V_0} \quad (6.6)$$

For $F_P > 1$, the spontaneous emission is enhanced and Eq. 6.6 predicts that F_P will be large for large Q and small V_0 . In the case of a small cavity which does not have a cavity mode that overlaps well with the transition frequency, $F_P < 1$ and the radiative decay is inhibited.¹⁴ Spontaneous emission is not an inherent property of the atom.

Finally, we note from Eq. 6.1 that spontaneous emission is a result of the coupling between the atom dipole moment \vec{p} and the vacuum field \vec{E} , as M_{12} is the matrix element of $\langle \vec{p} \cdot \vec{E} \rangle$. The coupling can be classified as either strong or weak. The enhancement or inhibition of the spontaneous emission discussed above, are properties of the weak coupling regime. In the strong coupling regime, the transition rate is larger than the cavity loss rate and an emitted photon will be reabsorbed by the atom before it leaks out of the cavity. Spontaneous emission then becomes a reversible process and this constant exchange of energy between atom and field is called Rabi oscillation.

6.3 - Stimulated Emission Enhancement Factor Extraction Method

In this chapter, the absolute cavity QED enhancement factor of the stimulated emission cross-section is not extracted but instead a lower limit is placed on it, an approach first taken by Campillo *et al.*⁵ This technique is useful when the shape of the microcavity is not suitable to perform lifetime measurements^{4,15} or to use the pump-probe technique.⁷ It is assumed in this approach that for large pump intensities, the small-signal gain coefficient $\gamma(\lambda)$ has reached saturation and a full population inversion is achieved, i.e. all dye molecules are in the excited state. The cavity-enhanced stimulated emission cross-section σ_e^c is related to the non-cavity or bulk value σ_e by the expression

$$F_P = \frac{\sigma_e^c}{\sigma_e}, \quad (6.7)$$

When considering a time scale much shorter than the intersystem crossing lifetime and assuming that all molecules are in the excited state, one may then express $\gamma(\lambda)$ of such a dye laser by the following expression (making use of Eq. 6.7)¹⁶

$$\gamma(\lambda) = \sigma_e^c(\lambda)N_2 = F_P\sigma_e(\lambda)N_2 \quad (6.8)$$

where N_2 is the population density of the excited state S_1 . While Eq. 6.8 gives the gain per length inside the microcavity, the cavity transmission loss per length is given by the expression

$$\alpha(\lambda) = \frac{2\pi n}{\lambda Q} \quad (6.9)$$

In order to achieve laser operation from these microrings, the threshold condition $\gamma(\lambda) \geq \alpha(\lambda)$ has to be met. By assuming maximum gain and also by making use of Eq. 6.8 and 6.9, a lower limit can then be placed on the Purcell factor

$$F_P \geq \frac{1}{\sigma_e(\lambda)N_2} \frac{2\pi n}{\lambda Q} \quad (6.10)$$

6.4 - Bulk Stimulated Emission Cross-section

6.4.1 - Quantum Yield Determination

In order to determine the bulk stimulated emission cross-section of LDS821 molecules in PVP, the spectroscopic studies presented in Chap. 3 were used. First, the absorption cross-section spectrum was fitted with a Gaussian function (Fig. 6.3) to account for the absorption by the main peak only. The Gaussian fit was then expressed in terms of wavenumbers $\sigma(\tilde{\nu})$ instead of wavelengths. The extinction

coefficient spectrum $\varepsilon(\tilde{\nu})$ (Fig. 6.4) could then be calculated by use of the formula

$$\varepsilon(\tilde{\nu}) = \frac{N_a}{1000(\ln 10)} \sigma(\tilde{\nu}) \quad (6.11)$$

where N_a is Avogadro's number

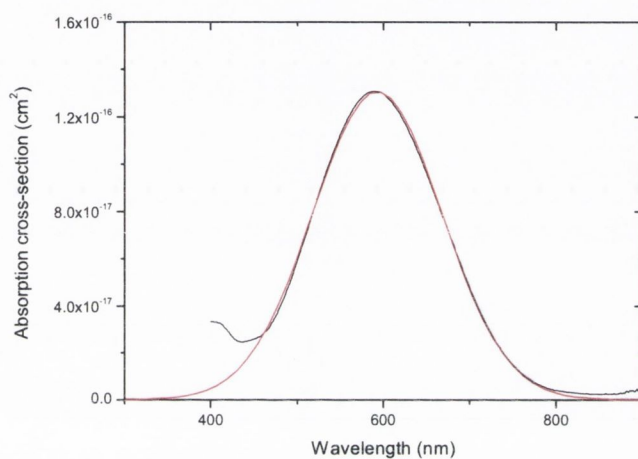


Figure 6.3 The absorption cross-section curve fitted with a Gaussian for LDS821 molecules in a PVP matrix.

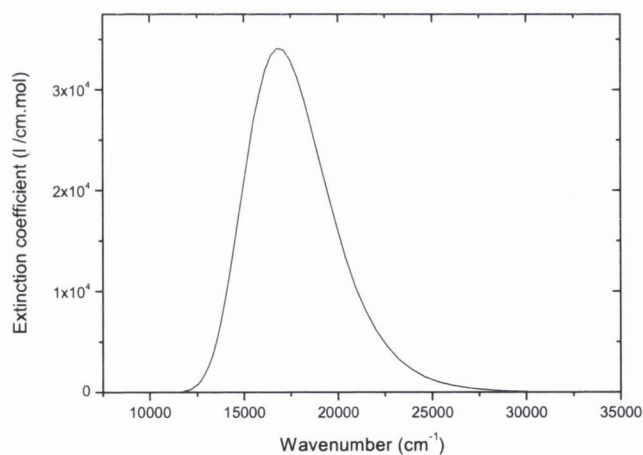


Figure 6.4 The molar extinction coefficient spectrum of LDS821 molecules in a PVP matrix.

The radiative lifetime τ_{rad} can be then calculated by use of the Strickler-Berg

formula¹⁷

$$\frac{1}{\tau_{rad}} = 2.88 \times 10^{-9} n^2 \langle \tilde{\nu} \rangle_{AV}^{-1} \int \frac{\mathcal{E}(\tilde{\nu})}{\tilde{\nu}} d\tilde{\nu} \quad (6.12)$$

where n is the refractive index, $\langle \tilde{\nu} \rangle_{AV}^{-1}$ is the reciprocal of the mean of the fluorescence spectrum $F(\bar{\nu})$, and the integral is taken over the molar extinction coefficient weighted with the wavenumber $\tilde{\nu}$.

The fluorescence spectrum of LDS821 in a PVP matrix already given in Chap. 3 was used to calculate $\langle \tilde{\nu} \rangle_{AV}^{-1}$ with the formula

$$\langle \tilde{\nu} \rangle_{AV}^{-1} = \frac{\int F(\bar{\nu}) d\bar{\nu}}{\int \frac{F(\bar{\nu})}{\bar{\nu}^3} d\bar{\nu}} \quad (6.13)$$

From the calculations, τ_{rad} was found to be 6.6 ns and from Chap. 3, it is known that the fluorescence lifetime τ_f is equal to 1.4 ns. The quantum yield $\phi = \tau_f / \tau_{rad}$ then has the value of 0.21. This means that approximately one in five excited molecules decay radiatively to the ground-state.

6.4.2 - Stimulated Emission Cross-section Determination

The photoluminescence spectrum can be normalised so that integration over emission range gives the quantum yield (Eq. 6.14). The spectrum obtained is called the lineshape function $E(\lambda)$

$$\int_0^{\infty} E(\lambda) d\lambda = \phi, \quad (6.14)$$

The stimulated emission cross-section spectrum can then be approximated by the Füchtbauer-Ladenburg equation¹⁵

$$\sigma_e(\lambda) = \frac{\lambda^4}{8\pi c n^2 \tau_f} E(\lambda), \quad (6.15)$$

where c is the speed of light. The stimulated emission spectrum is given in Fig. 6.5. It has its peak at 795 nm and has the value of $2.63 \times 10^{-16} \text{ cm}^2$ at 810 nm.

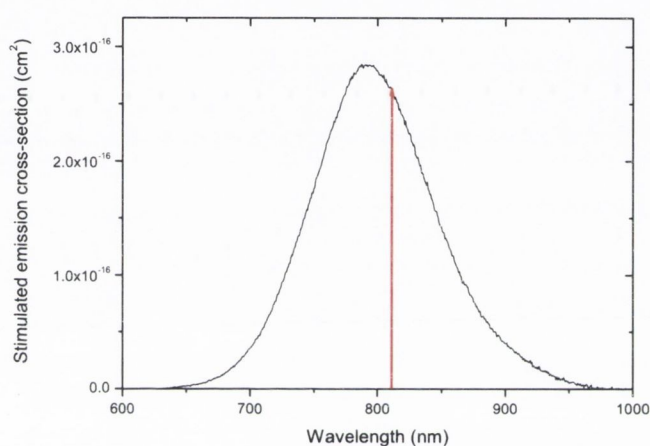


Figure 6.5 Stimulated emission cross-section spectrum. The wavelength of 810 nm is indicated with an arrow.

6.5 - Device Fabrication (see appendix A)

Polymer microcavities with a range of dye concentrations were fabricated as follows. A 0.4 wt% 100 g/l ethanol solution was prepared and subsequently diluted in steps down to a dye to polymer weight ratio of 0.001 wt%. The polymer concentration in the solvent was kept at 100 g/l for all solutions. A photograph of the vials containing the solutions with 0.009 wt% and 0.003 wt % is shown in Fig. 6.6.

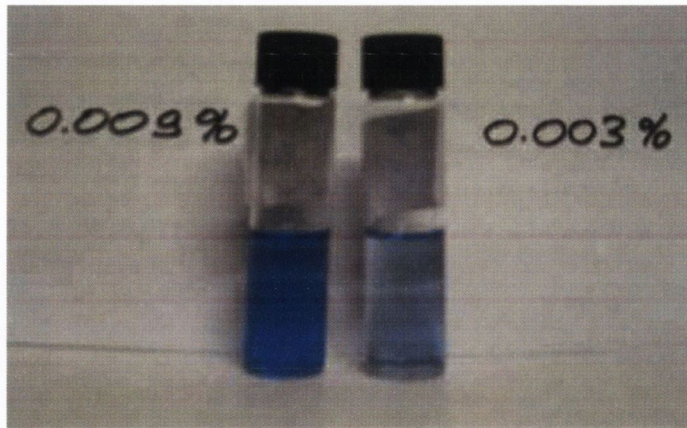
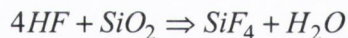


Figure 6.6 Photograph of vials containing the solutions with dye weight ratios of 0.009 wt% and 0.003 wt % (minimum experimental value).

It follows from the discussion in the previous section that small-sized cavities are needed to observe an enhancement of the stimulated emission. For the case of microrings, smaller diameters and thicknesses are required. A smaller inner diameter means using thinner optical fibres to fabricate the microrings. To that effect, the 80 μm silica fibres were etched with hydrofluoric acid to a diameter of 40 μm . The corresponding chemical reaction is



Fibres etched to a diameter of 20 μm or lower were difficult to work with due to their minuscule size and moreover, they will drift strongly in the laboratory environment. Next, the microrings fabricated in Chap. 5 were relatively thick. They had a thickness of 10 microns or more and, owing to the blue colour of the dye in the polymer matrix, were actually visible to the naked eye. Different techniques were explored in order to reduce the rings' thicknesses, such as slowly drawing out the optical fibre from a drop of solution or re-dipping the microrings again into a solvent.¹⁸ It was eventually found that for a polymer concentration of 100 g/l, minuscule rings will form on the fibre that are invisible to the naked eye and will only become apparent when pumped with the laser. Whereas the microrings characterised in Chap. 5 wetted large lengths of the optical fibre (500 μm) and assumed the shape of cylinders (Fig. 5.5 and 5.6 in Chap. 5), microrings fabricated for the work presented in this chapter were shorter and had a bulging shape. Figure 6.7 shows a photograph taken with a scanning electron microscope at a magnification

of 500. The microrings had a thickness of 2-3 μm .

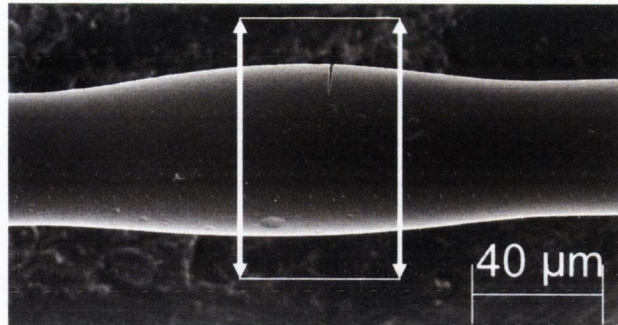


Figure 6.7 Scanning electron microscope photograph of a microring coated with a 30 nm-thick gold layer. The arrows indicate the long edges of the pump beam.

6.6 - Experimental Results

The experimental set-up used in these studies was similar to the one used in Chap. 5. (Fig 6.8, and Fig. 5.7 in Chapter 5). The second harmonic (532 nm) of a Nd:YAG laser was passed through two polarisers. No polarisers were used as high pump intensities were needed. The beam was then formed into a thin stripe (with a width of 50 μm) by two cylindrical lenses.

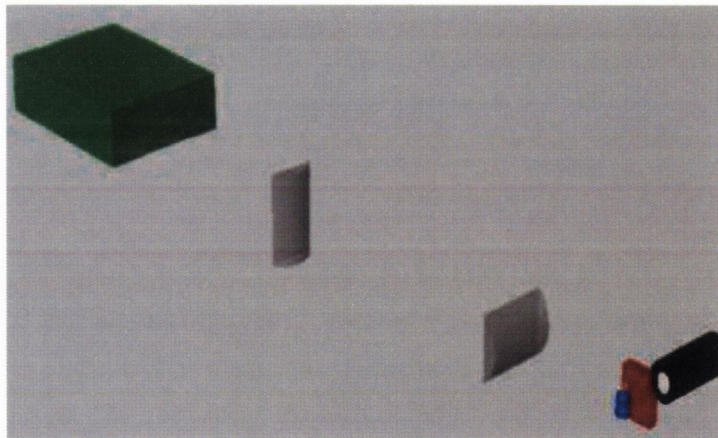


Figure 6.8: Experimental set-up for the study cavity quantum electrodynamic effects in microrings.

The microrings were positioned in the centre of the pump stripe for uniform illumination. The fibres were mounted on a vertical translational stage. Light emitted

from the microrings was collected with a light guide and directed, through a 532 nm cut filter, to the entrance slit of the detection system. The spectrograph was set to its high resolution grating (1800 grooves/mm) for a resolution of 0.22 nm. All the measurements were performed at room temperature under standard atmosphere.

In the initial tests, emission spectra from thick visible rings were recorded. Figure 6.9 shows a typical spectrum obtained from such microrings. It only shows part of the emission spectrum and that is because the detection system has a range of 50 nm when the high resolution grating is used. The data points can be well fitted with a Gaussian that has a width of 30 nm. A microring can also be thought of as a waveguide wrapped around the optical fibre and the spontaneous emission from thick microrings would be expected to be strong. The narrow width of this emission (30 nm) compared to that associated with spontaneous emission (90 nm) indicates amplified spontaneous emission.

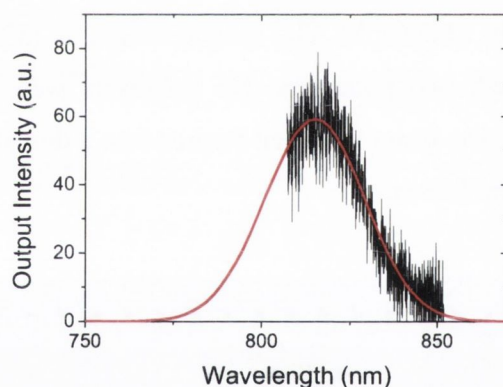


Figure 6.9 A typical amplified spontaneous emission spectrum obtained from thick microrings.

The lowest concentration for which laser peaks were observed was 0.003 wt% (30 ppm or 7.1×10^{-5} mol/L). In Fig. 6.10, emission spectra taken at two different pump fluences (107 and 178 mJ/cm²) are shown. These spectra were taken from different rings as laser operation ceased after a few tens of pump pulses. This is due to the rapid photodegradation inherent to dye molecules under standard atmosphere at large pump fluences. No input-output characteristic is therefore presented for these microrings.

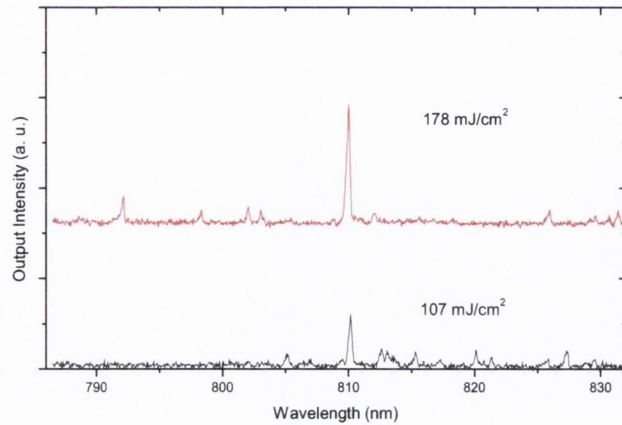


Figure 6.10 Emission spectra taken above the laser threshold for two different microrings (0.003 wt %) at two different pump fluences (107 and 178 mJ/cm²).

The quality factor Q was determined with the method used in Chap. 5. Q is given by the expression $Q = \lambda/\Delta\lambda$, where $\Delta\lambda$ is the FWHM. Lorentzian curves were fitted to both peaks in Fig. 6.8. The FWHM in both cases was 0.3 nm (above the maximum resolution of the detection system), which corresponds to a quality factor of 2700 for a wavelength of 810 nm (Fig. 6.11).

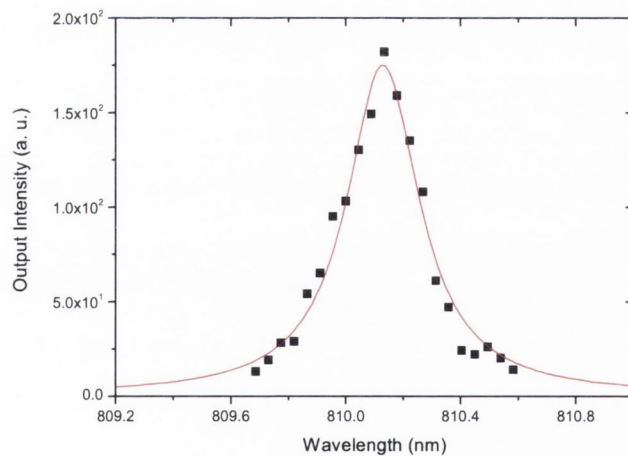


Figure 6.11 Peak at 810 nm for a pump fluence of 107 mJ/cm², fitted with a Lorentzian with a FWHM of 0.3 nm.

If there is no enhancement in the cavity ($F_P = 1$), then for $n = 1.518$,

$\sigma_e = 2.63 \times 10^{-16} \text{ cm}^2$ at 810 nm, and a quality factor Q of 2700, Eq. 6.10 predicts that the minimum population density for which lasing can be achieved is $1.66 \times 10^{17} \text{ cm}^{-3}$ (0.0116 wt%, 116 ppm, $2.74 \times 10^{-4} \text{ mol/L}$). Using $Q = 2700$ and Eq. 6.10, observing laser emission for 0.003 wt% solution corresponds to a minimum enhancement factor of 3.9 for the stimulated emission cross-section of these cavity modes. This is the first report of QED effects in polymer microrings.

6.7 - Discussion

The stimulated emission enhancement factor of 3.9 reported here is small compared to the value of 120 given by Campillo *et al.*⁴ The gain medium in reference [4] was a falling stream of 14 μm -diameter Rhodamine 6G-ethanol droplets. The difference in the enhancement factor could be attributed to three main factors. First, the microrings (diameter of 40 μm) are of a larger size than the microdroplets. Second, while optical confinement occurs in all three dimensions for a microdroplet, the confinement in the microrings used in this experiment can be considered to be one-dimensional as only their thickness is of the order of (λ/n) . The enhancement factor was found to be close to unity for both Fabry-Pérot³ and capillary cavities.⁵ Third, dye photodegradation would have been less of a concern in a laser with dye circulation. It can be concluded from the rapid disappearance of the laser peaks in the emission spectrum that photodegradation effectively reduces the number of dye molecules available for laser action in the solid-state microrings used here. It is therefore possible that the enhancement factor has been underestimated here and that for an improved photostability, e.g. if the experiment was performed in a nitrogen atmosphere, the laser threshold would have been reached at even lower dye concentrations, giving an enhancement factor closer to its true value. One result of Chapter 4 is that LDS821 is more photostable in PVPh than in PVP. Finding a solvent with a lower boiling point than Cyclohexanone to dissolve PVPh could possibly result in fabricating more photo-stable microrings with a homogeneous and smooth layer and therefore good candidates for CQED effects investigation.

6.8 - Summary

In summary, laser operation has been achieved from dye-doped polymer microrings at a dye concentration lower than predicted by theory. This is explained in terms of cavity quantum electrodynamic effects as the dye stimulated-emission cross section is enhanced inside such a microcavity. A lower limit of 3.9 was derived for this enhancement factor. The combination of enhanced stimulated emission cross-section with other CQED effects such as high spontaneous emission coupling ratio,⁴ should lead to low-threshold operation, a prerequisite for the development of practical optically pumped amplification devices as well as for the future demonstration of an electrically pumped organic gain medium.

6.8 - References

- ¹ E. M. Purcell, Phys. Rev. **69**, 681 (1946).
- ² K. J. Vahala, Nature **424**, 839 (2003).
- ³ F. Demartini, P. Mataloni, and L. Crescentini, Opt. Lett. **17**, 1370 (1992).
- ⁴ M. Osuge and K. Ujihara, J. Appl. Phys. **76**, 2588 (1994).
- ⁵ A. J. Campillo, J. D. Eversole, and H. B. Lin, Phys. Rev. Lett. **67**, 437 (1991).
- ⁶ J. C. Knight, H.S.T. Driver, and G.N. Robertson, J. Opt. Soc. Am. B **11**, 2046 (1994).
- ⁷ M. A. Noginov, G. Zhu, M. Bahoura, C. E. Small, C. Davison, J. Adegoke, V. P. Drachev, P. Nyga, and V. M. Shalaev, Phys. Rev. B **74**, 184203 (2006).
- ⁸ P. Sandeep and P. B. Bisht, Chem. Phys. Lett. **371**, 327 (2003).
- ⁹ A. M. Adawi, A. Cadby, L. G. Connolly, W. C. Hung, R. Dean, A. Tahraoui, A. M. Fox, A. G. Cullis, D. Sanvitto, M. S. Skolnick, and D. G. Lidzey, Adv. Mater. **18**, 742 (2006).
- ¹⁰ S. X. Dou, E. Toussaere, T. Ben-Messaoud, A. Potter, D. Josse, G. Kranzelbinder, and J. Zyss, Appl. Phys. Lett. **80**, 165 (2002).
- ¹¹ Y. Kawabe, Ch. Spiegelberg, A. Schulzgen, M. F. Nabor, B. Kippelen, E. A. Mash, P. M. Allemand, M. Kuwata-Gonokami, K. Takeda, and N. Peyghambarian, Appl. Phys. Lett. **72**, 141 (1998).
- ¹² M. Kuwata-Gonokami, R. H. Jordan, A. Dodabalapur, H. E. Katz, M. L. Schilling, R. E. Slusher, and S. Ozawa, Opt. Lett. **20**, 2093 (1995).
- ¹³ Mark Fox, *Quantum optics: an introduction* (Oxford University Press, Oxford, 2006).
- ¹⁴ S. Haroche and D. Kleppner, Physics Today **42**, 24 (1989).
- ¹⁵ J. M. Gerard and B. Gayral, J. Lightwave Technol. **17**, 2089 (1999).
- ¹⁶ O. G. Peterson, J. P. Webb, W. C. Mccolgin, and J. H. Eberly, J. Appl. Phys. **42**, 1917 (1971).
- ¹⁷ S. J. Strickler and Robert A. Berg, J. Chem. Phys. **37**, 814 (1962).
- ¹⁸ G. Jordan, *Optical Characterisation of Blue-Green Emitting Gain Media: Light Amplification, Laser Emission, and Two-Photon Absorption* (PhD. Trinity College Dublin, 2006).

Chapter 7: Summary and Future Work

The first aim of this work was to find an organic dye with emission in the near-infrared region that showed high optical gain when embedded in a polymer matrix. The molecule LDS821 (also known as Styryl 9) fulfilled this criteria. It belongs to the cyanine family and is a cationic dye with a perchlorate counterion. Upon absorption of a photon, it experiences a charge shift from its (dimethylamino)phenyl group towards its benzothiazolinium group. In general, an organic dye possesses larger dipole moment in its ground state. However, a numerical calculation using density functional theory showed that LDS821 instead has a larger dipole moment when in the ground state. Consequently, there should be a shift to shorter wavelengths of its absorption peak in increasingly polar solvents as the solvent-solute interaction becomes stronger, which was confirmed by experiment.

In solid state, it was shown that spectroscopic properties of the dye varied with the choice of host polymer. Poly(4-vinylphenol) was chosen as the most appropriate matrix for the gain spectroscopic studies. Thin films of this polymer doped with LDS821 were fabricated by the spin-coating technique. They appeared transparent, showed good absorption and good photo-stability, which is important in the case of organic gain media. Such thin films are in fact slab asymmetric waveguides, they were 1.7 μm thick and could support three transverse electric and three transverse magnetic modes. The gain in these waveguides was measured by the variable-stripe-length method for various pump fluences. A large gain coefficient of $37 \pm 2.1 \text{ cm}^{-1}$ and a small-signal gain of $19.7 \pm 2.3 \text{ dB}$ were demonstrated at 820 nm in 1.2 mm long waveguides under nanosecond photopumping. This is the largest gain reported to date for organic gain media operating in the near-infrared region of the spectrum. A compact photopumped amplifier made of this gain media would operate at a wavelength where optical fibres made of perfluorinated polymers have low losses.

Both could be implemented in an all-organic short distance communication network that offers low-cost production, easy installation, and maintenance.

With the ever-increasing demand for bandwidth, the next step would be to investigate organic dyes that have their photoluminescence deeper in the near-infrared region. It has been shown that amplified spontaneous emission (ASE) is possible from organic dyes in the range 1.14-1.27 $\mu\text{m}^{1,2}$, which is a spectral region close to the other two key wavelengths in silica-based long-distance telecommunications (1330 and 1550 nm). Furthermore, other classes of organic materials might be suitable for light amplification at these long wavelengths. In recent years, new small-gap conjugated polymers have been synthesised for use in plastic solar cell research.³⁻⁵ These polymers absorb and emit in the near-infrared region. This new development could lead to high gain in the near-infrared region at low pump fluences for neat films. This is because conjugated polymers with the adequate side-groups (e.g. BuEH-PPV) suffer less from fluorescence quenching than organic dyes when prepared in the form of neat films.⁶

The near-infrared light-emitting diodes investigated in this project had a very short operation lifetime. They were fabricated under standard atmosphere and were thus subject to water and oxygen impurities. The use of a glove-box in the fabrication process should yield devices with a longer life-expectancy such as those presented in [7]. The next step towards an electrically pumped plastic laser would be to demonstrate stimulated emission from such a device under photopumping. It was shown in the course of this project that ASE (amplified spontaneous emission) in the near-infrared region is possible from a dye-doped polymer thin film with semiconducting properties. However, layering aluminium on such a device cancelled the ASE. In future work, an alternative to aluminium as the cathode material needs to be found.

The second aim of this work was to investigate dye-doped polymer microrings, which are of interest for both applied (laser devices) and fundamental (cavity quantum electrodynamics effects) studies. Microrings were formed on the perimeter of silica optical fibres with various diameters by dipping the latter into an ethanol solution of LDS821 and poly(vinyl)pyrrolidone. These microcavities were good

optical resonators with high quality factor and showed laser emission at ~ 820 nm range under nanosecond pumping. It was shown that the laser threshold was inversely proportional to the microrings' size, which can be understood in terms of quality factor and cavity length. Although the microrings had a high quality factor (> 2300 in the case of $200 \mu\text{m}$ -diameter rings), the latter was nevertheless limited by absorption and scattering losses. The scattering losses had the largest detrimental effect on the performance of these laser devices compared to radiative and absorption losses. The importance of scattering losses was confirmed by the small value of $1.6 \mu\text{m}$ for the transverse coherence length of these microlasers.

Finally, for the case of microrings that are so small that they approach the wavelength (λ/n) limit, it was shown that cavity quantum electrodynamic effects are possible. Laser operation was observed from microrings that had been doped by a dye amount theoretically too small to enable lasing. This was due to an enhancement of the stimulated emission cross-section by at least a factor of 3.9. The latter is low compared to the value of 120 for a stream of Rhodamine 6G doped droplets.⁸ This can be understood in terms of cavity size as the droplets had a diameter of only $14 \mu\text{m}$. Also, a droplet would provide confinement in three dimensions compared to the one-dimensional confinement in a microring. LDS821 does not have the photostability of other dyes such as the blue-green emitting B2080⁹ for example. It is therefore important in the future to investigate microrings doped with more resilient organic dyes to find a value for the enhancement factor closer to the true value for this particular cavity. Finally, the microrings could be further reduced by hydrofluoric acid etching to increase the enhancement factor as it is size-dependent.

7. 1 - References

- ¹ M. Casalboni, F. De Matteis, V. Merlo, P. Proposito, R. Russo, and S. Schutzmann, *Appl. Phys. Lett.* **83**, 416 (2003).
- ² Y. Yang, C. Ye, W. Ni, K. Wong, M. Wang, D. Lo, and G. Qian, *J. Sol-Gel Sci. Techn.* **44**, 53 (2007).
- ³ C. J. Brabec, C. Winder, N. S. Sariciftci, J. C. Hummelen, A. Dhanabalan, P. A. Van Hal, and R. A. J. Janssen, *Adv. Funct. Mater.* **12**, 709 (2002).
- ⁴ E. Perzon, F. Zhang, M. Andersson, W. Mammo, O. Inganäs, and M. R. Andersson, *Adv. Mater.* **19**, 3308 (2007).
- ⁵ F. Zhang, E. Perzon, X. Wang, W. Mammo, M. R. Andersson, and O. Inganäs, *Adv. Funct. Mater.* **15**, 745 (2005).
- ⁶ F. Hide, M. A. Diaz-Garcia, B. J. Schwartz, M. R. Andersson, Q. Pei, and A. J. Heeger, *Science* **273**, 1833 (1996).
- ⁷ H. Suzuki, *Appl. Phys. Lett.* **76**, 1543 (2000).
- ⁸ A. J. Campillo, J. D. Eversole, and H. B. Lin, *Phys. Rev. Lett.* **67**, 437 (1991).
- ⁹ T. Kobayashi, M. Flaemmich, G. Jordan, R. D'arcy, M. Rütther, W. J. Blau, Y. Suzuki, and T. Kaino, *Appl. Phys. Lett.* **89**, 131119 (2006).

Appendix A: Detailed Device Fabrication

Chapter 3:

Section 3.4: Liquid Phase

In each case, about 1.2 mg of LDS821 was dissolved in 100 ml of the particular solvent (methanol, ethanol, acetone, DMSO, cyclohexanone, DCM, THF, or Chloroform) giving solutions of about 12 parts per million. For such low concentrations, the absorption spectra obtained using UV-visible spectrophotometer are not affected by reabsorption. The solutions were stirred to ensure good dissolution.

Section 3.5: Solid Phase

To prepare the thin films used in this section, a solution made up of a solvent, the particular dye, and the polymer were first prepared. The particular volume and weights are shown in Table A.1.

Table A.1 Solution compositions for LDS821 mixed with various solvents and polymers.

Solvent	Solvent volume (ml)	Polymer	Polymer weight (mg)	Dye weight (mg)	Weight percent (%w)
Ethanol	2	PVP	500	2	0.4
Cyclohexanone	2	PVPh	500	2	0.4
DCM	2	PC	500	2.5	0.5
Chloroform	2	PMMA	500	2	0.4

The solutions were left standing overnight to allow complete dissolution of polymer and dye in the solvent. Then to prepare a thick film, 200 ml of a solution was dropped on a Pyrex substrate. The samples were then left to dry. In the case of the PVPh-

cyclohexanone solutions, the films were dried in a vacuum oven at 60°C for 30 min. Otherwise their surface would not be smooth.

Samples with the dyes LD800 and LDS798 were prepared in a similar fashion with the details listed in Table A.2.

Table A.2 Solution compositions for LD800 and LDS798

Dye	Solvent	Solvent volume (ml)	Polymer	Polymer weight (mg)	Dye weight (mg)	Weight percent (%w)
LD800	Ethanol	2	PVP	500	2	0.4
LDS798	Ethanol	2	PVP	500	2	0.4

Chapter 4:

To make the slab waveguides, a solution was prepared using LDS821, the polymer PVPh, and the solvent cyclohexanone. The details of this particular solution composition are given in Table A.1. A volume of 100 μl would then be dropped on a pyrex substrate ($2.5 \times 2.5 \text{ cm}^2$) fixed on a spin-coated. The substrate was rotated at 3000 rpm giving the films a thickness of 1.7 μm .

The LD800 and LDS798 samples were prepared with the solution compositions given in Table A.2 and in a similar fashion to the LDS821 samples.

In order to fabricate the OLEDs, first a solution with a material concentration of 40 g/l was prepared. To do this, 10 ml of chloroform were mixed with 280 mg of the polymer PVK, 120 mg of Butyl-PBD and 1 mg of LDS821. A volume of 1 ml was then taken from this solution and mixed with 1 ml of chloroform. The new solution had a material concentration of 20 g/l.

A volume of 100 μl was then dropped on an Glass-ITO substrate ($1.2 \times 1.2 \text{ cm}^2$) and rotated at 4000 rpm with a spin-coater giving the films a thickness of $\sim 50 \text{ nm}$. After

evaporation of the solvent, the samples were covered with a mask and put into a thermal evaporator. A 80 nm-thick layer was deposited onto the uncovered parts on the film. Each sample had 6 OLEDs on it.

Chapter 5:

To make the microrings, a solution was prepared using LDS821, the polymer PVP, and the solvent chloroform. To do this, 5 ml of chloroform were mixed with 500 mg of the polymer and 2.5 mg of LDS821. A silica optical fibre rinsed in deionised water and then in chloroform. It was then lowered into the solution and then quickly removed. Several drops of the solution would cling unto the fibre giving microrings after evaporation of the solvent.

Chapter 6:

Solutions of diminishing concentrations were prepared. Solution 1 was made of 5 ml of chloroform mixed with 500 mg of PVP and 2 mg of LDS821. The details of the other solutions are given in Table A.3. Solutions 2-5 all had the same polymer concentration than solution 1.

The microrings studied in this chapter were of smaller dimensions than those presented in Chap. 5. The latter were visible to the naked eye. I found out later that if I follow the same fabrication technique as in Chap. 5 the microrings could be so small that the optical fibre appears clean (I used to discard these samples as having no microrings). However, the presence of microrings is revealed by laser emission when illuminated, they can also be seen under a scanning electron microscope.

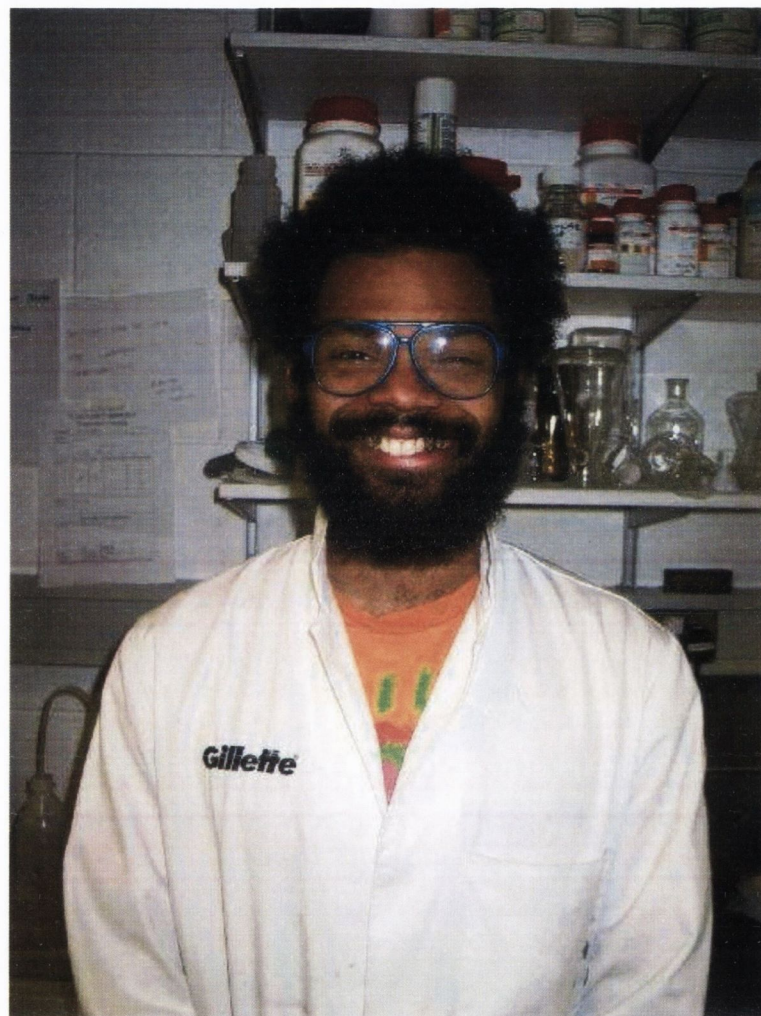
Table A.3 Solution composition for various LDS821 concentrations.

Solution number	Composition	Dye to polymer weight ratio (w%)
0	25 ml of a 100 g/l PVP chloroform solution	0
1	5 ml of 100 g/l LDS821 PVP chloroform solution	0.4
2	1 ml of Solution 1 + 4 ml of solution 0	0.08
3	1 ml of Solution 2 + 4 ml of solution 0	0.016
4	1 ml of solution 2 + 8 ml of solution 0	0.09
5	1 ml of Solution 4 + 2 ml of solution 0	0.03
6	2 ml of solution 5 + 1 ml of solution 0	0.02
7	1 ml of solution 6 + 1 ml of solution 0	0.01

Appendix B: Publications

- ¹ M. Djiango, T. Kobayashi, and W. J. Blau, "*Cavity-enhanced stimulated emission cross-section in polymer microlasers*" To be submitted (2008).
- ² M. Djiango, T. Kobayashi, W. J. Blau, B. Cai, K. Komatsu, and T. Kaino, "*Near-infrared luminescent polymer waveguide with a 20 dB small-signal gain*" Appl. Phys. Lett. **92**, 083306 (2008).
- ³ T. Kobayashi, M. Djiango, G. Jordan, M. Ruether, W. J. Blau, Y. Suzuki, and T. Kaino, "*Near-infrared light amplification and lasing in luminescent polymer microresonators*" Nonlinear Optics, Quantum Optics **37**, 1 (2007).
- ⁴ M. Djiango, T. Kobayashi, E. Bouron, W. J. Blau, Y. Suzuki, and T. Kaino, "*Operating characteristics of near-infrared self-assembled polymer microlasers*" Opt. Lett. **32**, 1375 (2007).
- ⁵ T. Kobayashi, M. Djiango, G. Jordan, M. Ruether, W. J. Blau, Y. Suzuki, and T. Kaino, "*Laser emission at 0.8 μm from photopumped luminescent polymer microresonators*" Appl. Phys. Lett. **88**, 181119 (2006).
- ⁶ M. Djiango, T. Kobayashi, G. Jordan, W. J. Blau, Y. Suzuki, and T. Kaino, "*Near-infrared optical gain and lasing in luminescent polymeric microrings*" Nonlinear Optics, Quantum Optics **34**, 251 (2005).

Appendix C: Photograph of a Physicist



2001-08: *Trinity College Dublin, Dublin, Ireland*
1999-2001: *Universität Regensburg, Regensburg, Deutschland*
1995-98: *Collège François-Xavier Vogt, Yaoundé, Cameroun*